POLITECNICO DI TORINO

MASTER's Degree in MATHEMATICAL ENGINEERING

MASTER's Degree Thesis

Numerical simulation of stable or unstable stratified cloud-mixing region.

Supervisors

Prof. Daniela TORDELLA

Candidate

Bo Yi ZHANG

2025

Numerical simulation of stable or unstable stratified cloud-mixing region.

Bo Yi Zhang

Abstract

In this work, we investigate the evolution of a two-phase system composed of clear air and unsaturated water vapor, including advected Lagrangian particles as water droplets. This, as a whole, represents an idealized cloud–clear air configuration. The flow evolves within a decaying, shearless, and stratified turbulent field, where both stably and unstably stratified conditions are considered. This configuration allows us to isolate and analyze the fundamental mechanisms governing the system and the interaction between microscale turbulence and buoyancy-driven motions.

Significant focus is placed on the role of buoyancy in generating wavelike responses in the velocity and thermodynamic fields. These responses are examined and compared to the theoretical behavior of internal gravity waves (IGWs), with attention to the amplification or damping of vertical velocity fluctuations as a function of the intensity of stratification and initial conditions.

To achieve this, high-resolution direct numerical simulations (DNS) are performed using a pseudo-spectral solver with two-phase coupling, including droplet population dynamics in the cloudy region. The initial conditions consist of two turbulent regions with different turbulent kinetic energies (TKE), smoothly connected through a transition layer, thereby mimicking a realistic cloud–clear air interface.

Following the numerical method, a spectral analysis is conducted in both spatial and temporal domains to identify the dominant wave structures and their interactions with the turbulent background. The balance between turbulence and gravity is studied to unravel the processes that control cloud–clear air mixing and the emergence of coherent wave patterns where possible. The results highlight the dynamics of stratified turbulence and its role in atmospheric circulation, implying a better understanding of cloud physics.

ACKNOWLEDGMENTS

I would like to express my deepest gratitude to Prof. D. Tordella for her invaluable guidance, constant support, and trust throughout the development of this work. I am also sincerely grateful to Shahbozbek Abdunabiev (PhD) for his assistance, especially with the numerical aspects, and for generously sharing his expertise. I would also like to thank CINECA for providing access to the Leonardo supercomputing facilities, which enabled part of the simulations presented in this thesis. Finally, I extend my heartfelt thanks to my family and friends for their patience, encouragement, and unwavering support during these years.

Table of Contents

List of Figures

List of Tables

List of Acronyms and Symbols

DNS	Direct Numerical Simulation
MPI	Message Passing Interface
FFT	Fast Fourier Transform
IGW	Internal Gravity Waves
ABL	Atmospheric Boundary Layer
RH	Relative Humidity
LWC	Liquid Water Content
TKE	Turbulent Kinetic Energy
RMS	Root Mean Square
Fr	Froude Number
Re	Reynolds Number
$\mathcal{N}$	Brunt–Väisälä Frequency
$\mathcal{N}_{\text{eff}}$	Effective Brunt–Väisälä Frequency
Re_b	Buoyancy Reynolds number
Re_λ	Taylor-scale Reynolds number

Introduction

> *"The universe cannot be read until we have learnt the language and become familiar with the characters in which it is written. It is written in mathematical language, and the letters are triangles, circles and other geometrical figures, without which means it is humanly impossible to comprehend a single word."*
> — Galileo Galilei, *Il Saggiatore* (1623)

I have been fascinated by the power of mathematics since the beginning of my academic career, because of its ability to explain, and occasionally predict, the behaviour of the natural world. Galileo thought that mathematics should be seen as a language that could reveal the underlying order of nature. Physical processes can be quantified and made predictable through mathematical formulation, which advances science from just a qualitative observation to a quantitative perspective. But this viewpoint also raises an old question: does mathematics represent a structure inherent in reality, or does it only describe the world? This debate — between an instrumental and a realist view of mathematics — has accompanied the evolution of scientific thought from its origins to the present day. Another problem, strictly connected, was raised by the English empiricists, and it concerns the origin and validity of human knowledge. The secular dichotomy between rationalism and empiricism found a synthesis through the interpretation of Immanuel Kant. As Kant wrote,in fact, mathematical judgments *"extend our knowledge"* because they do not derive from experience but rely on the pure forms of intuition — space and time — through which the mind structures all possible perception [I. Kant, *Critique of Pure Reason*, 1781]. In his view, mathematics represents the paradigm of *synthetic a priori* knowledge: it does not originate from experience, yet it applies necessarily to it. Mathematical reasoning gains meaning only when confronted with experience, while empirical data become comprehensible only when organized through mathematical concepts. Thus, mathematics emerges as the conceptual link that is required to create knowledge. Therefore a constant balance between abstraction and observation is crucial for scientific advancement and this is particularly evident in systems governed by deterministic laws which still show an unpredictable behavior. For example, the classical three-body problem reveals that infinitesimal variations in initial conditions can lead to drastically different trajectories. This describes the contemporary idea of deterministic chaos, which originated when Edward Lorenz identified this sensitivity in a simpler model of atmospheric convection.

A new notion of predictability—where precise equations do not always guarantee stable forecasts—rose from that discovery. This dichotomy is embodied in meteorology, a discipline that is both fundamentally quantitative and necessarily unpredictable. These ideas find a natural realization in the Earth's atmosphere, a complex physical system governed by a multitude of interacting processes that span a wide range of spatial and temporal scales. Just mentioning a few: Gravity, chemical reactions, thermodynamic processes and turbulence contribute to shaping from the general atmospheric circulation to local precipitations. In this context, the ability to predict atmospheric phenomena is also closely tied to a detailed understanding of cloud dynamics.

Clouds play a fundamental role in the transport of mass and energy, in the formation of precipitation, and in regulating the Earth's radiative balance. Yet the inherently multi-scale and non-linear nature of cloud processes — involving turbulence, phase changes, and microphysical interactions — makes them extremely challenging to describe accurately under realistic conditions. A key aspect of cloud dynamics is the interaction between turbulence and stratification. Stratification is a ubiquitous feature of geophysical flows, arising whenever density varies with height due to temperature or compositional gradients. The competition between buoyancy and inertial forces shapes the structure of atmospheric turbulence, influencing convection, wave propagation, and vertical transport. Understanding this coupling is essential for characterizing the mixing between air masses of different thermodynamic properties.

Over the past decades, the study of stratified turbulence has revealed the remarkable tendency of these flows to self-organize into layered structures, composed of well-mixed regions separated by sharp density interfaces. In his review article, Caulfield (2021) [1] provides a comprehensive synthesis of the current understanding of stratified turbulence, highlighting how the evolution of such layers arises from a delicate balance between overturning — the local destruction of stratification through turbulent instabilities — and scouring, the gradual erosion of interfaces by adjacent motions. These mechanisms, together with the associated energy conversion pathways between kinetic and potential energy, govern the efficiency and irreversibility of turbulent mixing. One of the key purposes of this review is to establish a unified framework for interpreting the wide variety of dynamical regimes observed in stratified flows. Caulfield emphasizes the necessity of identifying dimensionless parameters capable of quantitatively characterizing these processes across scales. Numbers such as the Richardson, Froude, and buoyancy Reynolds capture the relative influence of stratification, shear, and turbulence intensity, and thus determine whether the flow supports layer formation, wave–turbulence coexistence, or complete mixing. Theoretical and numerical studies summarized in the review demonstrate that, depending on these parameters, turbulence can coexist with waves, producing complex interactions and anisotropic energy transfers across scales. This coupling between wave dynamics and turbulent motions is now recognized as a defining feature of stratified turbulence, with profound implications for energy cascades, mixing

efficiency, and vertical transport in geophysical flows. Wave–turbulence interactions remain an open problem, as highlighted in the review by Sun et al. [2]. Their intermittent nature, together with the intricate interplay between vorticity waves, internal gravity waves (IGWs), and turbulence, makes them difficult to capture and quantify. This complexity is further compounded by the lack of appropriate numerical parameters and closure models capable of representing the transition mechanisms through which waves trigger turbulence and vice versa, as well as the inherently gradual and overlapping character of these processes. The cloud–clear air interface provides a natural laboratory for studying the interplay between turbulence and stratification. Entrainment and detrainment processes at the cloud top are governed by the local balance between turbulent mixing and buoyancy forces, leading to intermittent mixing events and, in the stably stratified case, to the spontaneous excitation of internal gravity waves (IGWs). The numerical challenge of accurately simulating a cloud-topped boundary layer across all its relevant scales has been emphasized, specially following the work of Mellado and collaborators [3, 4]. Resolving the full range of motions involved would require on the order of $O(10^6)$ grid points per spatial direction, which is currently impracticable. This limitation motivates the use of modelling approaches such as Large-Eddy Simulation (LES), though these methods offer significantly lower precision in representing the cloud-top entrainment process — a key mechanism that Mellado identifies as critical for cloud evolution and its radiative impact. To complement such approaches, Direct Numerical Simulations (DNS) have proven particularly effective in capturing the fine-scale dynamics of the cloud-top mixing layer and its sensitivity to stratification strength. Schumacher and co-workers [5] have also made significant advancement in studying mixing processes and how it affects droplets evolution.

These studies have elucidated the transient and anisotropic character of turbulence in the presence of energy gradients or stratification, providing a solid foundation for the present investigation. The present work builds upon these previous contributions to analyze in detail the effects of buoyancy during the mixing between cloud and clear air. Building upon the previous numerical experiments conducted by my supervisor and the research group [6, 7], this study employs a parallelepiped domain of $0.512^2 \times 1.024$ m^3, considerably smaller than those typically used in gravity-wave studies. This configuration highlights the small-scale processes coupled with buoyancy and their dynamical effects. High-accuracy pseudo-spectral Direct Numerical Simulations are employed to explore a set of configurations that differ in their initial stratification perturbation and turbulent intensity. The analysis encompasses both stable and unstable regimes, with the objective of identifying the spectral features of internal gravity waves in the stable case and evaluating the growth of perturbations in the unstable one. The simulations are performed using a numerical software developed within the research group, extending previous configurations or generating new ones to capture the long-term evolution of the flow.

The first chapter provides the theoretical background and establishes the physical framework of the study. It begins with an overview of the atmosphere's composition and vertical stratification, introducing the concept of static stability and the Brunt–Väisälä frequency through parcel theory. The discussion then focuses on the phenomenology of turbulence in stably stratified regimes, describing the transition from homogeneous isotropic turbulence to anisotropic, layered flows and introducing the relevant dimensionless parameters such as the Froude and buoyancy Reynolds numbers. Subsequently, the governing equations of the system are presented within the Boussinesq approximation, including the formulation of the dynamical and thermodynamic variables used in the simulations. The chapter concludes with an introduction to internal gravity wave (IGW) dynamics and their nonlinear interaction with turbulence in stratified environments.

The second chapter describes the methodology adopted in this study, including the numerical approach, the computational domain, the initial conditions, and a brief overview of the different simulations performed. It also outlines the analysis procedures used to extract the relevant dynamical information.

Finally, the last chapter presents the numerical results and discusses their physical interpretation in light of the theoretical framework introduced earlier.

Chapter 1

Physical framework

In this chapter, we outline the theoretical framework that supports the present study, with the aim of providing the physical and mathematical foundations needed to interpret the results of direct numerical simulations of cloud–clear air mixing. The atmosphere is an intrinsically complex geophysical system, where processes acting on very different spatial and temporal scales are dynamically coupled. Planetary circulation, regional weather systems, turbulence in the atmospheric boundary layer, and microphysical transformations of droplets are all interconnected through the same governing equations of fluid dynamics and thermodynamics. Understanding this cascade of interactions requires a systematic organization of theory, where successive levels of approximation are introduced to isolate the essential processes at each scale. From a large-scale perspective, the atmosphere is shaped by hydrostatic balance and Earth's rotation, which determine its vertical stratification and general circulation. At smaller scales, stratification remains a dominant factor: it controls the stability of fluid parcels and regulates the propagation of internal gravity waves, while interacting with turbulence to mediate vertical transport of heat and moisture. At the microscopic scale, the physics of cloud microdroplets introduces additional complexity: condensation and evaporation exchange energy between vapour and liquid phases, while latent heating modifies local buoyancy and can alter the stability of the surrounding fluid. It is precisely this multi-scale coupling that governs the efficiency of cloud–clear air mixing, a process of fundamental importance for cloud lifetime, radiative properties, and precipitation formation.

To build a coherent framework, we begin by recalling the macroscopic description of the atmosphere, emphasizing its chemical composition and vertical stratification. These aspects define the background state and the static stability against which turbulent and wave motions develop. We then discuss the phenomenology of turbulence in stably stratified regimes, illustrating how buoyancy modifies the classical picture of homogeneous isotropic turbulence and introduces characteristic scales such as the Froude number, the Ozmidov length, and the buoyancy Reynolds number. Subsequently, the mathematical formulation of the problem is presented within the Boussinesq

approximation, providing the set of governing equations that describe the coupled dynamics of velocity, temperature, and density fluctuations. Finally, attention is devoted to the linear theory of internal gravity waves (IGWs), which explains how perturbations propagate and exchange energy in a stratified medium. This framework also serves as a basis for understanding weakly nonlinear effects—such as wave–wave and wave–turbulence interactions—that bridge the transition from organized oscillations to turbulent mixing, forming the conceptual foundation for the numerical analyses presented in this thesis.

1.1 A brief introduction to atmospheric physics

The atmosphere is a gaseous envelope surrounding the Earth and bound to it by gravity. Its study falls within atmospheric physics, a branch of geophysics that applies the principles of classical mechanics, thermodynamics, and radiative transfer to understand the behaviour of the atmosphere as a physical system. The first quantitative explorations of atmospheric processes date back to the 17th and 18th centuries, with the works of Galileo, Torricelli, and Halley, who established the basic notions of pressure, temperature, and circulation. The modern dynamical framework emerged in the 20th century thanks to the pioneering contributions of Bjerknes, who formulated the primitive equations for atmospheric motion, Richardson, who envisioned numerical weather prediction, and Lorenz, who uncovered the role of deterministic chaos in atmospheric dynamics. Beyond its scientific interest, the atmosphere plays an essential role in sustaining life and regulating the climate. It mediates the exchange of energy between the surface and incoming solar radiation, redistributes heat and moisture through circulation, and provides the latent energy that powers convection. At the same time, it acts as a protective shield by filtering harmful ultraviolet radiation and moderating temperature variations between day and night. These processes together make Earth habitable and govern the stability of ecosystems. The atmosphere is also inherently variable. Its state changes across a wide spectrum of scales: from seconds to centuries in time, and from millimetres to planetary dimensions in space. Such variability poses both scientific challenges—such as understanding turbulence, stratification, or wave–mean flow interactions—and practical concerns, including weather prediction and the quantification of long-term climate sensitivity. In the present day, atmospheric physics extends well beyond traditional meteorology. It combines satellite observations, high-resolution numerical simulations, and laboratory experiments to analyse the coupled interactions between dynamics, radiation, chemistry, and microphysics. This integrated perspective is fundamental for addressing pressing issues such as global warming, ozone depletion, and air quality, and for understanding the central role of clouds and water vapour in Earth's energy balance. For a comprehensive overview of atmospheric structure and dynamics, the reader is referred to standard texts such as [8],[9],[10].

1.1.1 Chemical Composition

The chemical composition of the atmosphere provides the basis for understanding its thermodynamic properties, radiative balance, and capacity to sustain cloud formation. Although dominated by just two gases, nitrogen and oxygen, the remaining minor constituents exert a disproportionate influence on climate and weather due to their active radiative and chemical roles. Earth's atmosphere consists primarily of molecular nitrogen (78%) and molecular oxygen (21%). The remaining ∼1% includes constituents such as argon, water vapour, carbon dioxide, and ozone. Despite their low concentrations, these trace species play a crucial role in the planet's energy balance and chemical cycles, owing to their involvement in radiative processes and their high spatial and temporal variability. For this reason, the main components are usually referred to as *"dry air"*, while variable components such as water vapour are treated separately.

Table 1.1: Approximate composition of dry air near the Earth's surface.

Constituent	Volume fraction [%]	Notes
Nitrogen (N_2)	78.08	Inert, background gas
Oxygen (O_2)	20.95	Essential for life, combustion
Argon (Ar)	0.93	Inert
Carbon dioxide (CO_2)	0.04	Greenhouse gas, increasing
Neon, Helium, Krypton	< 0.002	Inert trace gases
Ozone (O_3)	variable (ppm)	Absorbs UV radiation
Water vapour (H_2O)	0–4	Highly variable, key to clouds

Among the variable constituents, water vapour plays a particularly crucial role. Its concentration ranges from nearly zero in polar regions to up to 4% in warm and humid tropical areas, making it the most abundant and effective greenhouse gas in the present climate system. Water vapour not only absorbs and emits infrared radiation, but also provides the latent heat that fuels convective systems and drives much of the global circulation. It represents the immediate reservoir for cloud droplets, directly linking microphysics with large-scale atmospheric energetics. Its distribution is continuously modified by evaporation from the oceans, condensation in clouds, and transport by atmospheric circulation, which explains its pronounced spatial and temporal variability.

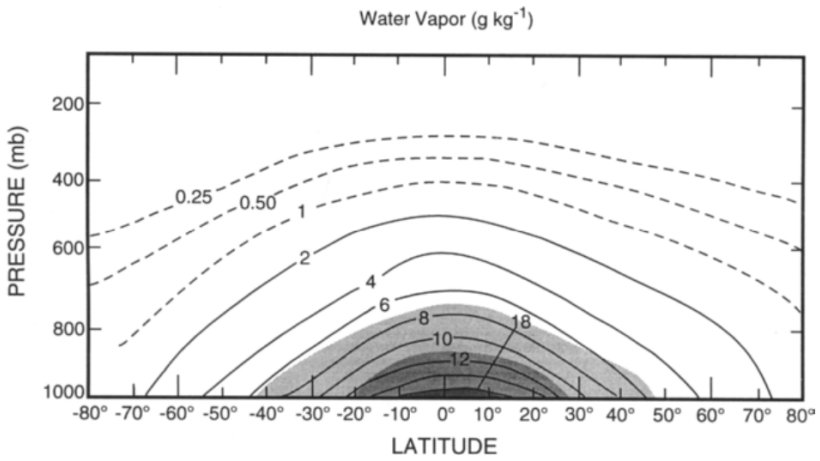

Figure 1.1: Zonal-mean mixing ratio of water vapour (contours) and absolute humidity (shaded), as functions of latitude and pressure. The shaded levels correspond to 20, 40, and 60% of the maximum value. Adapted from *Salby 2012*[8], original data from Oort and Peixoto (1983).

1.1.2 Stratification

The principal mechanism that influences the atmospheric dynamics and its properties is gravity. In fact, gravity shapes its geometry and prevents mass from escaping. Although the atmosphere has no sharp upper boundary, most of its mass is concentrated in the lowest ~ 10 km, which represents less than 1% of the planetary radius (~ 6371 km). Due to properties of the gravitational field, mass, thermodynamic variables, and chemical constituents are stratified vertically. For example, by applying Newton's second law to a shallow layer of mass we obtain the hydrostatic balance:

$$\frac{dp}{dz} = -\rho g,$$

where p denotes the pressure, z the vertical direction, parallel to the gravity, ρ is the mass density, and g is the acceleration of gravity. By applying the perfect gas law : $p = \rho RT$, eliminating ρ and integrating from the surface altitude to z, yielding :

$$\frac{p}{p_s} = e^{-\int_{z_s}^{z} \frac{g}{RT(z')}},$$

where p_s is the surface pressure. Vertical stratification imposes a kinematic constraint to the motion; in fact, in layers with vertical dimensions less than a few kilometers, circulations are predominantly quasi-horizontal.
As shown in fig.1.2 both the pressure and the density decrease approximately exponentially. Pressure decreases rapidly with altitude: from about 1000 mb ($\approx 10^5$ Pa) at the surface to nearly 10% of that value at 15 km. According to hydrostatic balance, this implies that roughly 90% of the total atmospheric mass is contained below this level. With each additional 15 km, pressure is reduced by approximately another order of

magnitude. Similarly, the mean air density, which is about 1.2 kg m^{-3} at the surface, decreases at a comparable rate with altitude. The strong vertical decrease in pressure ensures that isobaric surfaces ($p = \text{const}$) are nearly horizontal; only small deviations from horizontality occur, and these give rise to the horizontal pressure gradients that drive atmospheric motion.

If we continued to ascend, above 100 km, pressure and density continue to decrease exponentially, though at a different rate than in the lower atmosphere. This marks a transition in the processes that govern mass stratification and air composition. As density decreases, the molecular mean free path increases from about 10^{-7} m at the surface to nearly 1 m at 100 km, strongly influencing transport properties such as diffusion, viscosity, and thermal conductivity. Diffusion of momentum and heat acts to dissipate atmospheric motions by reducing gradients of velocity and temperature.
Below about 100 km, however, the mean free path is sufficiently small that molecular diffusion only weakly damps turbulent eddies. In this region, turbulent transport dominates over molecular diffusion, efficiently mixing atmospheric constituents. As a result, the mixing ratios of passive species remain nearly uniform, and the atmosphere is referred to as *"well mixed"*. This region is known as the homosphere, where turbulent mixing is the principal acting phenomenon and gives a homogeneous composition. The homosphere includes the troposphere, stratosphere, mesosphere, and the lowest part of the thermosphere, where the chemical composition of the atmosphere does not depend on molecular weight, because the gases are mixed by turbulence. While the transition from turbulent transport to diffusive transport occurs at the homopause or also known as turbopause ($\sim$ 100 km). The *troposphere* (surface to $\sim$ 10–15 km) contains most of the atmospheric mass and is characterized by a decrease of temperature with height, strong vertical mixing, and the presence of weather systems and clouds. Above it lies the *stratosphere* ($\sim$ 15–50 km), where temperature increases with altitude due to absorption of solar radiation by ozone; this region is dynamically more stable. The *mesosphere* ($\sim$ 50–85 km) is marked again by a temperature decrease with height and represents the coldest part of the atmosphere, where meteors typically burn up. Finally, the lowest part of the *thermosphere* (above approximately 85 km) still belongs to the homosphere and is characterized by a strong increase in temperature with altitude, due to the absorption of high-energy solar radiation. Above the homopause (at approximately 100 km) and up to about 500 km lies the *heterosphere*, where air flow is nearly laminar. In this region, molecular diffusion dominates over turbulent mixing and separates the constituents according to molecular weight: heavier gases such as O_2 decrease more rapidly with altitude than lighter ones like N_2, while atomic oxygen becomes dominant not far above the homopause due to photodissociation by energetic UV radiation. Photodissociation of H_2O also contributes to the production of atomic hydrogen, which diffuses upward.
Beyond $\sim$ 500 km, collisions between molecules become rare, marking the onset of the

exosphere. Here, particles follow ballistic trajectories controlled by their velocity at the critical level and Earth's gravity. Most return along parabolic paths, but those with sufficient velocity escape the planet's gravitational field and are lost to space.
In our study, the focus will primarily be on the troposphere and the stratosphere. The main property responsible for the different characteristics of these two layers is their vertical stability. While forces generally maintain hydrostatic equilibrium, vertical motions can still arise, mainly due to orographic effects and buoyancy.

To gain an intuitive understanding of how buoyancy affects motion, it is useful to introduce a heuristic approach, such as the *parcel theory*. In this framework, we consider an air parcel treated in a Lagrangian sense and subjected to a small vertical displacement z'. Its thermodynamic properties are distinguished from those of the surrounding environment, under the assumption that the displacement occurs on a timescale short compared to that of heat exchange. At the same time, the parcel adjusts through expansion or compression in order to remain in mechanical equilibrium with the external pressure ($p_p = p_e = p$). By applying Newton's second law to this displaced parcel, we obtain:

$$\rho_p \frac{d^2 z'}{dt^2} = -\rho_p g - \frac{\partial p}{\partial z'} \tag{1.1}$$

while the environmental momentum balance is simply:

$$0 = \rho g - \frac{\partial p}{\partial z}. \tag{1.2}$$

Subtracting (1.1) from (1.2) yields for the parcel:

$$\rho_p \frac{d^2 z'}{dt^2} = (\rho - \rho_p) g, \tag{1.3}$$

or equivalently

$$\frac{d^2 z'}{dt^2} = f_b, \tag{1.4}$$

where $f_b = g(\rho - \rho_p)/\rho_p$ is the specific buoyancy force acting on the parcel. For an ideal gas, because potential temperature is conserved during the parcel's motion, we can recast it in terms of θ rather than ρ:

$$\frac{d^2 z'}{dt^2} = -\frac{g}{\theta} \frac{d\theta}{dz} z'. \tag{1.5}$$

We then define the *buoyancy frequency* or *Brunt–Väisälä frequency*

$$\mathcal{N}^2 = \frac{g}{\theta} \frac{d\theta}{dz}, \tag{1.6}$$

so that (1.5) becomes the equation of a harmonic oscillator:

$$\frac{d^2 z'}{dt^2} + \mathcal{N}^2 \, z' = 0. \tag{1.7}$$

The quantity $\mathcal{N}$ has units of s^{-1} and represents an *angular frequency* (rad/s).
The corresponding oscillation *period* and the *frequency in Hz* are

$$T = \frac{2\pi}{\mathcal{N}}, \qquad f = \frac{\mathcal{N}}{2\pi}.$$

Typical values are $\mathcal{N} \sim 10^{-2}\,\mathrm{s}^{-1}$ in the free troposphere (i.e. $T \sim 10$ min) and up to $2 \times 10^{-2}\,\mathrm{s}^{-1}$ in the lower stratosphere. The sign of $\mathcal{N}^2$ controls the vertical stability and the form of the solutions of (1.7):

- **Stable stratification** ($\mathcal{N}^2 > 0$). Small displacements are opposed by a restoring buoyancy force, and the parcel performs bounded oscillations (internal gravity waves). A convenient real form of the general solution is

  $$z'(t) = A\cos(\mathcal{N}t) + B\sin(\mathcal{N}t),$$

  which is equivalent to the complex representation $z'(t) = \tilde{A}\, e^{i\mathcal{N}t} + \tilde{B}\, e^{-i\mathcal{N}t}$. In this dry and adiabatic framework, the amplitude remains constant.

- **Neutral stratification** ($\mathcal{N}^2 = 0$). In the absence of a restoring force, the governing equation reduces to $d^2z'/dt^2 = 0$ with solution

  $$z'(t) = a\,t + b.$$

  If the initial vertical velocity vanishes ($a = 0$), the parcel remains at its displaced position. This situation is typical of well-mixed layers where $d\theta/dz \simeq 0$.

- **Unstable stratification** ($\mathcal{N}^2 < 0$). Small perturbations grow exponentially, leading to convection. Defining $\sigma = \sqrt{|\mathcal{N}^2|}$, the solution reads

  $$z'(t) = A\, e^{\sigma t} + B\, e^{-\sigma t},$$

  where σ represents the growth rate of the instability.

This framework clarifies why the troposphere, often characterized by a decrease of temperature with height, can be weakly stable or even unstable, thereby favouring convection and cloud formation. In contrast, the stratosphere—where temperature increases with altitude due to ozone absorption—is strongly stable and therefore supports the propagation of internal gravity waves rather than convective overturning.

Another important dynamical factor that deserves at least a brief mention is the Earth's rotation, which gives rise to two apparent forces: the centrifugal force and the

Coriolis force. These forces play a fundamental role in atmospheric dynamics, leading to meridional stratification and influencing phenomena ranging from large-scale wave patterns to regional weather systems. A key non-dimensional parameter to quantify the importance of rotation is the Rossby number, $R_O = \frac{U}{fL}$, which compares inertial to Coriolis forces. In the present study, the effects of Earth's rotation are neglected since the Rossby number is very large ($R_O \sim 10^3$), indicating that rotational effects are only relevant at much larger spatial and temporal scales than those considered here.

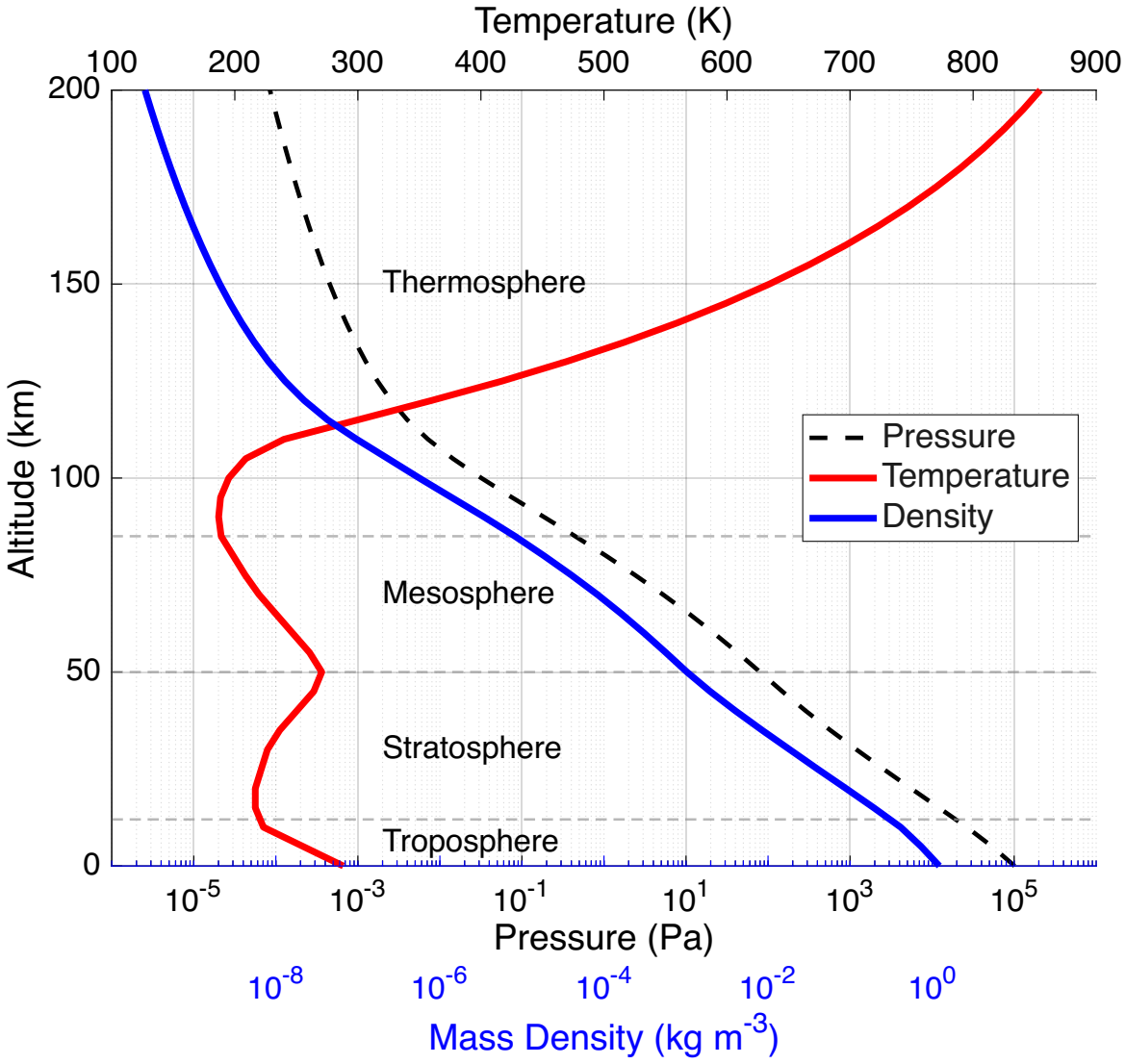

Figure 1.2: Vertical profile of pressure (dashed) , density (blue), and temperature (red) in the Atmosphere up to 200 km. Picture adapted from data of *US standard atmosphere 1976* [11].

1.2 Turbulence in Stratified Regimes

Turbulent flows are characterized by a wide range of interacting spatial and temporal scales through which energy is injected, transferred, and ultimately dissipated. In the idealized framework of homogeneous and isotropic turbulence (HIT), the absence of preferred directions allows the statistical description of the flow to depend solely on the magnitude of the wavenumber k. Energy is supplied to the system by the largest motions — the *energy-containing eddies* — whose characteristic size defines the *integral length scale* L_i, representing the typical distance over which velocity fluctuations remain correlated,

$$L_i \sim \int_0^\infty R_{uu}(r)\, dr,$$

where $R_{uu}(r)$ is the longitudinal velocity autocorrelation function. The corresponding timescale of the largest eddies, known as the *large-eddy turnover time*, is

$$\tau_L = \frac{L_i}{u'},$$

with u' denoting the root-mean-square (r.m.s.) velocity fluctuation.

According to Kolmogorov's similarity theory (K41), in a statistically stationary regime the mean rate of turbulent kinetic energy (TKE) dissipation per unit mass, ε, is the only governing parameter in the inertial range. Energy extracted from the mean flow at the largest scales cascades toward progressively smaller scales via nonlinear interactions, until viscous effects become dominant. Dimensional arguments yield the characteristic velocity scaling

$$u_\ell \sim (\varepsilon \ell)^{1/3},$$

and the associated one-dimensional energy spectrum

$$E(k) = C_K\, \varepsilon^{2/3} k^{-5/3},$$

where $C_K \simeq 1.5$ is the Kolmogorov constant. The cascade continues down to the smallest dynamically active scale, the *Kolmogorov length*,

$$\eta = \left(\frac{\nu^3}{\varepsilon}\right)^{1/4},$$

where viscosity converts kinetic energy into heat. This framework, first formalized by Kolmogorov and later extended by Batchelor [12], describes the classical energy cascade: energy is injected at the integral scale L_i, transferred conservatively across the inertial subrange, and dissipated at the Kolmogorov scale η. Homogeneous and isotropic turbulence (HIT) thus provides the universal reference state for turbulent flows, serving as the theoretical cornerstone from which more complex situations can

be interpreted.

In practical situations, however, real turbulent flows seldom satisfy the assumptions of homogeneity and isotropy. Large-scale gradients, boundary effects, rotation, and density stratification introduce preferred directions and additional physical timescales that break the statistical symmetry underlying HIT. Among these, stable density stratification plays a central role in geophysical and environmental contexts, such as the atmosphere and the ocean, where vertical motions are inhibited by buoyancy forces and turbulence coexists with internal gravity waves.

The influence of stratification can be understood through the *parcel theory* discussed in Sec. 1.1.2, where the restoring acceleration acting on a vertically displaced fluid parcel defines the Brunt–Väisälä frequency $\mathcal{N}$ and the corresponding buoyancy period $T_{\mathcal{N}} = 2\pi/\mathcal{N}$ as formulated in (1.6). These quantities set the natural timescale for oscillations about a stably stratified equilibrium and provide a measure of the strength of the background stability. When turbulent eddies attempt to displace fluid parcels vertically, this buoyant restoring force acts against inertia, thereby modifying the energy cascade and introducing a strong anisotropy in the flow.

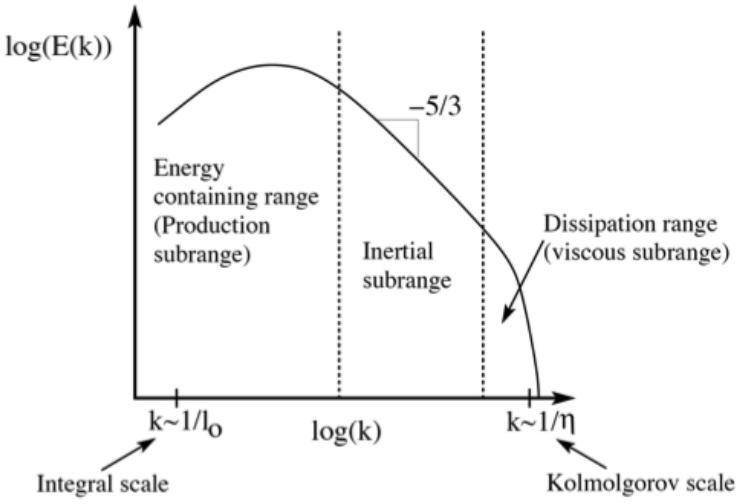

Figure 1.3: Schematic representation of the turbulent kinetic energy spectrum. The largest eddies (integral scale L) correspond to the energy-containing range, where turbulence is generated by shear and buoyancy. In the inertial subrange, energy is transferred toward smaller scales following the Kolmogorov $-5/3$ power law, until viscous effects dominate at the Kolmogorov scale η. Adapted from lecture materials on turbulent flows, University of Utah.

Dimensionless Parameters and Dynamical Regimes The relative importance of inertial and buoyant effects is measured by the *Froude number*,

$$Fr = \frac{u'}{\mathcal{N} L_i} = \frac{\tau_{\mathcal{N}}}{\tau_L}, \tag{1.8}$$

where $\tau_{\mathcal{N}} \coloneqq 1/\mathcal{N}$ is the characteristic buoyancy timescale. The Froude number compares the timescales of turbulent eddies and buoyancy oscillations. Three asymptotic regimes are commonly identified:

- $Fr \gg 1$: buoyancy is negligible and the flow behaves as HIT;
- $Fr \ll 1$: buoyancy dominates, suppressing vertical motions and leading to strongly anisotropic, layered flows;
- $Fr \sim 1$: inertial and buoyant effects are comparable, giving rise to *stratified turbulence* where eddies and internal gravity waves coexist.

As stratification strengthens, the restoring action of buoyancy limits the vertical extent of turbulent eddies. The largest vertical scale unaffected by buoyancy is known as the *Ozmidov length*,

$$L_O = \left(\frac{\varepsilon}{\mathcal{N}^3}\right)^{1/2}.$$

This scale marks the transition between isotropic turbulence ($\ell < L_O$) and wave-dominated motions ($\ell > L_O$). Below L_O, turbulence follows Kolmogorov-like scaling, while above it, vertical energy transfer is inhibited and motions become predominantly horizontal. The corresponding timescale $\tau_O = (\varepsilon/\mathcal{N}^2)^{1/2}$ represents the turnover period of eddies at the buoyancy limit. The ratio L_O/L_i thus quantifies how deeply stratification penetrates the turbulent cascade: for $L_O/L_i \ll 1$, anisotropy extends down to small scales.

A complementary parameter that characterizes the influence of viscosity and stratification on small-scale motions is the *buoyancy Reynolds number*,

$$Re_b = \frac{\varepsilon}{\nu \mathcal{N}^2}.$$

This dimensionless quantity compares the rate of turbulent kinetic energy (TKE) dissipation, ε, to the combined effects of viscous diffusion and stratification, represented by $\nu\mathcal{N}^2$. Physically, Re_b measures the extent to which turbulence can overcome the stabilizing and dissipative constraints imposed by viscosity and buoyancy. It can also be expressed as a function of the Ozmidov and Kolmogorov scales,

$$Re_b \sim \left(\frac{L_O}{\eta}\right)^{4/3},$$

thus quantifying the number of dynamically active eddies that can exist between the smallest isotropic scale η and the largest scale unaffected by stratification L_O.

When Re_b is large, stratification is weak relative to turbulent mixing, and the small scales remain nearly isotropic, allowing an extended inertial subrange to develop. Values of $Re_b \gtrsim 10^2$ correspond to fully developed stratified turbulence, while for $Re_b \lesssim 10$ the flow becomes dominated by internal gravity waves or tends toward laminarization. Intermediate values $10 \lesssim Re_b \lesssim 100$ mark the transition between wave-dominated and turbulence-dominated regimes, where intermittent layers of shear and mixing coexist with quasi-linear wave motions. In this range, small-scale isotropy is progressively lost and the turbulent cascade becomes increasingly anisotropic as vertical motions are suppressed by buoyancy. Together, (Fr, Re_b) delineate the dynamical regimes of stratified turbulence observed in laboratory and field studies [13][14]. This anisotropy manifests as flattened vortical structures, often termed *pancake eddies*, with aspect ratio

$$\frac{\ell_z}{\ell_h} \sim Fr,$$

where ℓ_z and ℓ_h denote the vertical and horizontal scales, respectively [15]. Energy accumulates at large horizontal scales while vertical gradients sharpen, producing thin layers of intense shear and density contrast. The resulting flow is highly intermittent: regions of active turbulence coexist with quiescent layers dominated by internal wave motion.

Wave–Turbulence Coupling and Relevance to Cloud Interfaces For $Fr \sim 1$ and $Re_b \gtrsim 10^2$, turbulence and internal waves coexist in a dynamically coupled state known as the *wave–turbulence regime*. Here, large-scale eddies excite internal gravity waves that can either radiate energy away or feed back onto the turbulence through local instabilities and breaking events. This mutual interaction leads to intermittent bursts of vigorous turbulent activity, separated by periods of weakly wave-dominated motion, often described as the alternation between *active* and *fossil* turbulence [16, 13].

In the *active turbulence* stage, turbulent overturning dominates over buoyant restoring forces ($Fr \gtrsim 1$), and the mixing layer is dynamically unstable with strong shear and vertical transport. Energy is transferred downscale through the turbulent cascade until buoyancy effects become significant at the Ozmidov scale L_O. As the turbulence decays, stratification progressively suppresses vertical motions, and the flow enters the *active–fossil* or *partially fossilised* stage, in which remnants of turbulence coexist with internal waves generated by the decaying motions. During this phase, the kinetic energy is largely stored in quasi-horizontal motions and internal-wave oscillations, while small-scale dissipation continues at a reduced rate. Eventually, when the turbulent overturns have fully subsided and only wave motions persist, the flow is said to be in the *fully fossilised* state. In this regime, the energy spectrum is dominated by linear

internal waves, the flow becomes nearly reversible, and mixing efficiency drops to very low values.

This sequence — from active turbulence to partially and then fully fossilised motion — represents a typical decay pathway of stratified turbulence, where the energy initially contained in overturning eddies is gradually converted into internal-wave energy and finally dissipated by molecular diffusion. The coexistence and transition between these regimes are central to the dynamics of stably stratified layers, particularly in geophysical contexts where intermittent turbulence patches and internal waves regulate momentum and scalar transport across density interfaces.

In the context of the present study, the turbulent flow develops within a weakly to moderately stratified layer at the cloud–clear air interface, where $\mathcal{N}(z,t)$ varies with height and time due to the competing effects of turbulence and buoyancy: stratification excites gravity waves, while turbulent mixing tends to erode the background gradient over time. Such conditions are characteristic of transitional atmospheric regimes in which turbulence, buoyancy, and wave dynamics coexist. In this regime, internal gravity waves are continuously generated by turbulent fluctuations, and their subsequent modulation or breaking sustains mixing, redistributing buoyancy, vapour, and droplets across the stratified interface.

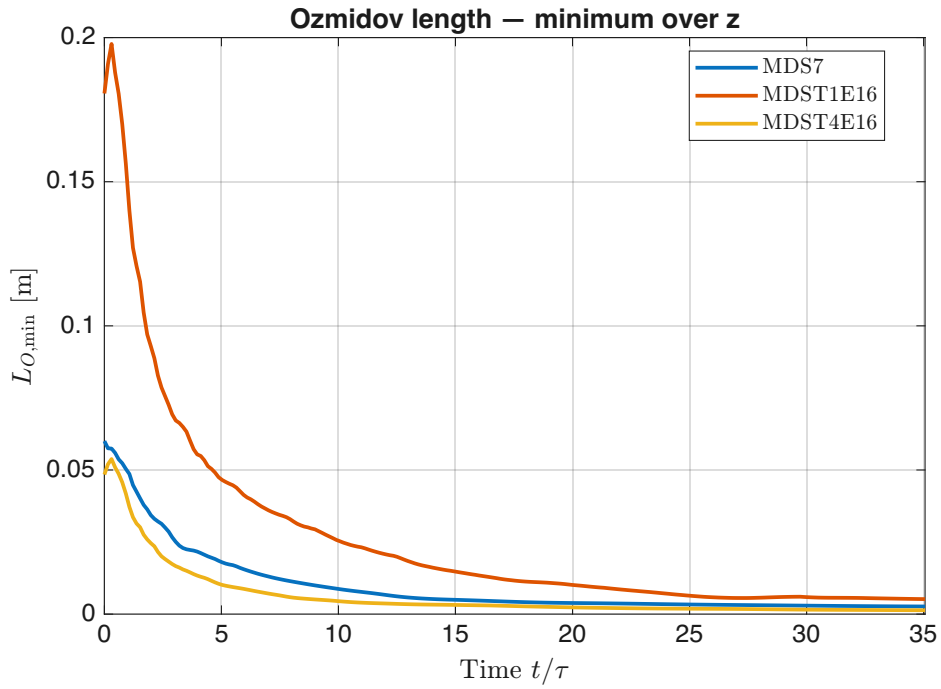

Figure 1.4: Estimated values of the Ozmidov length scale, evolution in time for some stable stratified case of the present study; $L_O(t) = (\bar{\varepsilon}/(\max \mathcal{N})^3)^{1/2}$ is evalued from the whole domain averaged dissipation rate $\bar{\varepsilon}(t)$ and the maximum value of $\mathcal{N}$ over z. We can observe that at the beginning the Ozmidov length scale assumes values of significant fraction of the horizontal domain length($L_h = 0.512$ m), highlighting that active turbulence dominates at scales smaller than L_O. At the end it assumes values comparable to the $\Delta x = 0.001$m, and so buoyancy dominates.

1.3 Governing Equations

The atmosphere can be described as a fluid system governed by the laws of continuum mechanics, which follow from the balance of mass, momentum, and energy. In integral form, a generic conservation law for a scalar or vector field $\psi(\mathbf{x}, t)$ over a control volume $\mathcal{V}$ reads

$$\frac{d}{dt}\int_{\mathcal{V}} \psi(\mathbf{x},t)\, dV = \int_{\mathcal{V}} b\, dV - \int_{\partial\mathcal{V}} \psi(\mathbf{x},t)\, \mathbf{u}\cdot\mathbf{n}\, d\Sigma, \tag{1.9}$$

i.e. the rate of change of ψ inside $\mathcal{V}$ equals the volumetric sources b minus the flux across the boundary $\partial\mathcal{V}$. Here $\mathbf{u}$ denotes the velocity field and $\mathbf{n}$ the outward normal vector.

By specializing this relation to mass, momentum, and internal energy, one obtains the Navier–Stokes system in local (differential) form:

$$\frac{\partial \rho}{\partial t} + \nabla\cdot(\rho\mathbf{u}) = 0, \tag{1.10}$$

$$\rho\frac{D\mathbf{u}}{Dt} = \nabla\cdot\boldsymbol{\sigma} + \rho\mathbf{f}, \tag{1.11}$$

$$\rho\frac{De}{Dt} = \nabla\cdot(k\nabla T) + r + \boldsymbol{\sigma} : \mathbf{D}, \tag{1.12}$$

where ρ is the mass density, $\mathbf{u}$ the velocity field, e the internal energy per unit mass, and $\mathbf{f}$ a generic body force, such as gravity. The operator

$$\frac{D}{Dt} = \frac{\partial}{\partial t} + \mathbf{u}\cdot\nabla$$

denotes the material derivative, which represents the rate of change following the motion of a fluid parcel.

The Cauchy stress tensor is written as

$$\boldsymbol{\sigma} = -p\,\mathbf{I} + 2\mu\mathbf{D},$$

where p denotes the thermodynamic pressure, μ the dynamic viscosity, and $\mathbf{D} = (\nabla\mathbf{u} + \nabla\mathbf{u}^T)/2$ the strain-rate tensor. In the energy equation (1.12), the first term on the right-hand side expresses heat conduction according to Fourier's law, with k the thermal conductivity; the second term, r, accounts for possible volumetric sources or sinks of heat, such as radiation or phase changes; while the last contribution, $\boldsymbol{\sigma} : \mathbf{D}$, represents the conversion of kinetic into internal energy through viscous dissipation.

The inherent nonlinearity of the Navier–Stokes equations generates motions across a broad range of scales. In the atmosphere, such dynamically coupled motions span planetary scales (Rossby waves, $\sim 10^4$ km), synoptic weather systems (cyclones and anticyclones, $\sim 10^3$ km), mesoscale convection ($\sim 10^2$ km), down to microscale turbu-

lence in the boundary layer ($\sim$ 1–10 m), and even sub-millimeter scales relevant for cloud microphysics and droplet interactions.

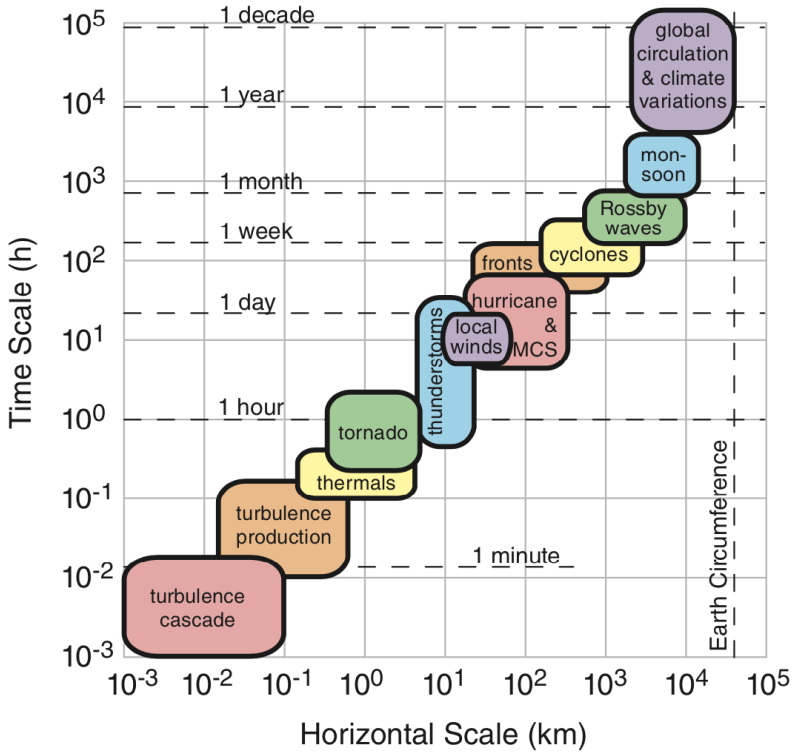

Figure 1.5: Horizontal range of scales of atmospheric dynamics. [9]

In this work, the focus is on the microscale regime, for which the *Boussinesq approximation* is appropriate.

This approximation is obtained by considering nearly incompressible flows ($M \ll 1$) with weak density variations, and neglecting compressibility effects everywhere except in the buoyancy force. Under this assumption, density is written as

$$\rho = \rho_0 \Big[1 - \alpha(\theta - \theta_0) \Big], \tag{1.13}$$

where ρ_0 is the reference density at potential temperature θ_0, and α is the thermal expansion coefficient (for an ideal gas, $\alpha = 1/\theta_0$). Replacing k with $\kappa = k/(\rho_0 c_p)$, the thermal diffusivity, the equations simplify into a system where acoustic modes are filtered out but buoyancy is retained as the driving force. The derivation of the Boussinesq system from the fully compressible Navier–Stokes equations is obtained through an asymptotic expansion in the limit of small Mach number. The starting point is a reference hydrostatic state, defined by a background pressure and density profile $(p_0(z), \rho_0(z))$ satisfying $\partial_z p_0 = -\rho_0 g$. The flow variables are then decomposed into this base state plus small perturbations of relative order $\varepsilon = \Delta\rho/\rho_0 \ll 1$. By expanding the governing equations in powers of ε and retaining only the leading-order terms, one finds that density variations may be neglected everywhere except in the buoyancy force,

while pressure reduces to a Lagrange multiplier enforcing incompressibility. At the same time, the continuity equation reduces to $\nabla \cdot \mathbf{u} = 0$, and acoustic modes are filtered out. The resulting model preserves the essential coupling between velocity and scalar fields (temperature and humidity), while eliminating compressibility effects, which is the hallmark of the Boussinesq approximation [17],[18].

The final governing equations used in our direct numerical simulations follow the Boussinesq formulation, written for the turbulent velocity field $\mathbf{u}(\mathbf{x}, t)$ and for two active scalars: the potential temperature $\theta(\mathbf{x}, t)$ and the vapor mixing ratio $q_v(\mathbf{x}, t) = \frac{\rho_v(\mathbf{x},t)}{\rho_0}$. The system reads [7]:

$$\nabla \cdot \mathbf{u} = 0, \tag{1.14}$$

$$\frac{\partial \mathbf{u}}{\partial t} + (\mathbf{u} \cdot \nabla)\mathbf{u} = -\frac{1}{\rho_0}\nabla p + \nu \nabla^2 \mathbf{u} - \mathcal{B}\,\mathbf{e}_z, \tag{1.15}$$

$$\frac{\partial \theta}{\partial t} + \mathbf{u} \cdot \nabla \theta = \kappa \nabla^2 \theta + \frac{\mathcal{L}}{c_p} C_d, \tag{1.16}$$

$$\frac{\partial q_v}{\partial t} + \mathbf{u} \cdot \nabla q_v = \kappa_v \nabla^2 q_v - C_d, \tag{1.17}$$

where ν is the kinematic viscosity of air, κ the thermal diffusivity, and κ_v the diffusivity of vapour mixing ratio. They are assumed constant. The buoyancy term is expressed as

$$\mathcal{B} = g\Big[\,\alpha(\theta - \theta_0) + \beta\,(q_v - q_0)\,\Big], \tag{1.18}$$

where $\beta = M_a/M_v - 1$, with M_a and M_v denoting the molar masses of dry air and water vapour, respectively. Furthermore $p(\mathbf{x}, t)$ is the pressure field, which in this formulation acts as a Lagrange multiplier enforcing the incompressibility constraint (1.14). Consequently, it is not computed explicitly during the time integration. Instead, the solution is projected onto the divergence-free subspace: $\Sigma = \{\boldsymbol{v} \in H(div, \Omega) \ : \nabla \cdot \boldsymbol{v} = 0\ \}$, thus eliminating the pressure gradient term from the numerical procedure while preserving the solenoidal nature of the velocity field. Next to take into account phase changes phenomenon, the $\mathcal{L}$ latent heat and $C_d(\mathbf{x}, t)$ condensation rate field are introduced. The condensation rate field is defined as the time derivative of the liquid water mass which is contained in each Δ^3 volume cell surrounding the grid points. It expresses the water mass depleted or absorbed rate for all the droplets in each cell [19]. Since droplets are advected by the flow, it must be determined in Lagrangian framework as :

$$C_d(\mathbf{x}, t) = \frac{1}{\Delta^3}\frac{dm_l(\mathbf{x}, t)}{dt} = \frac{4\pi\rho_l}{\Delta^3}\sum_{j=1}^{N_\Delta} R_j^2(\mathbf{X}_j(t))\frac{dR_j(\mathbf{X}_j(t))}{dt}, \tag{1.19}$$

where R_j, $\mathbf{X}_j$, and N_Δ are respectively the radius, the coordinate of the j-th droplet,

and the number of droplets within the cell. Since the condensation rate field appears in Eqs (1.16) and (1.17) , it must be expressed in the Eulerian framework. This is achieved by interpolating the droplet-based quantities onto the fixed grid points using a second-order Lagrange polynomial scheme.

1.3.1 Lagrangian Droplets

The liquid phase is represented by a population of cloud droplets tracked individually in a Lagrangian framework. Each droplet is treated as a small, spherical particle whose dynamics is governed by the local fluid velocity and by buoyancy forces. The motion of the i-th droplet is described by the following set of equations:

$$\frac{d\mathbf{X}_i}{dt} = \boldsymbol{V}_i, \tag{1.20}$$

$$\frac{d\boldsymbol{V}_i}{dt} = \frac{\mathbf{u}(\mathbf{X}_i, t) - \boldsymbol{V}_i}{\tau_i} + \left(1 - \frac{\rho_a}{\rho_w}\right) g\, \mathbf{e}_z, \tag{1.21}$$

where $\mathbf{X}_i$ and $\boldsymbol{V}_i$ denote the droplet position and velocity, respectively. The first term on the right-hand side represents the Stokes drag exerted by the surrounding air, while the second accounts for the effective gravitational settling reduced by buoyancy. The droplet relaxation time τ_i is given by

$$\tau_i = \frac{2}{9}\,\frac{\rho_w}{\rho_a}\,\frac{R_i^2}{\nu}, \tag{1.22}$$

which defines the characteristic response timescale to variations in the carrier flow. This formulation assumes small particle Reynolds numbers and neglects droplet–droplet interactions in the dynamical coupling.

The evolution of the droplet radius is governed by condensation and evaporation processes,

$$\frac{dR_i}{dt} = \frac{K_s}{R_i}\left(s - \frac{A}{R_i} + \frac{Br_d^3}{R_i^3}\right), \tag{1.23}$$

where s is the local supersaturation, A and B are the curvature (Kelvin) and solute (Raoult) coefficients, and r_d is the dry nucleus radius. This equation expresses the diffusive growth of droplets due to vapor exchange with the environment, including both surface tension and hygroscopic effects.

Further details on the microphysical parameterizations and the derivation of the droplet growth law are reported in Appendix A.

1.4 Internal Gravity Waves

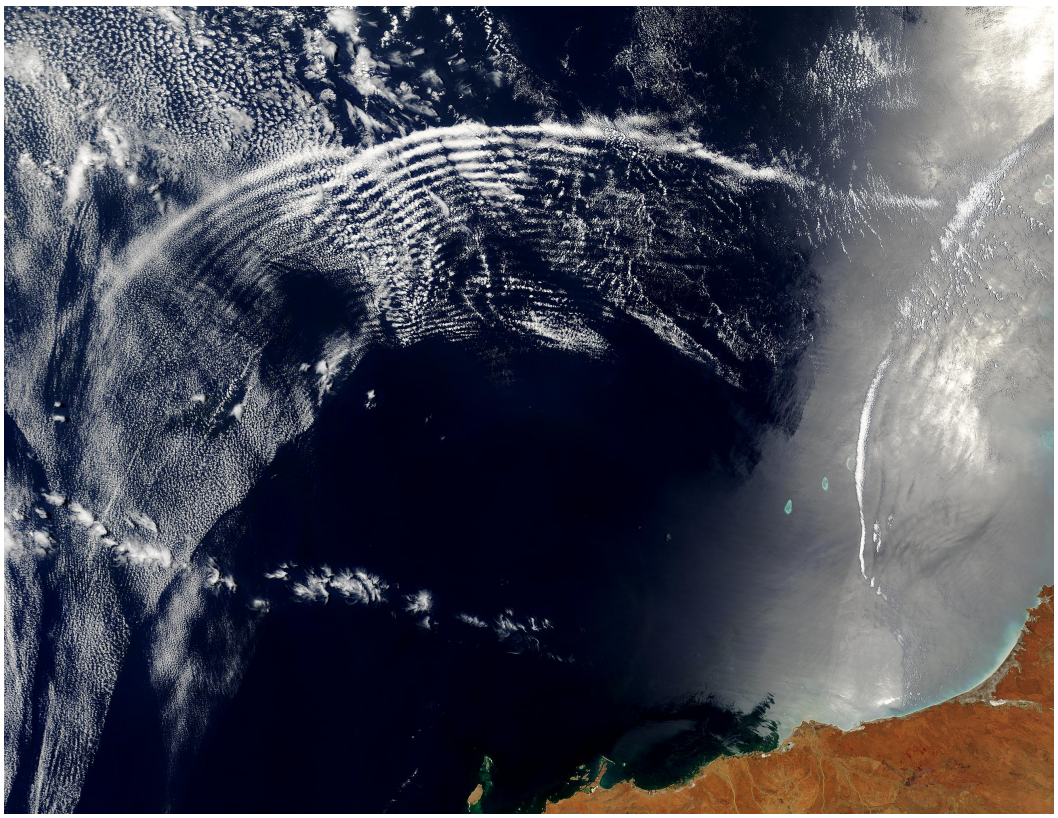

Figure 1.6: Atmospheric gravity waves and internal ocean waves off Australia, as seen by the MODIS instrument aboard the Terra satellite on November 11, 2003. Image courtesy of Jacques Descloitres and the MODIS Rapid Response Team, NASA/GSFC [20].

As previously discussed in Section 1.1.2, vertical displacements of air parcels in a stably stratified fluid experience a restoring buoyant acceleration proportional to the Brunt–Väisälä frequency $\mathcal{N}$. While in parcel theory this mechanism describes local oscillations of displaced fluid elements, it can also manifest as propagating disturbances known as *internal gravity waves* (IGWs). Unlike surface waves, which propagate along a sharp density interface, IGWs exist within continuously stratified media, where the vertical gradients of temperature and density provide the restoring force that supports their oscillation. The frequency of these waves is bounded by $\mathcal{N}$, which sets the natural timescale for vertical motions in the background atmosphere. Under the linear approximation of small-amplitude perturbations, the restoring buoyancy and pressure gradients combine to sustain oscillations that can propagate energy and momentum both vertically and horizontally. Such waves play a fundamental role in coupling large-scale stratification with small-scale turbulence and mixing, as already outlined in Section 1.2. They redistribute heat, momentum, and moisture, interact with convection and shear, and influence cloud-layer dynamics. In cloudy boundary layers,

IGWs modulate the vertical transport of vapour and temperature, thereby affecting droplet growth and the entrainment of dry air. Their nonlinear evolution can lead to wave breaking and local overturning, producing patches of turbulence that enhance mixing across cloudy–clear air interfaces. In this context, IGWs represent the dynamical bridge between the mean stratification and the turbulent fluctuations observed in the simulations. The present section develops the linear theory of IGWs based on the Boussinesq approximation and the Brunt–Väisälä restoring mechanism, providing a foundation for understanding their dispersion properties and energy exchange. This theoretical framework will later be complemented by weakly nonlinear considerations, necessary to capture the transition from organized wave motion to turbulence and mixing within the cloud–clear air interface.

Linear IGW

Let $\mathbf{u} = (u_h, w)$ be the velocity field (horizontal u_h and vertical w), $\hat{p}$ the kinematic pressure (pressure divided by ρ_0), and θ the potential temperature. The governing equations under the Boussinesq approximation are

$$\nabla \cdot \mathbf{u} = 0, \tag{1.24}$$

$$\frac{D\mathbf{u}}{Dt} = -\nabla \hat{p} \; + \; \nu \nabla^2 \mathbf{u} \; + \; b\, \mathbf{e}_z, \qquad b \; \equiv \; g\, \alpha\, [\theta - \theta_0], \tag{1.25}$$

$$\frac{D\theta}{Dt} = \kappa \nabla^2 \theta, \tag{1.26}$$

with the material derivative $\frac{D}{Dt} = \partial_t + \mathbf{u} \cdot \nabla$, $\nabla = (\partial_{x_h}, \partial_z)$, and $\nabla^2 = \partial^2_{x_h} + \partial^2_z$. Following [21, 22, 23] we consider a horizontally homogeneous and vertically varying background flow, represented by the mean (or base state) fields

$$\mathbf{U}(z) = U(z)\, \mathbf{e}_h, \qquad \overline{\theta}(z), \qquad \overline{p}(z),$$

which depend only on the vertical coordinate z. Here, $\mathbf{U}(z)$ denotes the mean velocity profile aligned with the horizontal direction $\mathbf{e}_h$, $\overline{\theta}(z)$ is the mean potential temperature profile, and $\overline{p}(z)$ the mean pressure field. These background quantities satisfy hydrostatic balance:

$$\frac{d\overline{p}}{dz} \; = \; -\, g\, \frac{\overline{\theta}(z) - \theta_0}{\theta_0},$$

with θ_0 a reference potential temperature. Small-scale departures from the base state are introduced as perturbations:

$$\mathbf{u}' = \mathbf{u} - \mathbf{U}, \qquad \theta' = \theta - \overline{\theta}, \qquad p' = p - \overline{p}.$$

We recall that the stability of the base state is characterised by the Brunt–Väisälä frequency,

$$\mathcal{N}^2(z) \;=\; \frac{g}{\theta_0}\,\frac{d\overline{\theta}}{dz}.$$

Linearising the governing equations around the base state yields the system

$$\nabla \cdot \mathbf{u}' = 0, \tag{1.27}$$

$$\partial_t \mathbf{u}' + U\,\partial_{x_h}\mathbf{u}' + w'\,U'(z)\,\mathbf{e}_h = -\nabla p' + \nu\,\nabla^2\mathbf{u}' + \frac{g}{\theta_0}\,\theta'\,\mathbf{e}_z, \tag{1.28}$$

$$\partial_t \theta' + U\,\partial_{x_h}\theta' + w'\,\frac{d\overline{\theta}}{dz} = \kappa\,\nabla^2\theta'. \tag{1.29}$$

We seek perturbations of the form

$$\{u', w', p', \theta'\}(x_h, z, t) = \{\hat{u}(z), \hat{w}(z), \hat{p}(z), \hat{\theta}(z)\}\, e^{\,i(kx_h - \omega t)},$$

and from $\mathcal{N}^2(z) = \dfrac{g}{\theta_0}\dfrac{d\overline{\theta}}{dz}$, and substituting into the linear viscous Boussinesq system

$$\begin{cases} \partial_{x_h} u' + \partial_z w' = 0, \\ \partial_t u' + U\,\partial_{x_h} u' + w'U' = -\,\partial_{x_h} p' + \nu\nabla^2 u', \\ \partial_t w' + U\,\partial_{x_h} w' = -\,\partial_z p' + \dfrac{g}{\theta_0}\,\theta' + \nu\nabla^2 w', \\ \partial_t \theta' + U\,\partial_{x_h}\theta' + \overline{\theta}'\,w' = \kappa\nabla^2\theta', \end{cases}$$

gives (with $'$ now meaning d/dz and $\nabla^2 \to \partial_z^2 - k^2$)

$$ik\,\hat{u} + \hat{w}' = 0, \tag{1.30}$$

$$\big(-i\omega + ikU\big)\hat{u} + U'\hat{w} = -ik\,\hat{p} + \nu(\hat{u}'' - k^2\hat{u}), \tag{1.31}$$

$$\big(-i\omega + ikU\big)\hat{w} = -\,\hat{p}' + \frac{g}{\theta_0}\hat{\theta} + \nu(\hat{w}'' - k^2\hat{w}), \tag{1.32}$$

$$\big(-i\omega + ikU\big)\hat{\theta} + \overline{\theta}'\,\hat{w} = \kappa(\hat{\theta}'' - k^2\hat{\theta}). \tag{1.33}$$

Uniform background ($U, \mathcal{N}$ constants): For vertical plane waves e^{imz}, $\hat{f}'' - k^2\hat{f} = -K^2\hat{f}$ with $K^2 = k^2 + m^2$. Equations (1.30)–(1.33) reduce to the algebraic system

$$\mathbf{M}(k, m, \omega)\begin{pmatrix} \hat{u} \\ \hat{w} \\ \hat{p} \\ \hat{\theta} \end{pmatrix} = \mathbf{0},$$

where

$$\mathbf{M} = \begin{pmatrix} k & m & 0 & 0 \\ (-i\omega + ikU + \nu K^2) & 0 & ik & 0 \\ 0 & (-i\omega + ikU + \nu K^2) & im & -\dfrac{g}{\theta_0} \\ 0 & \overline{\theta}' & 0 & (-i\omega + ikU + \kappa K^2) \end{pmatrix}.$$

Nontrivial solutions require $\det \mathbf{M} = 0$, which (using $\mathcal{N}^2 = \dfrac{g}{\theta_0}\,\overline{\theta}'$) yields the viscously/thermally damped dispersion relation

$$\Big(\omega - kU - i\nu K^2\Big)\Big(\omega - kU - i\kappa K^2\Big) \;=\; \mathcal{N}^2\,\frac{k^2}{K^2}\,. \tag{1.34}$$

In the weak–damping limit,

$$\omega \;\approx\; kU \;+\; \mathcal{N}\,\frac{k}{K} \;-\; i\,\frac{\nu+\kappa}{2}\,K^2.$$

Variable background ($U(z), N(z)$): Taylor–Goldstein via solvability. Set $\nu = \kappa = 0$ to derive the standard Taylor–Goldstein (TG) equation.

From (1.30), $\hat{u} = -(1/ik)\hat{w}'$. From (1.31), solve for $\hat{p}$:

$$-\,i(\omega - kU)\,\hat{u} + U'\hat{w} = -ik\,\hat{p} \;\;\Rightarrow\;\; \hat{p} = \frac{i}{k}\Big(\frac{\omega - kU}{k}\,\hat{w}' + U'\hat{w}\Big).$$

Differentiate in z:

$$\hat{p}' = \frac{i}{k}\Big(\frac{\omega - kU}{k}\,\hat{w}'' + U''\hat{w}\Big),$$

where the $U'\hat{w}'$ terms cancel. From (1.33) (inviscid), $\hat{\theta} = -\,\dfrac{\overline{\theta}'}{-i\omega + ikU}\,\hat{w} = \dfrac{\overline{\theta}'}{i(\omega - kU)}\,\hat{w}$.

Insert $\hat{p}'$ and $\hat{\theta}$ into (1.32) (inviscid):

$$-\,i(\omega - kU)\,\hat{w} = -\,\hat{p}' + \frac{g}{\theta_0}\hat{\theta} = -\,\frac{i}{k}\Big(\frac{\omega - kU}{k}\,\hat{w}'' + U''\hat{w}\Big) + \frac{\mathcal{N}^2}{i(\omega - kU)}\,\hat{w}.$$

After simple algebra and introducing the phase speed $c = \omega/k$, this reduces to

$$\Big(U - c\Big)\Big(\hat{w}'' - k^2\hat{w}\Big) \;-\; U''\,\hat{w} \;+\; \frac{\mathcal{N}^2(z)}{U - c}\,\hat{w} \;=\; 0, \qquad c = \frac{\omega}{k}. \tag{1.35}$$

Equation (1.35) is the Taylor–Goldstein eigenproblem (inviscid, Boussinesq, 2D). Setting $U \equiv 0$, $\mathcal{N} \equiv \mathcal{N}_0$ and $\hat{w} \sim e^{imz}$ recovers the classical internal-wave dispersion relation:

$$\boxed{\omega^2 = \mathcal{N}_0^2\,\frac{k^2}{k^2 + m^2}}\,. \tag{1.36}$$

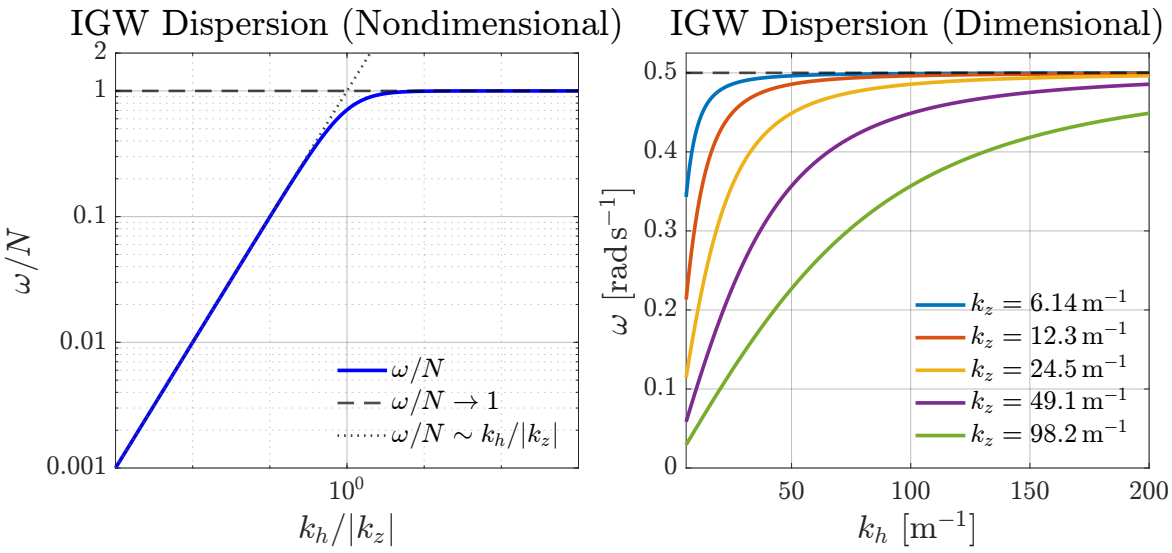

Figure 1.7: Dispersion relation plotted non-dimensionally on the left and dispersion curves at fixed k_z, with a reference $\mathcal{N} = 0.5$ rad/s.

Trapped internal waves

An illustrative case is a stratification confined to a finite layer of thickness $2H$:

$$\mathcal{N}^2(z) = \begin{cases} \mathcal{N}_0^2 & \text{for } |z| \le H, \\ 0 & \text{for } |z| > H. \end{cases}$$

then we have solutions:

$$\hat{w}(z) = \begin{cases} \mathcal{A}\, e^{-kz}, & z > H, \\ \mathcal{B}_1 \cos(mz) + \mathcal{B}_2 \sin(mz), & |z| \le H, \\ \mathcal{C}\, e^{kz}, & z < -H, \end{cases} \tag{1.37}$$

with $m = \sqrt{\mathcal{N}_0^2 - \omega^2}/c_x$. Imposing continuity of $\hat{w}$ and $\partial_z \hat{w}$ at $z = \pm H$ yields the dispersion relation for trapped modes. The solutions (1.37) correspond to vertically confined internal waves, which become evanescent outside the stratified layer and are therefore often referred to as *ducted* waves. This scenario shares key features with the present configuration, most notably the strong spatial localisation of stratification around a thin interfacial region. Unlike the idealised setting, however, in our simulations the temperature field evolves dynamically and directly interacts with the velocity field. As a consequence, both the thickness of the stratified layer and the local buoyancy frequency vary in time, so that the degree of wave trapping is not constant but adjusts continuously as mixing progresses.

Consistency with the present setup. The linear theory developed above is strictly valid under the assumptions of an inviscid Boussinesq fluid, a single scalar stratification,

and a horizontally uniform background state. In the model presented in this work (1.3), some of these assumptions are relaxed or different. In particular:

- the mean shear is absent ($U(z) = 0$);
- viscosity ν and scalar diffusivities are finite and constant, leading to exponential damping of the form

$$e^{-\frac{1}{2}(\nu+\kappa)K^2 t}, \qquad K^2 = k_h^2 + m^2;$$

- buoyancy is influenced by two scalars, potential temperature θ and vapour mixing ratio q_v, both contributing to the effective stratification.

More explicitly, the buoyancy perturbation entering the momentum equation is

$$b' = \frac{g}{\theta_0}\,\theta' + g\beta\, q_v',$$

where $\beta = M_a/M_v - 1$ depends on the molar masses of air and vapour.

Moist air buoyancy frequency The effective buoyancy contribution needs to be adjusted when atmospheric moisture is present. This effect is specifically taken into consideration in our formulation, in accordance with the methods of [24], who examined the impact of moisture in both unsaturated and saturated situations, and of [25], who approached this specific problem through mixture theory. We follow the latter approach, expressing buoyancy in terms of the virtual potential temperature $\theta_v \approx \theta(1 + 0.61\, q_v)$, which allows the contribution of water vapour to be incorporated additively into the effective static stability. In contrast to [24], phase-change effects are already included in the prognostic potential temperature equation used here, so that the background gradient $\overline{\theta}(z)$ implicitly accounts for latent heating and cooling. Linearisation of the scalar equations about the background fields $\overline{\theta}(z)$ and $\overline{q_v}(z)$ gives

$$\mathcal{N}_\theta^2 = \frac{g}{\theta_0}\frac{d\overline{\theta}}{dz}, \qquad \mathcal{N}_{q_v}^2 = g\beta\,\frac{d\overline{q_v}}{dz},$$

with $\beta \simeq 0.61$ accounting for the effect of water vapour on air density. Hence, the squared effective buoyancy frequency naturally follows as

$$\mathcal{N}_{\text{eff}}^2 = \mathcal{N}_\theta^2 + \mathcal{N}_{q_v}^2, \tag{1.38}$$

reflecting the combined stabilising or destabilising contributions of temperature and moisture gradients. Substituting this expression into the linearised Boussinesq equations

leads to the moist internal gravity wave dispersion relation

$$\omega^2 \simeq \mathcal{N}_{\text{eff}}^2 \, \frac{k_h^2}{k_h^2 + m^2}, \tag{1.39}$$

where $\mathcal{N}_{\text{eff}}^2$ encapsulates the effective static stability of moist air. This moist extension of the classical IGW dispersion relation provides the theoretical benchmark against which the DNS results will be compared in later chapters.

Nonlinear considerations for internal gravity waves

Weakly nonlinear framework The linear theory holds only for infinitesimal amplitude disturbances. When the amplitude becomes finite but small, non-linear terms arising from advection in the material derivative start to play a role. This regime is called *weakly non-linear*. Perturbation theory can then be applied.

For a field variable ψ, the governing equation may be schematically written as

$$L(\partial_x, \partial_z, \partial_t)\psi = N(\psi), \tag{1.40}$$

where L is a linear operator and N collects quadratic non-linearities .

A perturbative ansatz is introduced:

$$\psi = A_0\Big(\psi_0 + A_0\psi_1 + A_0^2\psi_2 + \dots\Big), \tag{1.41}$$

where we have taken as a perturbative parameter the wave-amplitude A_0. The corresponding weakly non-linear dispersion relation takes the form :

$$\omega^2 = \omega_0^2\Big(1 + \sigma_2 A_0^2 + \dots\Big), \tag{1.42}$$

where in this expansion we have taken advantage of symmetry (there's no difference between forward or backward moving waves; furthermore, odd powers of A_0 vanish). Then by supposing time-periodic solutions, it yields to $L \equiv L(\omega)$. And expanding the operators of (1.40) we obtain:

$$L(\omega) = L_0(\omega_0) + A_0^2 L_2(\omega_0, \sigma_2) + \ ..., \tag{1.43}$$

$$\frac{1}{A_0}N(f) = A_0 N_1(f_0) + A_0^2 N_2(f_0, f_1) + \ ..., \tag{1.44}$$

which substituting in (1.40):

$$A_0(L_0 f_0) + A_0^2(L_0 f_1 - N_1(f_0)) + A_0^3(L_0 f_2 + L_2 f_0 - N_2(f_0, f_1)) + \ .... = 0. \tag{1.45}$$

As leading order (A_0) we have:

$$L_0 f_0 = 0,$$

which is an eigenvalue problem yielding the linear theory's dispersion relation (1.36). So the solution $f_0 \propto e^{\pm i\phi}$, with $\phi = kx - \omega t$.

At the next order (A_0^2) instead:

$$L_0 f_1 = N_1(f_0),$$

from which we can assess that f_1 is dependent on non-linear interaction between f_0 (small amplitude waves), in particular the non-linearity is a quadratic term so f_1 is a linear combination of $e^{\pm 2\phi}$, plus a constant. Thus, physically non-linear wave-wave interactions can excite superharmonic waves with double the wavenumber and add a mean disturbance. At the order A_0^3, we have quadratic interaction between f_0 and f_1 exciting waves proportional to $e^{\pm i\phi}$ and $e^{\pm 3i\phi}$, furthermore σ_2 is chosen to cancel out secular terms, which are unphysical.

Chapter 2

Numerical Methods and Post-Processing Techniques

2.1 Numerical Method

The numerical method relies on a Fourier–Galerkin approach implemented within a pseudo-spectral DNS framework. The software has been developed by the PHILOFLUID research group at PoliTO, and further details on the code are available in [26, 27]. Spatial derivatives are computed with spectral accuracy on a triply periodic domain, while non-linear products are evaluated in physical space to optimize efficiency. Time integration is performed using a second-order Runge–Kutta scheme, with non-linear and buoyancy contributions treated explicitly and viscous diffusion handled through an integrating factor for enhanced stability. Incompressibility is enforced via a Helmholtz projection onto the divergence-free subspace, allowing the pressure term—acting as a Lagrange multiplier for the incompressibility constraint—to be eliminated from the numerical formulation. Scalar transport equations for temperature and water vapour are advanced concurrently using the same scheme, including their coupling through buoyancy and phase-change terms. Next, we provide a brief mathematical description of the method. For further details, the reader may refer to [28] for the spectral approach and to [29] for a rigorous variational formulation.

Variational (MWR/Galerkin) formulation Let $\Omega = [0, L]^3$ with periodic boundary conditions. Define the trial and test spaces

$$\boldsymbol{V} := \left[H^1_{\mathrm{per}}(\Omega)\right]^3, \qquad Q := L^2_{\mathrm{per}}(\Omega) \,/\, \mathbb{R},$$

and the divergence–free subspace

$$\boldsymbol{V}_{\mathrm{div}} := \left\{\boldsymbol{v} \in \boldsymbol{V} : \nabla\cdot\boldsymbol{v} = 0\right\}.$$

Find $(\boldsymbol{u}, p, \theta, q_v) \in \boldsymbol{V} \times Q \times H^1_{\mathrm{per}}(\Omega) \times H^1_{\mathrm{per}}(\Omega)$ such that, for all test functions $(\boldsymbol{\varphi}, \xi, \psi_\theta, \psi_q)$ in the corresponding spaces,

$$(\partial_t \boldsymbol{u}, \boldsymbol{\varphi}) \;+\; \Big((\boldsymbol{u}\cdot\nabla)\boldsymbol{u}, \boldsymbol{\varphi}\Big) \;+\; \nu\,(\nabla \boldsymbol{u}, \nabla \boldsymbol{\varphi}) \;-\; (p, \nabla\cdot\boldsymbol{\varphi}) \;=\; (\boldsymbol{f}_b(\theta, q_v), \boldsymbol{\varphi}), \tag{2.1}$$

$$(\nabla\cdot\boldsymbol{u}, \xi) = 0, \tag{2.2}$$

$$(\partial_t \theta, \psi_\theta) \;+\; (\boldsymbol{u}\cdot\nabla\theta, \psi_\theta) \;+\; \kappa_\theta(\nabla\theta, \nabla\psi_\theta) \;-\; \Big((\nabla\langle\theta\rangle)\cdot\boldsymbol{u}, \psi_\theta\Big) \;=\; \Big(\tfrac{\mathcal{L}}{c_p} C_d, \psi_\theta\Big), \tag{2.3}$$

$$(\partial_t q_v, \psi_q) \;+\; (\boldsymbol{u}\cdot\nabla q_v, \psi_q) \;+\; \kappa_q(\nabla q_v, \nabla\psi_q) \;=\; (-C_d, \psi_q). \tag{2.4}$$

Here $(\cdot,\cdot)$ denotes the $L^2(\Omega)$ inner product and $\boldsymbol{f}_b(\theta, q_v) = \mathcal{B}(\theta, q_v)\,\boldsymbol{e}_z$ is the buoyancy force. On a periodic domain, all boundary terms vanish after integration by parts.

If we restrict the test space in (2.1) to $\boldsymbol{\varphi} \in \boldsymbol{V}_{\mathrm{div}}$, then

$$(p, \nabla\cdot\boldsymbol{\varphi}) = 0,$$

so the pressure term drops out of the weak momentum equation. Equivalently, introducing the L^2–orthogonal projector

$$\mathbb{P} : \Big[L^2_{\mathrm{per}}(\Omega)\Big]^3 \to \boldsymbol{V}_{\mathrm{div}},$$

the momentum balance may be written, in strong form, as

$$\partial_t \boldsymbol{u} \;=\; \mathbb{P}\Big(-(\boldsymbol{u}\cdot\nabla)\boldsymbol{u} + \nu\Delta\boldsymbol{u} + \boldsymbol{f}_b(\theta, q_v)\Big), \quad \nabla\cdot\boldsymbol{u} = 0,$$

which makes explicit that the pressure only enforces the constraint and is not advanced as a prognostic variable.

Fourier representation and pressure elimination Let $\widehat{\cdot}(\boldsymbol{k})$ denote the Fourier transform on Ω and $\boldsymbol{k} \in \frac{2\pi}{L}\mathbb{Z}^3$ the wavevector. The incompressible Navier–Stokes equations with buoyancy read, in Fourier space,

$$\partial_t \widehat{\boldsymbol{u}}(\boldsymbol{k}) = -\nu|\boldsymbol{k}|^2 \widehat{\boldsymbol{u}}(\boldsymbol{k}) \;-\; \frac{i\,\boldsymbol{k}}{\rho_0}\,\widehat{p}(\boldsymbol{k}) \;+\; \widehat{\boldsymbol{N}}(\boldsymbol{k}) \;+\; \widehat{\boldsymbol{f}}_b(\boldsymbol{k}), \tag{2.5}$$

$$\boldsymbol{k}\cdot\widehat{\boldsymbol{u}}(\boldsymbol{k}) = 0, \tag{2.6}$$

where $\widehat{\boldsymbol{N}}$ collects the nonlinear convective contributions. Define the Helmholtz projector

$$\mathbb{P}(\boldsymbol{k}) \;:=\; \boldsymbol{I} \;-\; \frac{\boldsymbol{k}\,\boldsymbol{k}^{\top}}{|\boldsymbol{k}|^2} \qquad (\boldsymbol{k} \neq \boldsymbol{0}),$$

which satisfies $\mathbb{P}(\boldsymbol{k})\,\widehat{\boldsymbol{u}} = \widehat{\boldsymbol{u}}$ iff $\boldsymbol{k}\cdot\widehat{\boldsymbol{u}} = 0$. Applying $\mathbb{P}(\boldsymbol{k})$ to (2.5) and using $\mathbb{P}(\boldsymbol{k})\,\boldsymbol{k} = \boldsymbol{0}$, the pressure term vanishes:

$$\partial_t \widehat{\boldsymbol{u}}(\boldsymbol{k}) \;=\; -\nu|\boldsymbol{k}|^2\widehat{\boldsymbol{u}}(\boldsymbol{k}) \;+\; \mathbb{P}(\boldsymbol{k})\Big[\widehat{\boldsymbol{N}}(\boldsymbol{k}) + \widehat{\boldsymbol{f}}_b(\boldsymbol{k})\Big], \qquad \boldsymbol{k} \neq \boldsymbol{0}.$$

If needed, the pressure can be recovered a posteriori from the Poisson relation obtained by taking the divergence of the momentum equation:

$$-|\boldsymbol{k}|^2\,\widehat{p}(\boldsymbol{k}) \;=\; -\,i\,\rho_0\,\boldsymbol{k}\cdot\Big[\widehat{\boldsymbol{N}}(\boldsymbol{k}) + \widehat{\boldsymbol{f}}_b(\boldsymbol{k})\Big], \qquad \Rightarrow \qquad \widehat{p}(\boldsymbol{k}) \;=\; -\,i\,\rho_0\,\frac{\boldsymbol{k}\cdot\big[\widehat{\boldsymbol{N}} + \widehat{\boldsymbol{f}}_b\big]}{|\boldsymbol{k}|^2}.$$

For the scalars one has, in Fourier space,

$$\begin{aligned}
\partial_t\widehat{\theta}(\boldsymbol{k}) &= -\kappa_\theta|\boldsymbol{k}|^2\widehat{\theta}(\boldsymbol{k}) \;+\; \widehat{S}_\theta(\boldsymbol{k}), \qquad \widehat{S}_\theta := -\,\widehat{\boldsymbol{u}\cdot\nabla\theta} \;-\; \widehat{(\nabla\langle\theta\rangle)\cdot\boldsymbol{u}} \;+\; \widehat{\tfrac{\mathcal{L}}{c_p}C_d},\\
\partial_t\widehat{q}_v(\boldsymbol{k}) &= -\kappa_q|\boldsymbol{k}|^2\widehat{q}_v(\boldsymbol{k}) \;-\; \widehat{\boldsymbol{u}\cdot\nabla q_v} \;-\; \widehat{C_d}.
\end{aligned}$$

No projection is needed for scalars; the coupling to momentum appears through $\widehat{\boldsymbol{f}}_b$.

In practice, the algorithm advances $\widehat{\boldsymbol{u}}$ by applying $\mathbb{P}(\boldsymbol{k})$ to the nonlinear and buoyancy contributions at each Runge–Kutta stage, while diffusion is handled by the factor $e^{-\nu|\boldsymbol{k}|^2\Delta t}$ (and analogously for the scalar diffusivities). The pseudo-spectral method represents the solution as a truncated Fourier series on a periodic domain:

$$\mathbf{u}_N(\mathbf{x},t) = \sum_{k_1=-N/2}^{N/2-1}\;\sum_{k_2=-N/2}^{N/2-1}\;\sum_{k_3=-N/2}^{N/2-1} \widehat{\mathbf{u}}_{\boldsymbol{k}}(t)\,e^{i\boldsymbol{k}\cdot\mathbf{x}}.$$

Spatial derivatives are computed exactly in spectral space by multiplication with ik_j. Nonlinear terms, however, are evaluated in physical space to avoid expensive convolutions, and then transformed back to Fourier space via FFTs. The product of two fields in physical space corresponds to a convolution in spectral space, which introduces aliasing errors due to mode folding beyond the truncation wavenumber. To eliminate aliasing, the classical 3/2 padding rule is applied: the spectral array is zero-padded from size N to $M = (3/2)N$ before performing the inverse FFT. The nonlinear product is then computed in physical space, and the result is transformed back to spectral space and truncated to the original N modes. This procedure guarantees that no spurious modes are reintroduced into the resolved range.

The implementation combines this dealiasing strategy with a parallelization scheme based on a one-dimensional domain decomposition using MPI. In this approach, each process stores a slab of data corresponding to a subset of wavenumbers in one direction, while retaining full data along the other two directions locally. This layout enables two out of three FFTs to be performed entirely in-core, requiring only two global transpositions per timestep. Moreover, the parallel dealiased implementation follows

the technique introduced by Iovieno et al. [26], where the dealiasing step is merged with data transposition. This integration reduces communication overhead and improves scalability on distributed-memory systems. Temporal advancement uses a second-order Runge–Kutta (RK2) scheme for the nonlinear and buoyancy terms, combined with an integrating factor to treat viscous and diffusive terms implicitly in spectral space. Denoting $\widehat{\mathbf{u}}^n$ the velocity at timestep n and $\mathcal{N}(\cdot)$ the nonlinear plus buoyancy contributions after projection, the algorithm reads:

$$\widehat{\mathbf{u}}^* = e^{-\nu|\boldsymbol{k}|^2\Delta t}\,\widehat{\mathbf{u}}^n + \Delta t\, e^{-\nu|\boldsymbol{k}|^2\Delta t}\,\mathbb{P}(\mathcal{N}^n),$$
$$\widehat{\mathbf{u}}^{n+1} = e^{-\nu|\boldsymbol{k}|^2\Delta t}\,\widehat{\mathbf{u}}^n + \frac{\Delta t}{2} e^{-\nu|\boldsymbol{k}|^2\Delta t}\left[\mathbb{P}(\mathcal{N}^n) + \mathbb{P}(\mathcal{N}^*)\right].$$

An analogous update is applied to scalar fields with their respective diffusivities. This formulation is unconditionally stable for the linear viscous term, while the time-step restriction comes from the advective CFL condition.

2.2 Simulations set-up

The simulations are performed in a triply periodic domain of size $L_{x_1} \times L_{x_2} \times L_{x_3}$, discretized with $N_1 \times N_2 \times N_3$ grid points (see Table 2.1). The focus is on the turbulent mixing between a cloudy region and a clear–air region under different stratification conditions. To this end, we vary the initial temperature jump ΔT across the cloud–clear interface, the energy ratio $E_{\text{cloud}}/E_{\text{clear}}$ between the two sides, and the droplet population type (monodisperse or polydisperse), as summarized in Table 2.2.

2.2.1 Initial conditions

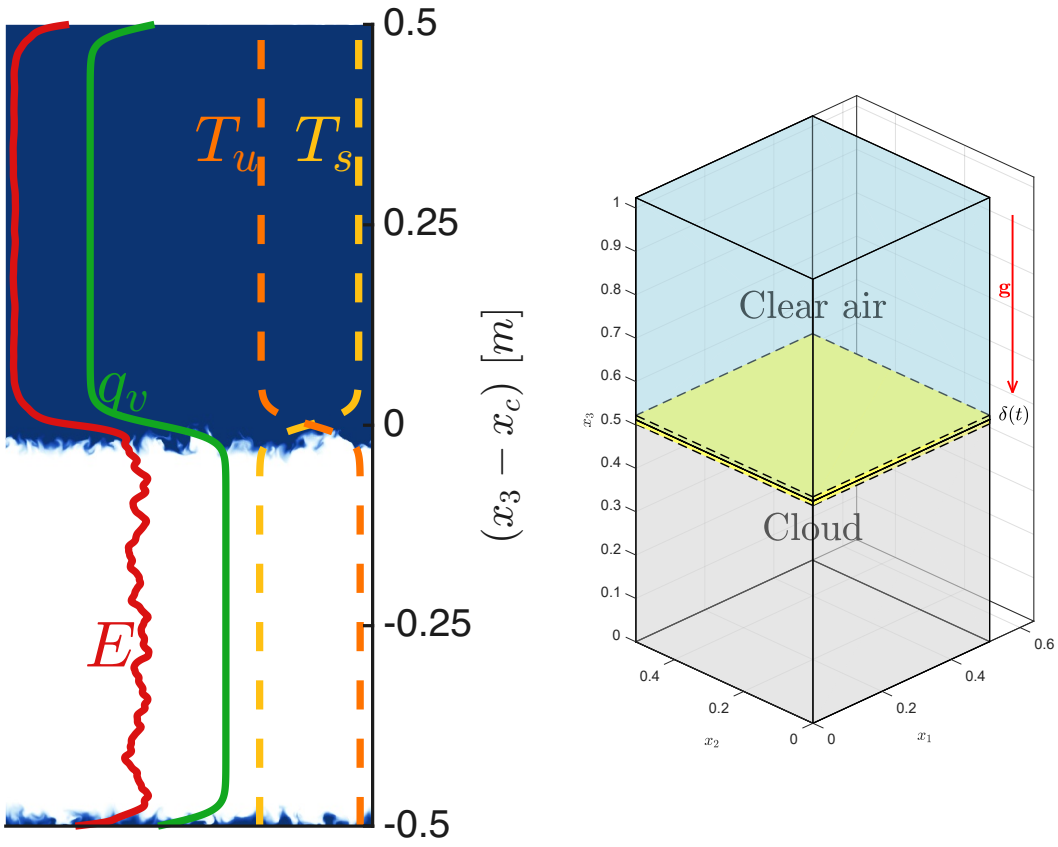

Figure 2.1: Initial distribution of kinetic energy (in red), water vapour content (in green), and stable (T_s) or unstable (T_u) temperature on the left. Computational domain representation on the right where $\delta(t)$ is the mixing layer thickness. Figures adapted from [6].

The computational domain is divided into two regions along the vertical direction, x_3: a *cloudy region* and a *clear-air region*. Each region is initialized as a separate cube of size N_1^3 containing homogeneous isotropic turbulence (HIT) with zero mean flow and prescribed levels of turbulent kinetic energy (TKE), consistent with the desired energy ratio $E_{\text{cloud}}/E_{\text{clear}}$. These two turbulent cubes are then smoothly connected along the

inhomogeneous direction (x_3) using a transition function, such as a hyperbolic tangent, to form the final composite domain [30].

The smoothing is achieved through the following function:

$$p(x_3) = 1 + \tanh\left[a\frac{x_3}{L_{x_3}}\right]\tanh\left[a\left(\frac{x_3}{L_{x_3}} - \frac{1}{2}\right)\right]\tanh\left[a\left(\frac{x_3}{L_{x_3}} - 1\right)\right], \tag{2.7}$$

where $a = 12\pi$ controls the steepness of the transition layer.

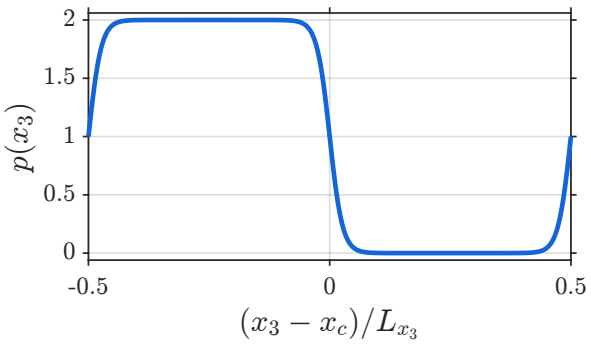

Figure 2.2: Smoothing function plot vs $((x_3 - x_c)/L_{x_3})$.

At $t = 0$, the velocity and vapor fields are initialized as

$$\mathbf{u}(\mathbf{x}, 0) = \mathbf{u}^c(\mathbf{x})\, p(x_3) + \mathbf{u}^a(\mathbf{x})\sqrt{1 - p^2(x_3)}, \tag{2.8}$$

$$\rho_v(\mathbf{x}, 0) = \rho_v^c(\mathbf{x})\, p(x_3) + \rho_v^a(\mathbf{x})\sqrt{1 - p^2(x_3)}, \tag{2.9}$$

where the superscripts c and a refer to the cloudy and clear-air regions, respectively. The initial vapour densities are given by

$$\rho_v^c(\mathbf{x}) = \rho_{vs}(\theta_1)RH_1, \qquad \rho_v^a(\mathbf{x}) = \rho_{vs}(\theta_2)RH_2,$$

where ρ_{vs} is the saturation vapor density at the local temperature θ, and RH denotes the relative humidity of each region.

The mean temperature profile is prescribed as

$$\theta(x_3, 0) = \frac{\Delta\theta}{2}\left[\tanh\left(a\left(\frac{x_3}{L_{x_3}} - \frac{1}{2}\right)\right) - \frac{2x_3}{L_{x_3}} + 1\right], \tag{2.10}$$

where $\Delta\theta$ is the imposed temperature jump across the interface.

Droplet populations are initialized only in the cloudy half of the domain. For monodisperse runs, droplets have a uniform initial radius $R_0 = 15$ μm. For polydisperse runs, the initial radii are sampled from a log-normal distribution spanning 0.6–30 μm. The total number of droplets is of order 10^7, corresponding to typical cloud droplet number concentrations.

Quantity	Symbol	Value	Unit
Simulation domain size	$L_{x_1} \cdot L_{x_2} \cdot L_{x_3}$	$0.512 \cdot 0.512 \cdot 1.024$	m^3
Simulation domain discretization	$N_1 \cdot N_2 \cdot N_3$	$512 \cdot 512 \cdot 1024$	
Simulation grid step	Δx	0.001	m
Initial and final Kolmogorov time	τ_η	$3.75 \cdot 10^{-2}$, 0.27	s
Initial and final Kolmogorov scale in the cloud	η	0.6, 2.2	mm
Root mean square of velocity fluctuation in cloud region	u_{rms}	0.1125	m/s
Initial particle response time at $R_0 = 15\,\mu$m	τ_p	$3.6 \cdot 10^{-3}$	s
Initial large eddy turn over time	τ_0	0.42	s
Initial droplet radius for monodisperse distribution	R_{in}	15	μm
Minimum droplet radius for polydisperse distribution	$R_{\text{in-p,min}}$	0.6	μm
Maximum droplet radius for polydisperse distribution	$R_{\text{in-p,max}}$	30	μm
Total number of initial droplets (monodisperse population)	$N_{\text{tot-m}}$	$8 \cdot 10^6$	
Total number of initial droplets (polydisperse population)	$N_{\text{tot-p}}$	10^7	
Simulation time step	Δt	$3.8 \cdot 10^{-4}$	s
Initial integral scale	l	0.048	m
Initial Taylor micro-scale Reynolds no.	Re_λ	42	
Reynolds number based on domain dimension	Re_L	5000	

Table 2.1: List of parameters for cloud–clear air DNS hosting mono- and poly-disperse droplet populations (adapted from [7]).

2.3 Methodology of Post-Processing

After the Direct Numerical Simulation (DNS), the data were post-processed to extract the relevant physical quantities and spectral information. This step is essential for interpreting the flow dynamics and identifying the dominant physical mechanisms that govern the evolution of the system.

The first step consisted of transforming the data from spectral space to physical space whenever needed, in order to compute fields as functions of the physical coordinates:

$$\hat{f}(\mathbf{k}, t) \;\Rightarrow\; f(\mathbf{x}, t),$$

where $\hat{f}(\mathbf{k}, t)$ represents the spectral field and $f(\mathbf{x}, t)$ its real-space counterpart. This operation was carried out using a three-dimensional inverse Fast Fourier Transform (iFFT) applied to the DNS data.

Because of the inherently anisotropic nature of the problem and the vertical direction playing a central role, an *horizontal averaging operator* was introduced to filter out small-scale fluctuations in the horizontal planes, leaving only the vertical and temporal dependence of the field:

$$\langle \phi \rangle_{xy}(z, t) \coloneqq \frac{1}{L_x L_y} \int_0^{L_x} \int_0^{L_y} \phi(x, y, z, t)\, dx\, dy \simeq \frac{1}{N_x N_y} \sum_{i=1}^{N_x} \sum_{j=1}^{N_y} \phi(x_i, y_j, z, t), \quad (2.11)$$

where $\phi(x, y, z, t)$ is a generic field of interest (e.g., velocity component or temperature), L_x and L_y are the horizontal domain sizes, and N_x, N_y the number of grid points in the two horizontal directions. The continuous form is shown on the left-hand side

Table 2.2: List of simulations and stratification/energy settings.

Simulation	$\Delta\theta_0$ [K]	$E_{\mathrm{cloud}}/E_{\mathrm{clear}}$	**Level** $[\times 10^3\, G_0]$	$\mathcal{N}_{\mathrm{ic}}^2$ [s^{-2}]	$\mathrm{Fr}_{\mathrm{ic}}^2$	Re_b	**Eddy turnovers**
MD U7	-2	6.7	-8.26	-1.8733	0.93	254.5	35.06
MD S7	2	6.7	8.26	1.8733	0.93	254.5	35.06
MD UT1E16	-1	16	-4.13	-0.9366	3.95	1102	35.06
MD UT4E16	-4	16	-16.5	-3.7466	0.988	275.5	35.06
MD ST1E16	1	16	4.13	0.9366	3.95	1102	35.06
MD ST4E16	4	16	16.5	3.7466	0.988	275.5	35.06
PD UT1E16	-1	16	-4.13	-0.9366	3.95	1102	35.06
PD UT4E16	-4	16	-16.5	-3.7466	0.988	275.5	35.06
PD ST1E16	1	16	4.13	0.9366	3.95	1102	35.06
PD ST4E16	4	16	16.5	3.7466	0.988	275.5	35.06

Notes and definitions. Following [31], define the (initial-condition) Brunt–Väisälä frequency $\mathcal{N}_{\mathrm{ic}} = \left(\alpha g\, \partial_z \theta_{\mathrm{ic}}\right)^{1/2}$, where $\partial_z \theta_{ic} = \max(\partial_z \theta(z))$. The Froude number and its square are $\mathrm{Fr}_{ic} = \dfrac{u_{\mathrm{rms}}}{\mathcal{N}_{\mathrm{ic}}\, l}$, $\mathrm{Fr}_{ic}^2 = \dfrac{u_{\mathrm{rms}}^2}{\mathcal{N}_{\mathrm{ic}}^2\, l^2}$. The buoyancy Reynolds number is $Re_b = \dfrac{\varepsilon}{\nu\, \mathcal{N}_{\mathrm{ic}}^2}$, where ε is the (initial) kinetic-energy dissipation rate, l the initial integral scale, and ν the kinematic viscosity. "Level" denotes the stratification class with respect to $G_0 = 0.0065\ K/m$(e.g. $2G_0$, $30G_0, \ldots$).

Table 2.3: Key physical parameters used in the numerical experiments.

Quantity	**Symbol**	**Value**	**Unit**
Latent heat of evaporation	$\mathcal{L}$	2.48×10^6	$\mathrm{J\,kg^{-1}}$
Heat capacity (air, const. p)	c_p	1005	$\mathrm{J\,kg^{-1}K^{-1}}$
Gravitational acceleration	g	9.81	$\mathrm{m\,s^{-2}}$
Molar mass of water	$\mathcal{M}_w$	18	$\mathrm{kg\,mol^{-1}}$
Gas constant (water vapour)	R_v	461.5	$\mathrm{J\,kg^{-1}K^{-1}}$
Molar mass of dry air	$\mathcal{M}_a$	29	$\mathrm{kg\,mol^{-1}}$
Gas constant (air)	R_a	286.7	$\mathrm{J\,kg^{-1}K^{-1}}$
Vapour diffusivity	κ_v	2.52×10^{-5}	$\mathrm{m^2\,s^{-1}}$
Thermal conductivity (air)	κ	2.5×10^{-2}	$\mathrm{W\,m^{-1}K^{-1}}$
Liquid water density	ρ_w	1000	$\mathrm{kg\,m^{-3}}$
Dry air density (1000 m)	ρ_0	1.11	$\mathrm{kg\,m^{-3}}$
Air kinematic viscosity	ν	1.5×10^{-5}	$\mathrm{m^2\,s^{-1}}$
Average temperature (domain)	T_0	281.16	K
Reference temperature	T_{ref}	273.15	K
Reference vapor density	$\rho_{vs}(T_{ref})$	4.8×10^{-3}	$\mathrm{kg\,m^{-3}}$
Atmospheric lapse rate	G_0	0.0065	$\mathrm{K\,m^{-1}}$
Droplet growth coefficient	K_s	8.6×10^{-11}	$\mathrm{m^2\,s^{-1}}$
Accumulation mode radius	r_d	0.01	μm
Kelvin coefficient	A	1.15×10^{-9}	m
Raoult solubility parameter	B	0.7	–
Initial relative humidity (cloud)	RH_1	1.02	–
Initial relative humidity (clear)	RH_2	0.70	–
Initial liquid water content	LWC_0	7.9×10^{-4}	$\mathrm{kg\,m^{-3}}$

of Eq. (2.11), while the right-hand side represents its discrete approximation used in practice.

This operator was applied systematically to obtain profiles such as horizontally averaged velocity components, temperature, and other scalar fields, yielding $\langle\phi\rangle_{xy}(z,t)$ as a function of height z and time t.

Statistical Quantities

In addition to the mean field, higher-order statistical moments were computed to characterize the fluctuations of the flow. The second moment, or *variance*, measures the intensity of fluctuations around the mean:

$$\mathrm{Var}[\phi](z,t) = \langle\Big(\phi - \langle\phi\rangle_{xy}\Big)^2\rangle_{xy}.$$

The third moment, or *skewness*, describes the asymmetry of the fluctuation distribution:

$$\mathrm{Skew}[\phi](z,t) = \frac{\langle\Big(\phi - \langle\phi\rangle_{xy}\Big)^3\rangle_{xy}}{\mathrm{Var}[\phi]^{3/2}},$$

where positive values indicate a predominance of upward deviations, while negative values correspond to downward-dominated events.

The fourth moment, or *kurtosis*, quantifies the intermittency and the occurrence of extreme events:

$$\mathrm{Kurt}[\phi](z,t) = \frac{\langle\Big(\phi - \langle\phi\rangle_{xy}\Big)^4\rangle_{xy}}{\mathrm{Var}[\phi]^2},$$

with values greater than 3 indicating heavy-tailed distributions compared to a Gaussian reference.

These moments were evaluated for both velocity and temperature fields, providing a complete statistical characterization of the turbulence, from average structure to extreme fluctuations.

Derived Quantities

Several physically relevant derived quantities were calculated to further analyze the flow. The *Turbulent Kinetic Energy* (TKE) was computed from the variance of the velocity components as

$$E_k(z,t) = \frac{1}{2}\sum_{i=1}^{3}\langle u_i'^2\rangle_{xy},$$

where u_i' are the velocity fluctuations and $\langle\cdot\rangle_{xy}$ denotes the horizontal averaging operator introduced in Eq. (2.11).

The *buoyancy frequency* (or Brunt–Väisälä frequency) $\mathcal{N}(z,t)$, which characterizes the stability of the stratification, was computed from the horizontally averaged potential temperature field as

$$\mathcal{N}^2(z,t) = \frac{g}{\langle\theta\rangle_{xy}(z,t)} \frac{\partial\langle\theta\rangle_{xy}(z,t)}{\partial z},$$

where θ is the potential temperature and g the gravitational acceleration. The vertical derivative was evaluated using centered finite differences on the discrete DNS data. Regions with larger values of $\mathcal{N}$ correspond to stronger stratification.

Once the buoyancy frequency was determined, the *Froude number* was computed locally as a function of height and time to quantify the relative importance of turbulence and stratification:

$$Fr(z,t) = \frac{1}{\mathcal{N}(z,t)\,\tau(z,t)}, \tag{2.12}$$

where $\tau(z,t)$ is a characteristic local turbulence timescale.

The turbulence time scale was estimated from the local root-mean-square velocity fluctuation and the vertical integral length scale as

$$\tau(z,t) = \frac{l(z,t)}{u_{\mathrm{rms}}(z,t)}, \qquad u_{\mathrm{rms}}(z,t) = \sqrt{\langle u'^2\rangle_{xy}(z,t)}. \tag{2.13}$$

The integral length scale $l(z,t)$ was obtained directly from the one-dimensional horizontal velocity spectrum at each height:

$$l(z,t) = \frac{\int_0^\infty k_h^{-1} E(k_h,z,t)\,dk_h}{\int_0^\infty E(k_h,z,t)\,dk_h} \tag{2.14}$$

where $E(k_h,z,t)$ is the energy spectrum as a function of horizontal wavenumber k_h. In this implementation, no additional prefactors (such as $3\pi/4$) were included, so $l(z,t)$ corresponds exactly to the direct integral of the spectrum weighted by $1/k_h$.

Substituting $\tau(z,t)$ into the definition of the Froude number, the final expression becomes

$$Fr(z,t) = \frac{u_{\mathrm{rms}}(z,t)}{\mathcal{N}(z,t)\,l(z,t)},$$

which explicitly shows the balance between turbulence intensity and the stabilizing effect of stratification.

In practice, $\mathcal{N}(z,t)$ was calculated directly from the horizontally averaged vertical profiles of temperature, while $u_{\mathrm{rms}}(z,t)$ and $l(z,t)$ were computed using the horizontal velocity spectra at each vertical position. This approach allowed tracking the vertical and temporal evolution of the Froude number, distinguishing regions where turbulence dominates from those where internal waves are more relevant.

Mixing-Layer Analysis

The first step in the analysis was to objectively identify the vertical region where turbulent mixing actively occurs. To do so, we used horizontally averaged scalar profiles of potential temperature, $\langle\theta\rangle_{xy}(z,t)$, and water vapor mixing ratio, $\langle q_v\rangle_{xy}(z,t)$. These profiles were normalized between their instantaneous minimum and maximum values to remove the effect of large-scale variations:

$$\Theta(z,t) = \frac{\langle\theta\rangle_{xy}(z,t) - \theta_{\min}(t)}{\theta_{\max}(t) - \theta_{\min}(t)}, \qquad Q_v(z,t) = \frac{\langle q_v\rangle_{xy}(z,t) - q_{v,\min}(t)}{q_{v,\max}(t) - q_{v,\min}(t)}.$$

The mixing layer boundaries, $z_1(t)$ and $z_2(t)$, were defined as the vertical locations where both normalized profiles cross the thresholds 0.25 and 0.75, respectively. This 25–75% criterion is widely used in stratified turbulence studies as it captures the dynamically active region while excluding the outer quiescent zones. The instantaneous mixing-layer thickness is then

$$\delta(t) = z_2(t) - z_1(t).$$

Once the region $\mathcal{M}(t) = [z_1(t), z_2(t)]$ is identified, any horizontally averaged field $Q(z,t)$ can be further integrated in the vertical to produce a layer-mean quantity:

$$\langle Q\rangle_{\mathcal{M}}(t) = \frac{1}{h(t)}\int_{z_1(t)}^{z_2(t)} Q(z,t)\,dz, \qquad Q^{\mathcal{M}}_{\max}(t) = \max_{z\in\mathcal{M}(t)} Q(z,t).$$

All quantities are averaged over the mixing region $\mathcal{M}(t)$ to track their temporal evolution:

$$\langle\mathcal{N}^2\rangle_{\mathcal{M}}(t), \quad \langle Fr\rangle_{\mathcal{M}}(t),$$

together with their maxima $Q^{\mathcal{M}}_{\max}(t)$. This consistent methodology ensures that both turbulence and stratification are characterized within the dynamically active portion of the flow.

Spectral Analysis

To identify the dominant spatial and temporal scales, a spectral analysis was carried out in both horizontal and vertical directions. The velocity fields were first transformed to Fourier space along the spatial coordinates, and energy spectra were computed as

$$E(\mathbf{k},t) = \frac{1}{2}\sum_{i=1}^{3} |\hat{u}_i(\mathbf{k},t)|^2,$$

where $\hat{u}_i$ is the Fourier transform of the i-th velocity component.

The isotropic energy spectrum was obtained by averaging $E(\mathbf{k},t)$ over spherical

shells of constant wavenumber magnitude,

$$\kappa = \sqrt{k_x^2 + k_y^2 + k_z^2}.$$

The continuous isotropic spectrum is defined as

$$E(\kappa, t) = \int_{S(k)} E(\mathbf{k}, t)\, dS,$$

where $S(\kappa)$ denotes the spherical shell of radius κ. In the discrete case, the (k_x, k_y, k_z) points were assigned to bins of width $\Delta\kappa$ according to their magnitude κ. The energy in each bin was computed as

$$E(k_b, t) = \frac{1}{N_b} \sum_{\mathbf{k} \in \mathcal{B}(k_b)} E(\mathbf{k}, t),$$

where $\mathcal{B}(k_b)$ is the set of Fourier modes whose magnitude falls within

$$k_b - \frac{\Delta k}{2} \leq |\mathbf{k}| < k_b + \frac{\Delta k}{2},$$

and N_b is the number of modes in the bin. This process yields a smooth estimate of the isotropic energy distribution.

Because of the horizontally periodic and vertically inhomogeneous domain, we also computed horizontal spectra at each height z. The horizontal wavenumber is defined as

$$k_h = \sqrt{k_x^2 + k_y^2}.$$

The binning in this case follows a similar approach: the (k_x, k_y) points at each fixed z are grouped into concentric annular bins of width Δk_h, and the energy is averaged within each annulus:

$$E(k_{h,b}, z, t) = \frac{1}{N_{h,b}} \sum_{(k_x,k_y) \in \mathcal{B}_h(k_{h,b})} \frac{1}{2} \sum_{i=1}^{3} |\hat{u}_i(k_x, k_y, z, t)|^2,$$

where $\mathcal{B}_h(k_{h,b})$ denotes the set of modes in the annulus centered at $k_{h,b}$ and $N_{h,b}$ is the number of modes in that bin. This procedure yields $E(k_h, z, t)$, which was then used to compute quantities such as the vertical profile of the integral length scale $l(k_h, z, t)$ and the large eddy turnover time $\tau(k_h, z, t)$.

For the temporal analysis, time series of selected Fourier modes were extracted at fixed (k_x, k_y, k_z) and a temporal Fourier transform was applied to compute frequency spectra. To reduce spectral leakage, a Hamming window was applied to each time

series prior to the FFT:

$$u_i(k,\omega) = \mathrm{FFT}\Big[w(t)\, u_i(k,t)\Big],$$

where $w(t)$ is the window function. The resulting $|u_i(k,\omega)|^2$ fields were then used to see how energy was distributed across wavenumbers and frequencies.

Furthermore, to investigate the temporal dynamics of both turbulence and internal gravity waves, velocity signals were extracted at fixed spatial locations (x_0, y_0, z_0) over the entire simulation duration. For each selected point, the three velocity components $u_i(t)$ were stored, where $i = 1, 2, 3$.

To reduce small-scale noise, a local spatial average was performed over a square neighborhood centered at the point of interest (x_0, y_0, z_0) at fixed vertical level $z = z_0$. This neighborhood is mathematically defined as

$$\mathcal{B}(x_0, y_0) = \Big\{(x,y) \in \Omega_h \;\Big|\; \|(x,y) - (x_0,y_0)\|_\infty \le r_N\Big\},$$

where Ω_h is the horizontal domain and

$$\|(x,y) - (x_0,y_0)\|_\infty = \max\Big(|x - x_0|,\, |y - y_0|\Big)$$

is the infinity norm, with $r_N = N_{\text{around}}\Delta x$ representing the physical half-width of the neighborhood and Δx the grid spacing.

On the discrete grid, the corresponding set of points is

$$\mathcal{B}^\Delta(x_0, y_0) = \Big\{(x_i,y_j) \in \Omega_h^\Delta \;\Big|\; \|(x_i,y_j) - (x_0,y_0)\|_\infty \le r_N\Big\},$$

where $(x_i, y_j) = (i\Delta x, j\Delta x)$ are the grid points at fixed $z = z_0$.

For the present analysis, $N_{around} = 10$, corresponding to a square of side

$$L_{loc} = (2\, N_{\text{around}} + 1)\, \Delta x,$$

including a total of $|\mathcal{B}| = (2\, N_{\text{around}} + 1)^2 = 21^2 = 441$ points.

The locally averaged velocity signal is then computed as

$$\langle u_i(t)\rangle = \frac{1}{|\mathcal{B}|} \sum_{(x,y)\in\mathcal{B}^\Delta(x_0,y_0)} u_i(x, y, z_0, t),$$

where $|\mathcal{B}|$ is the total number of points in the neighborhood. This averaging acts as a low-pass spatial filter.

The choice of the parameter N_{around} represents a compromise between noise reduction and signal preservation: larger neighborhoods provide stronger filtering of high-frequency turbulent noise, but at the cost of smoothing out the physical signal of interest, such as coherent wave motions. Conversely, very small neighborhoods retain

localized features but are more contaminated by turbulent fluctuations.

In this study, $N_{around} = 10$ was adopted as a balanced compromise, resulting in a 21×21 horizontal region. This corresponds to a total of 441 points, which is approximately

$$\frac{441}{512^2} \approx 1.7 \times 10^{-3} \quad \text{(or 0.17\%)}$$

of the entire horizontal domain (512×512). This fraction is sufficiently small to ensure that the averaging remains local while still providing a meaningful reduction of small-scale turbulent noise.

The velocity signals were then filtered to retain only the time interval of interest $[t_{min}, t_{max}]$. A Hamming window $w(t)$ was applied to the temporal signal before performing the discrete Fourier transform, in order to reduce spectral leakage. The temporal Fourier transform of each velocity component was defined as

$$\hat{u}_i(\omega) = \mathrm{FFT}\Big[\, w(t)\, u_i(t)\Big],$$

where ω is the angular frequency.

The local energy were obtained by summing over the three velocity components,

$$E_{loc}(t) = \frac{1}{2} \sum_{i=1}^{3} |u_i(t)|^2.$$

Acceleration spectra. In addition to velocity, the temporal evolution of the acceleration was analyzed. The acceleration at each point was computed numerically by applying a centered finite-difference scheme to the velocity time series:

$$a_i(t_n) = \frac{u_i(t_{n+1}) - u_i(t_{n-1})}{2\,\Delta t},$$

where Δt is the temporal sampling interval of the stored fields. This scheme is second-order accurate and minimizes numerical noise while providing a reliable estimate of the local time derivative.

The acceleration signals were processed using the same FFT procedure applied to velocity, yielding

$$\hat{a}_i(\omega) = \mathrm{FFT}\Big[\, w(t)\, a_i(t)\Big].$$

Spectrograms. To further highlight the temporal intermittency of turbulence and the presence of coherent wave-like motions, a time–frequency analysis was performed by computing spectrograms of the acceleration signals. A short-time Fourier transform

was applied by sliding a window of fixed width along the time series:

$$\hat{a}_i(\omega, t) = \mathrm{FFT}\Big[\, w(t')\, a_i(\mathbf{x}_0, t + t')\Big],$$

where t' is the local time within each window. The magnitude, $|\hat{a}_i(\omega, t)|^2$, was then plotted as a function of both frequency and global time. This representation provides a clear visualization of transient bursts of turbulence, wave packets, and energy transfers between low-frequency internal waves and high-frequency turbulent fluctuations.

ω–k maps. To investigate the coupling between spatial and temporal scales, we further analysed selected Fourier modes in space by constructing ω–κ maps. Since the DNS output provides the velocity field directly in spectral space, $\hat{u}_i(k_x, k_y, k_z, t)$, we fixed a few representative horizontal Fourier pairs $(k_x, k_y) \in \{(1,1), (2,2), (3,3)\}$ and extracted the corresponding vertical modes $\hat{u}_i(k_z, t)$ over the entire simulation time. For each selected pair, the temporal Fourier transform was applied independently at each vertical wavenumber k_z:

$$\hat{u}_i(k_x, k_y, k_z, \omega) \;=\; \mathrm{FFT}\Big[\, w(t)\, \Big(\hat{u}_i(k_x, k_y, k_z, t) - \langle \hat{u}_i \rangle_t\Big)\Big],$$

where $w(t)$ is a Hamming window and the temporal mean has been removed to avoid a spurious peak at $\omega = 0$. The resulting quantity

$$P_i(k_z, \omega) = |\hat{u}_i(k_x, k_y, k_z, \omega)|^2$$

represents the joint distribution of energy across vertical wavenumbers and frequencies. These ω–k_z spectra are particularly informative in stratified flows, as they allow us to distinguish energy that follows the internal–wave dispersion relation from broadband turbulent motions, and to assess how wave activity weakens or intensifies as stratification evolves in time.

The procedure was implemented in MATLAB and automated to handle large datasets. Velocity files were read for the three components at each spatial location and averaged when necessary. Acceleration was computed directly from the velocity data, and the resulting spectra and spectrograms were stored in structured folders for post-processing. Hamming windows were consistently applied both for standard spectra and for spectrograms, with partial overlap between successive windows to ensure smooth time–frequency transitions. All spectra were normalized and plotted in both linear and logarithmic scales to capture the behavior of both energetic large-scale motions and dissipative high-frequency fluctuations.

Chapter 3

Results

In this chapter, we present the main results obtained from the processed simulation data. We begin by showing the vertical profiles of energy and their evolution over time. Next, we introduce the two scalar fields: temperature and vapor density. From these scalars, we compute derived quantities that highlight the effects of stratification, such as characteristic frequency numbers and characteristic turbulence numbers. Finally, we conclude with a spectral analysis, emphasizing the presence of wave-like solutions.

3.1 TKE profile evolution

The first quantity computed is the turbulent kinetic energy (TKE), previously defined through the horizontal mean. In this section, we plot E_k as a function of the vertical coordinate z, at each time instance. Figure 3.1 shows these profiles, where the panels on the right correspond to unstable cases with a mono-disperse droplet population, while those on the left represent the stable counterparts. The plots are presented in logarithmic scale to better highlight the different magnitudes. At the initial time steps, a sharp transition is clearly visible between the cloudy, more turbulent region and the clear-air region. The ratio of turbulent kinetic energy between these two areas, computed as in the previous chapter, is approximately $E_k^{\text{cloud}}/E_k^{\text{clear}} \sim 6.7$ for the MDS7 and MDU7 cases, while it is around ~ 16 for the other cases. The difference between stable and unstable conditions becomes evident after approximately $t/\tau_0 \sim 5$. In the stable simulations, a local *pit* of energy develops at the interface (mixing layer), particularly in cases with larger initial temperature differences ΔT. Conversely, in the unstable cases we observe a continuous growth of energy within the mixing region, in agreement with previous numerical studies; in particular, the present results are qualitatively consistent with those reported by Golshan et al. [7] and Fossà et al. [6]. A novel and remarkable feature is observed in the stable cases: after the initial formation of the energy pit, within just a few characteristic time scales, the energy in the mixing region begins to exhibit a decaying *wavy* behavior, alternating between periods of

increase and decrease over time. This phenomenon is clearly visible in Figure 3.2, particularly for the $\Delta T = 4$ case and, to a lesser extent, for the $\Delta T = 2$ case. The yellow curves in Figure 3.1, which represent the final simulated time, further highlight this behavior. In particular, for the MDS7 and MDST4E16 simulations, corresponding to initial temperature jumps of $\Delta T = 2$ and $\Delta T = 4$ respectively, the vertical energy profiles develop a distinct concave shape near the center of the domain. This indicates the emergence of a local maximum of energy both in space and in time. By contrast, in the MDST1E16 case, where the initial stratification is weaker, the energy profile decays smoothly and monotonically, without the formation of pronounced oscillations.

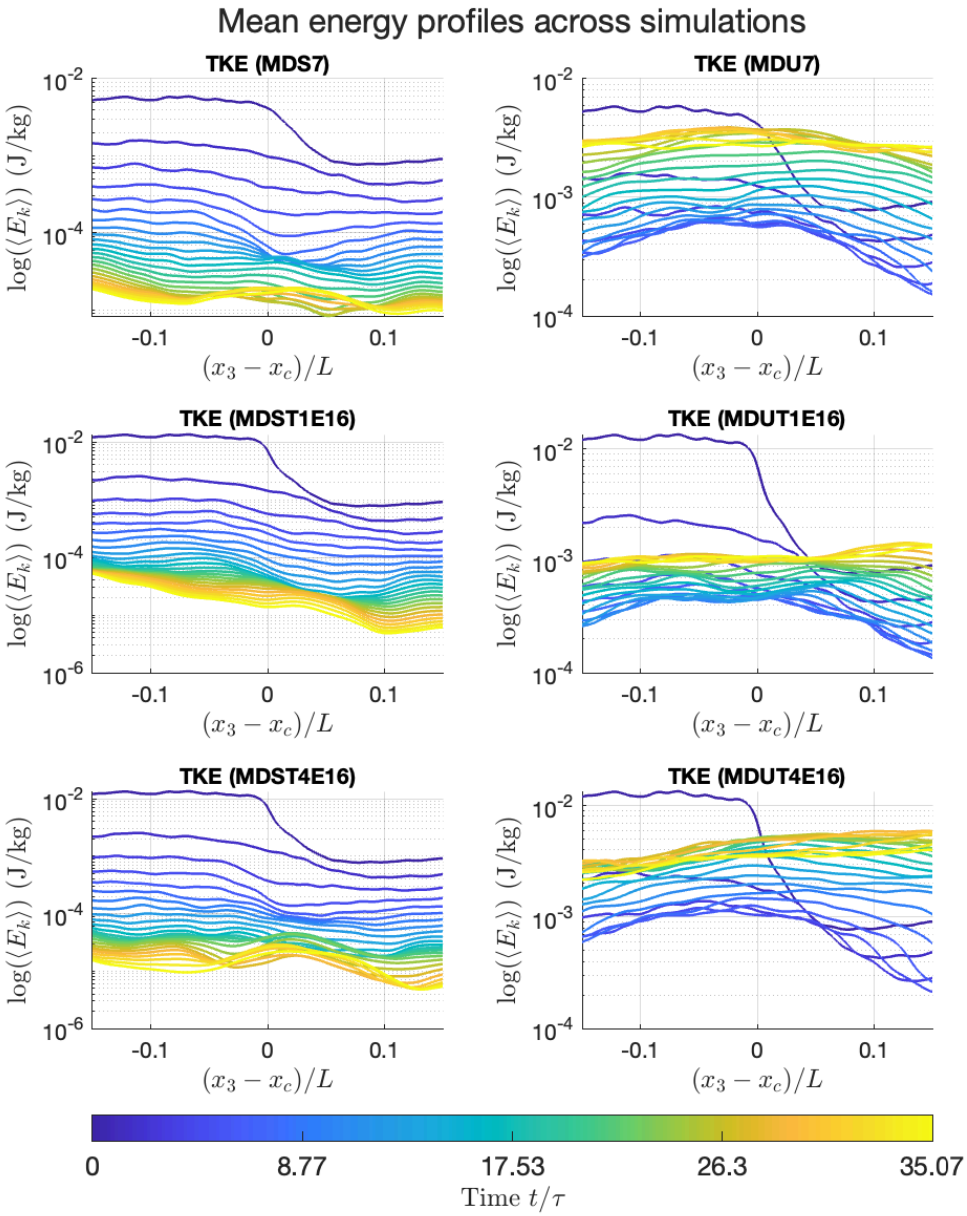

Figure 3.1: Mean Turbulent kinetic energy vertical profiles evolution in time (from 0 (blue) to 35 (yellow) t/τ), across different mono-disperse simulations-on the left the stable cases and unstable on the right.

On the other hand, in the unstable cases, after an initial phase of quasi-constant growth, the turbulent kinetic energy gradually stabilizes. Towards the end of the simulation, the energy profiles become smoother functions of z, and the initial energy contrast between the cloudy and clear-air regions completely disappears. This behavior is physically consistent: due to turbulent mixing, scalar quantities are progressively homogenized. As a result, the temperature field becomes more uniform, its vertical gradient decreases, and the buoyancy effects are consequently reduced. Furthermore, we estimated the growth factor λ for the unstable cases. For both MDUT4E16 and MDU7, despite the doubled initial temperature difference, the value is approximately $\lambda \simeq 0.11$. In contrast, for the MDUT1E16 case we obtained $\lambda \simeq 0.055$, roughly half the value of the other two cases. This result is consistent with the fact that MDUT1E16 is the least stratified configuration. From Figure 3.2, we can also estimate the duration of the growth phase. The MDU7 case exhibits the longest growth interval, spanning from approximately $t/\tau_0 \sim 6$ to $t/\tau_0 \sim 25$. For MDUT4E16, the growth occurs earlier but ends sooner, roughly between $t/\tau_0 \sim 5$ and $t/\tau_0 \sim 18$. Finally, for MDUT1E16, the interval is intermediate, extending from about $t/\tau_0 \sim 9$ to $t/\tau_0 \sim 23$.

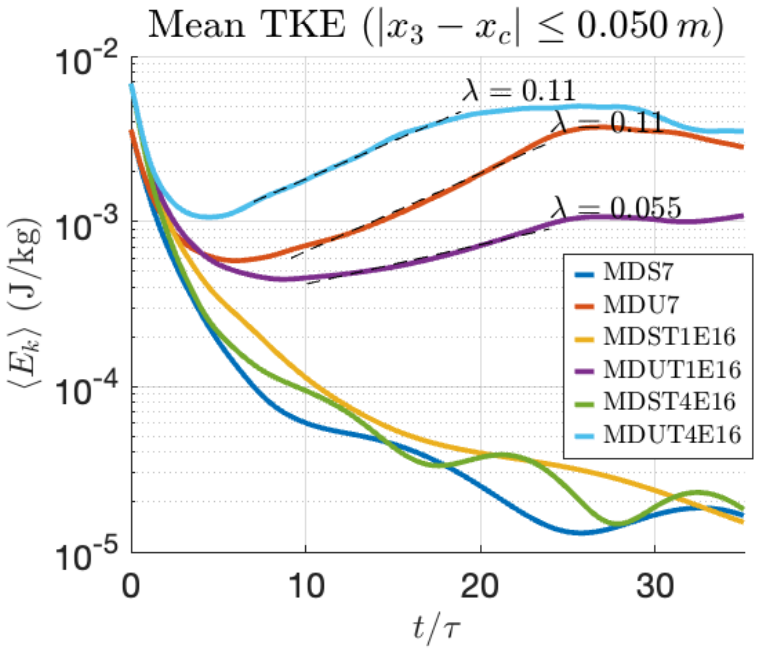

Figure 3.2: Time evolution of the turbulent kinetic energy (TKE) for the monodisperse cases, vertically averaged over the central region of the domain ($[-0.05, 0.05]$ m). For the unstable cases, the estimated growth rate λ is indicated. During the interval $t/\tau_0 \approx 10$–20, the energy exhibits an approximately exponential behaviour, following $E_k \sim e^{\lambda t}$.

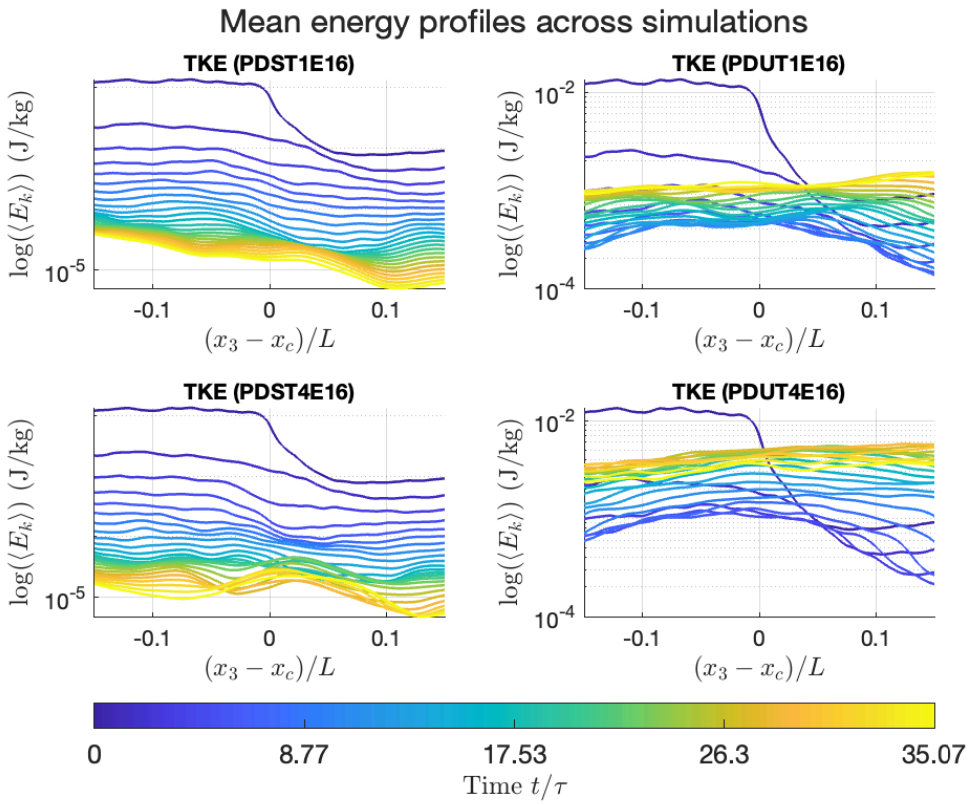

Figure 3.3: Mean Turbulent kinetic energy vertical profiles evolution in time (from 0 (blue) to 35 (yellow) t/τ), across different poly-disperse simulations-on the left the stable cases and unstable on the right.

These observations indicate that stratification influences not only the magnitude of the growth factor, but also the onset of the growth phase: the more strongly stratified cases tend to exhibit growth earlier. Conversely, the total duration of the growth appears to be primarily controlled by the intensity of mixing, and thus by the initial energy ratio between the cloudy and clear-air regions. In Figure 3.3 we present the time evolution of vertical TKE profiles for the poly-disperse cases. Qualitatively, their behavior closely resembles that of the mono-disperse simulations. In particular, we observe the same wavy pattern in the stable cases and the same growth factor in the unstable ones. To better quantify the effect of droplet population diversity, we computed the difference between the two sets of simulations, highlighting how the distribution of droplet sizes impacts the energy field. As discussed in Chapter 1, droplets influence the governing equations (1.3) solely through the phase transition term, which appears in both the temperature equation (1.16) and the vapor equation (1.17). Figure 3.4 shows that these differences remain negligible up to approximately $t/\tau_0 \sim 20$, after which they grow progressively. For the stable cases, the differences are mostly concentrated near the edges of the domain, eventually reaching values of the order of 10^{-5}, which is comparable to the decayed E_k at those later times. At the center of the domain, the difference initially shows a slight increase during the first stages, but it

becomes completely negligible as the system evolves. When comparing different levels of stratification, we observe that the ST1E16 cases display higher differences than the ST4E16 cases, with the former also retaining a noticeable growth of differences in the central region. In contrast, the unstable cases exhibit a much more chaotic behavior, especially toward the final stages (yellow curves). Here, the differences reach values that are two to three orders of magnitude higher than those observed in the stable cases. Since all simulations start from similar initial conditions and initially decay or decrease in energy, the differences between mono-disperse and poly-disperse runs emerge from negligible values at early times and become significant only in the final stages. This clearly shows that the impact of the droplet size distribution on the energy dynamics becomes evident primarily as the system approaches the later phases of its evolution.

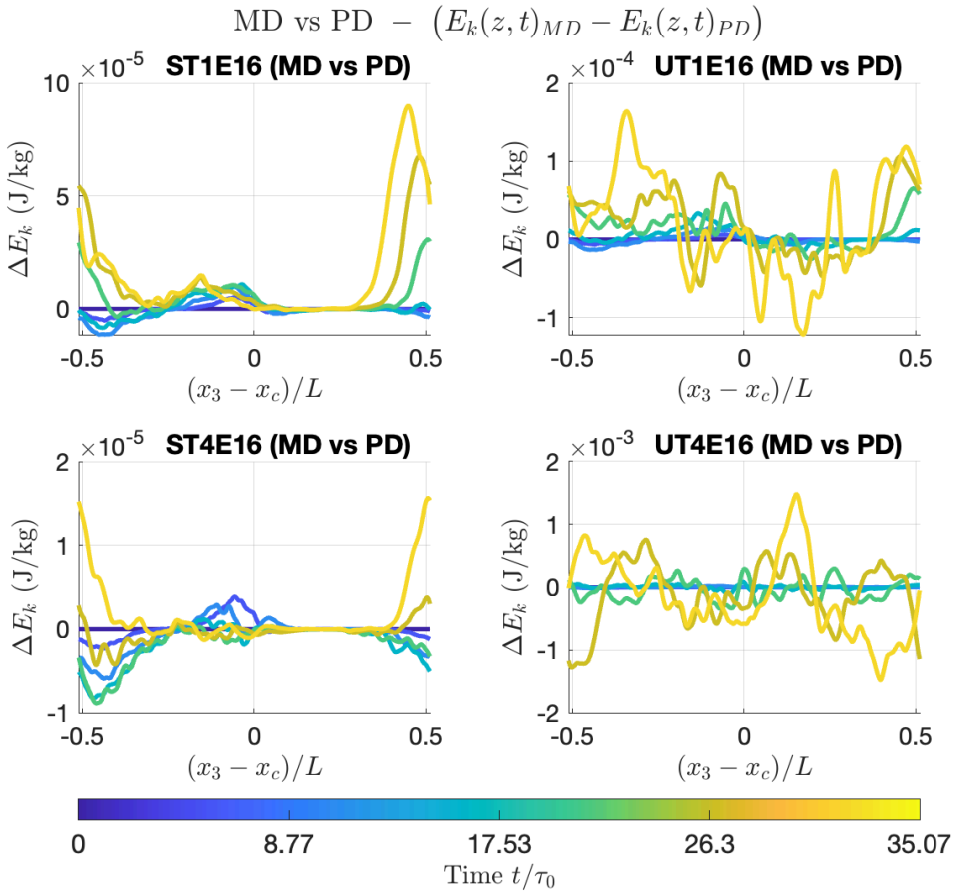

Figure 3.4: Vertical profiles of the difference in turbulent kinetic energy between the Mono-disperse (MD) and Poly-disperse (PD) cases, computed as $E_k(z,t)_{MD} - E_k(z,t)_{PD}$. Each panel corresponds to a specific simulation pair, while the colour gradient represents the temporal evolution normalized by the characteristic time scale τ_0. This visualization highlights the regions and time intervals where the two configurations diverge the most, providing insight into the effect of droplet population dynamics on turbulent mixing and energy distribution.

3.2 Temperature and vapour content statistics

Here, we present selected statistical moments, defined previously, analogously to the horizontal average. Figures (3.5–3.8) display the vertical profiles of temperature statistics, namely mean, variance, skewness, and kurtosis, in this order. Similarly, Figures (3.9–3.12) report the corresponding statistics for vapor density, following the same sequence as for temperature.

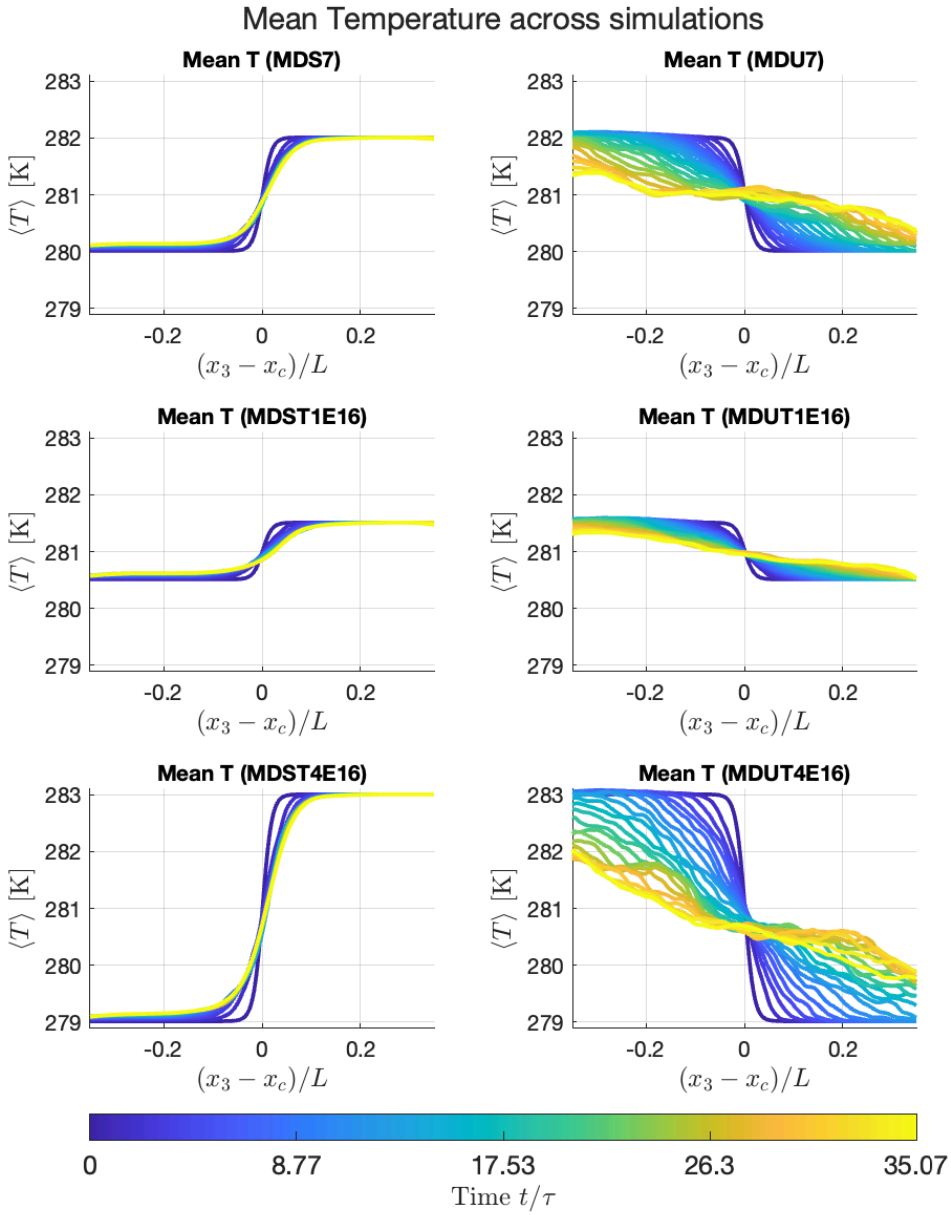

Figure 3.5: Temporal evolution of the vertical profiles of the mean temperature $\langle T \rangle$ for different mono-disperse simulations. The colors represent the normalized time t/τ_0. We have the stable cases on the left and unstable ones on the right.

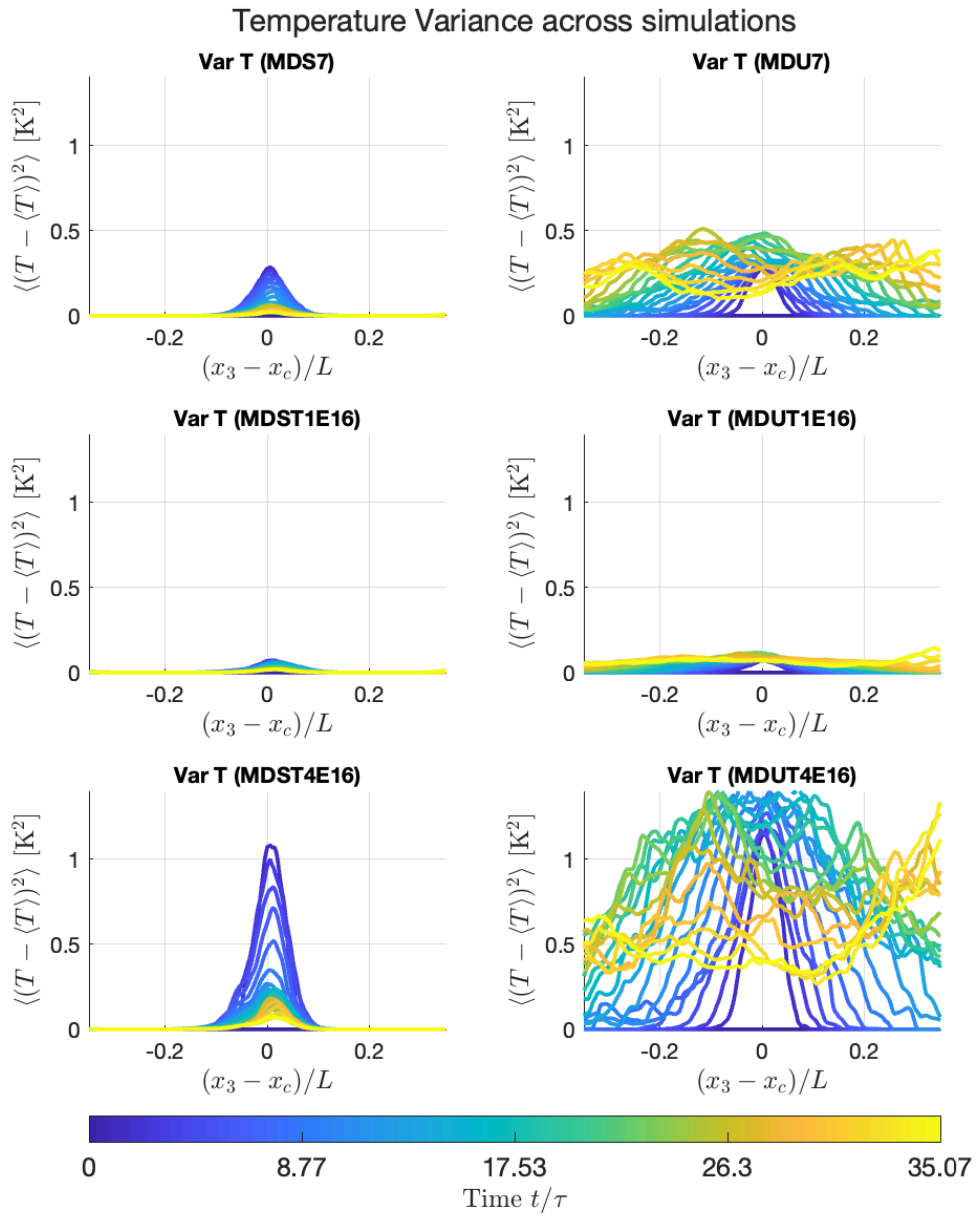

Figure 3.6: Temporal evolution of the vertical profiles of the variance of T , Var$[T]$ for different mono-disperse simulations. The colors represent the normalized time t/τ_0. We have the stable cases on the left and unstable ones on the right.

Temperature From Fig. 3.5, we observe how the mean temperature profiles $\langle T \rangle(z)$ evolve in time depending on the initial configuration. In the stable cases—characterized by higher temperatures in the clear-air region—the diffusive effects only slightly weaken and smooth the initial gradient, leaving its overall structure nearly unchanged. In contrast, in the unstable cases the impact of turbulent mixing is much more pronounced: the final profiles lose their initial shape and exhibit irregular fluctuations, yet on average display an approximately linear x_3-dependence.

As expected, the variance is strongly linked to the magnitude of the vertical temperature gradient. In Fig. 3.6, the variance reaches its highest values in the $\Delta T = 4$ cases,

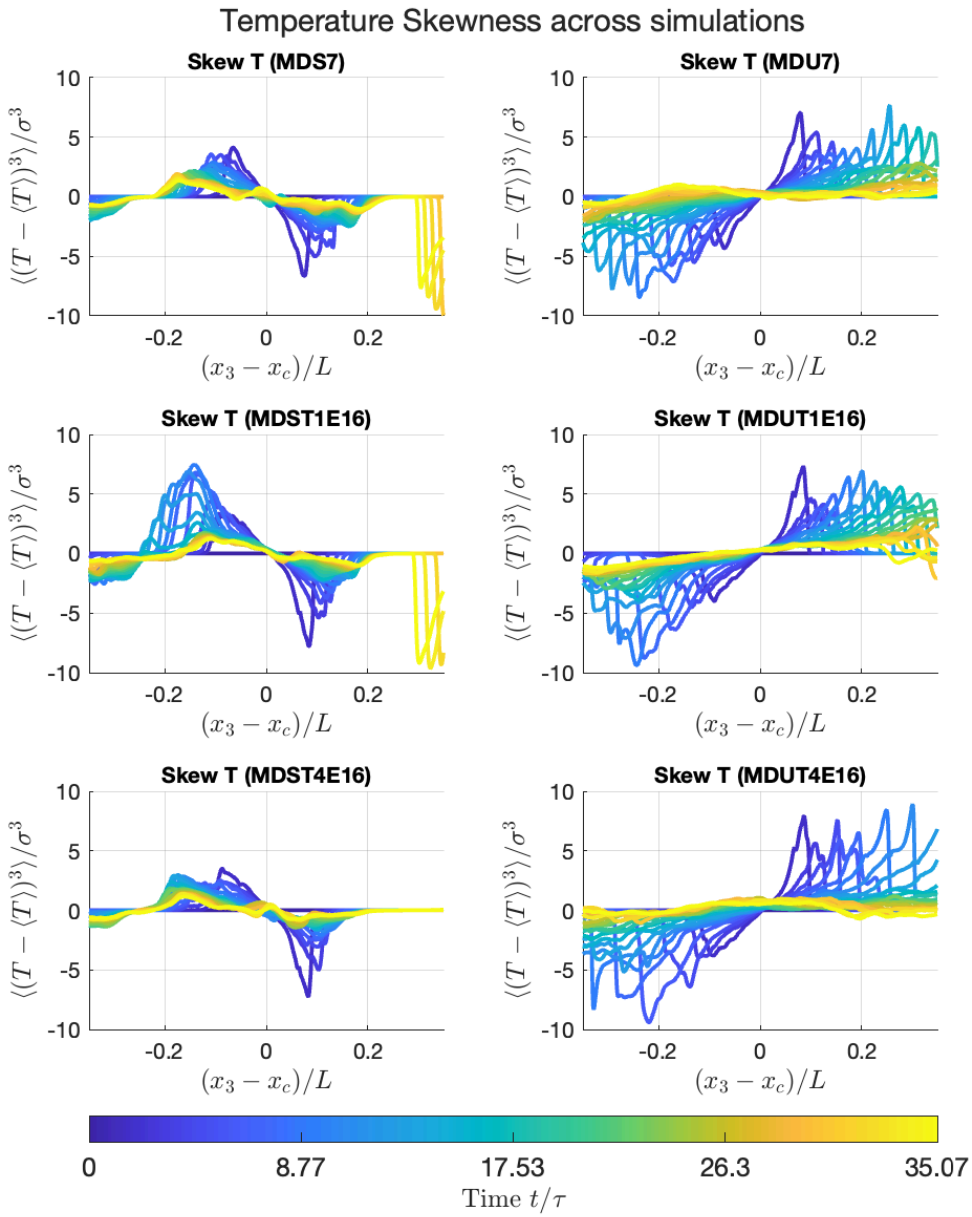

Figure 3.7: Temporal evolution of the vertical profiles of the skewness of T Skew$[T]$ for different simulations. The colors represent the normalized time t/τ_0. We have the stable cases on the left and unstable ones on the right.

whereas it remains much weaker in the $\Delta T = 1$ configurations. A clear distinction emerges between stable and unstable regimes. In the stable cases, the variance initially follows a Gaussian-like profile, with a well-defined peak at the interface ($x_3 = x_c$). As time progresses, this peak remains centered but decreases significantly in amplitude, indicating a gradual reduction of fluctuations around the interface. In contrast, the unstable cases depart from this behavior: after an initial Gaussian distribution, the variance grows in magnitude and evolves toward a broader, flatter, and more irregular distribution. At later times, the central peak weakens and the highest variance levels are displaced toward the clear-air region, consistent with the enhanced mixing and

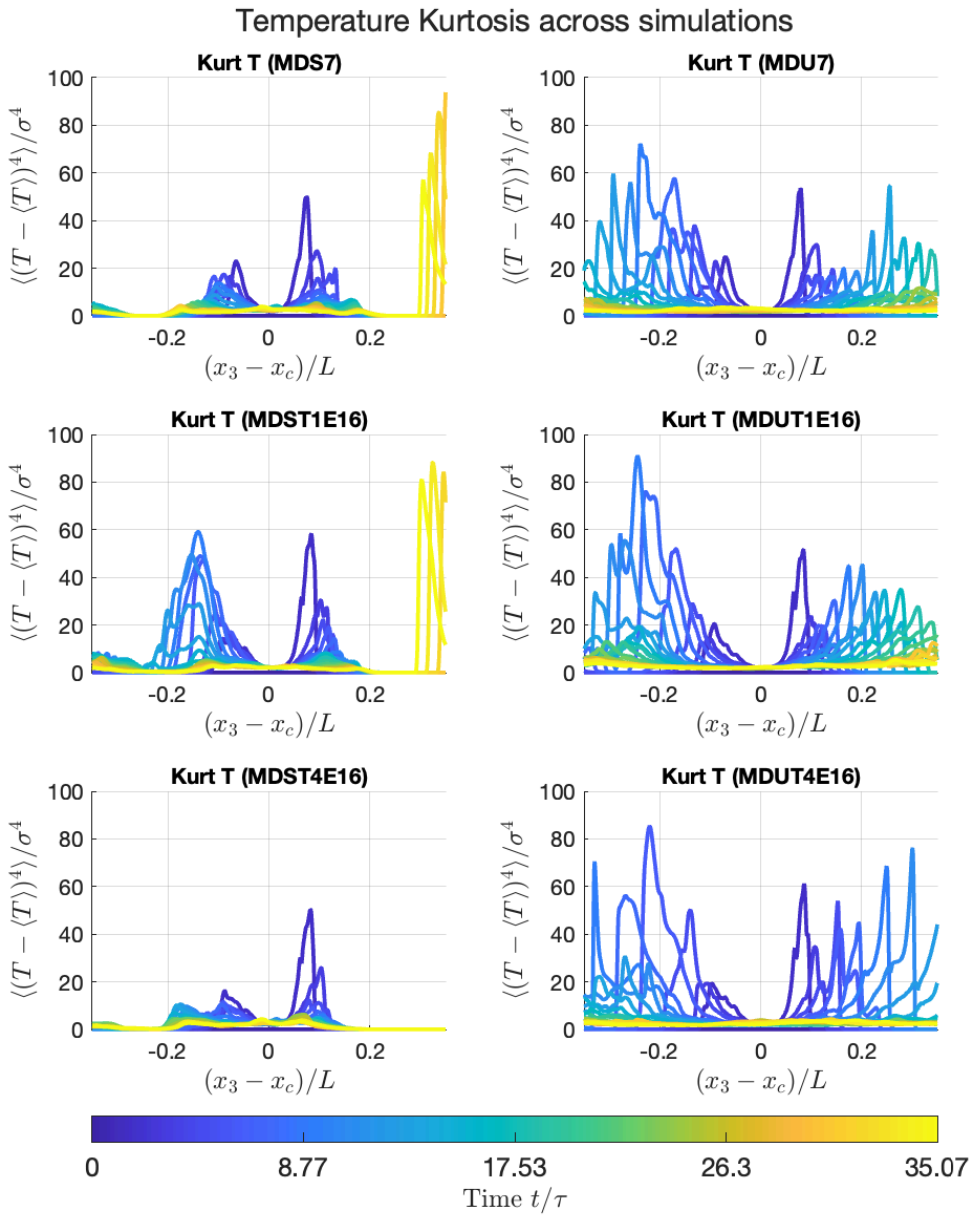

Figure 3.8: Temporal evolution of the vertical profiles of the skewness of T Kurt$[T]$ for different simulations. The colors represent the normalized time t/τ_0. We have the stable cases on the left and unstable ones on the right.

entrainment typical of unstable stratification. The skewness profiles highlight the asymmetry of temperature fluctuations within the cloud and the clear air. In the stable configurations (left panels), skewness is positive inside the cloud, indicating the prevalence of hot plumes, while it is negative in the clear air, where cold descending plumes dominate. In the unstable cases (right panels), the sign reverses: skewness becomes negative in the cloud and positive in the clear air, consistently reflecting the inverted temperature gradient. In all simulations, skewness values decrease in magnitude over time, tending towards more symmetric distributions as mixing progresses. These trends are fully consistent with the mean temperature profiles shown earlier. In fig. 3.8

we report the kurtosis of the temperature fluctuations. On the left, stable cases are shown, while unstable ones are on the right. In the stable configurations, kurtosis reaches the highest values when ΔT is smaller, which indicates stronger intermittency dominated by turbulent mixing. In all simulations, kurtosis tends to zero exactly at the center of the domain ($x_3 \simeq x_c$). For larger ΔT, stable cases display higher kurtosis values in the clear-air region, reflecting stronger tails in the distribution away from the cloud. In contrast, unstable cases show kurtosis increasing near the center, with peaks that progressively expand outward towards the domain edges. Eventually, in all simulations, kurtosis decreases significantly and approaches low values, suggesting that the temperature fluctuations evolve towards a nearly Gaussian distribution.

Vapor density Similarly to the temperature field, the vapor density statistics exhibit distinct behaviors depending on the degree of stratification. Figure 3.9 shows the vertical profiles of the horizontally averaged normalized vapor density, $\langle\tilde{\rho}_v\rangle(z)$, $\tilde{\rho}_v \coloneqq \frac{\rho_v}{\rho_{vs}(T_{\mathrm{ref}})}$, where $\rho_{vs}(T_{\mathrm{ref}})$ is the saturated vapor density at the reference temperature. The evolution of these profiles reveals a clear distinction between stably and unstably stratified configurations. As for the temperature field, in the stable cases most of the vertical gradient is confined within a narrow layer around the interface, whereas in the unstable ones enhanced mixing driven by the reversed stratification progressively erodes this sharp transition, leading to a growth of turbulent kinetic energy toward the end of the simulation.

Figure 3.10 reports the variance of vapor density fluctuations, which, consistently with the temperature variance, is closely linked to the mean gradient. However, the situation here is reversed: the case with $\Delta T = 1$ K displays a stronger vapor density gradient than the $\Delta T = 4$ K case. This behavior is physically consistent, since in stably stratified conditions the vapor and temperature gradients are of opposite sign, and variations in vapor density at constant total water content primarily reflect temperature-induced changes in saturation.

Furthermore, figure 3.11 shows the temporal evolution of the vertical profiles of the skewness of the normalized vapor density fluctuations, $\langle(\tilde{\rho}_v - \langle\tilde{\rho}_v\rangle)^3\rangle/\sigma^3$, for all simulated cases (stable on the left, unstable on the right). As in previous figures, colors indicate time progression from early (blue) to late (yellow) stages of the simulation. In the stably stratified configurations, the vapor skewness exhibits a pronounced negative peak around the interface on the cloudy side at early times, indicating that fluctuations are dominated by small, dry intrusions penetrating into the moist region. A corresponding positive peak appears on the opposite side, resulting in an antisymmetric structure that reflects turbulent exchanges across the interface. As time evolves, the magnitude of the skewness gradually decreases and the profiles tend to approach zero, signifying a progressive homogenization of the vapor field as mixing and diffusion weaken the asymmetry between moist and dry fluctuations.

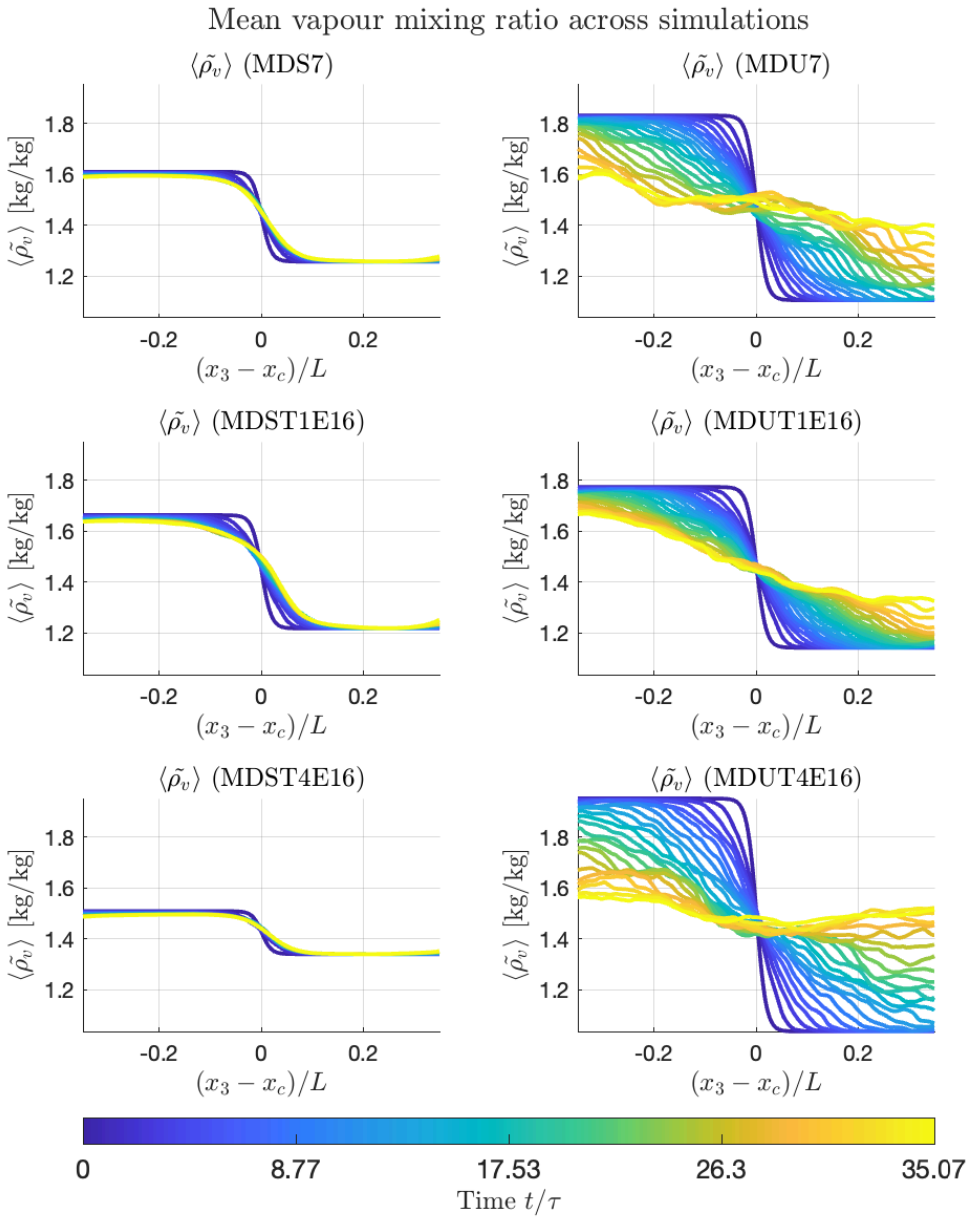

Figure 3.9: Temporal evolution of the vertical profiles of the mean normalized vapor density $\langle\tilde{\rho}_v\rangle = \langle\rho_v/\rho_{vs}(T_{ref})\rangle$ for different mono-disperse simulations. The colors represent the normalized time t/τ_0. We have the stable cases on the left and unstable ones on the right.

This decay is consistent with the attenuation of the mean gradients and with the reduction of buoyancy-driven intermittency as the system relaxes toward a quasi-stationary, weakly stratified state. In contrast, the unstable configurations display a strong positive skewness developing near the interface, associated with the upward transport of moist, buoyant parcels into the overlying dry region. The evolution of Skew$(\tilde{\rho}_v)$ in these cases closely mirrors that of temperature (see Figure 3.7), showing similar peaks that progressively move outward from the interface as turbulent mixing expands. These peaks gradually weaken toward the end of the simulation, reflecting the decay of convective activity and the transition toward a more homogeneous state.

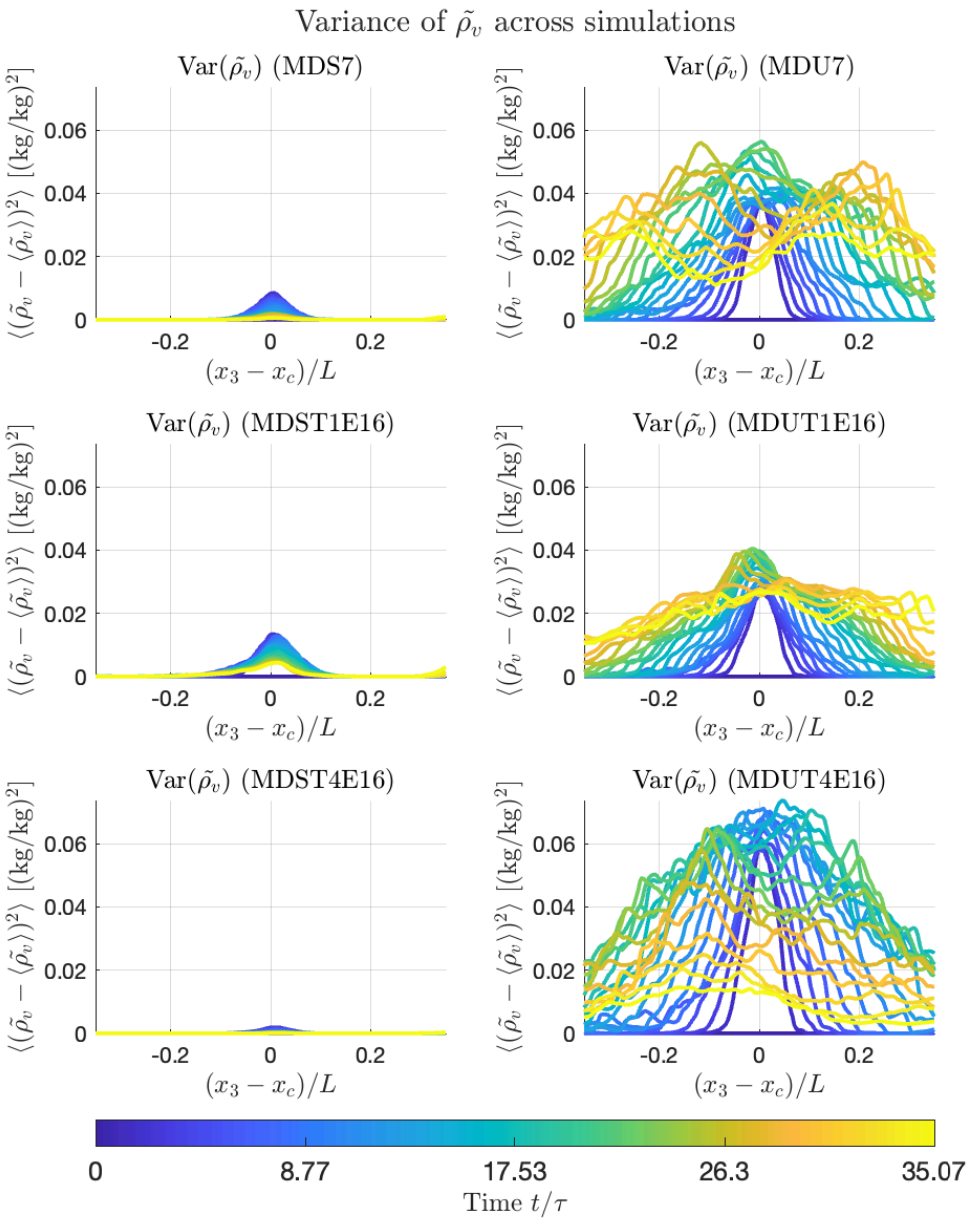

Figure 3.10: Temporal evolution of the vertical profiles of the variance of normalized vapor density , Var$[\tilde{\rho}_v]$ for different mono-disperse simulations. The colors represent the normalized time t/τ_0. We have the stable cases on the left and unstable ones on the right.

At intermediate times, the skewness remains positive over a broad vertical extent, indicating the persistence of moist updrafts and the predominance of upward moisture transport as the unstable stratification sustains vigorous convective overturning. Overall, the opposite signs and temporal evolution of the skewness in stable and unstable configurations clearly capture the contrasting mechanisms of entrainment and mixing acting across the cloud–clear air interface.

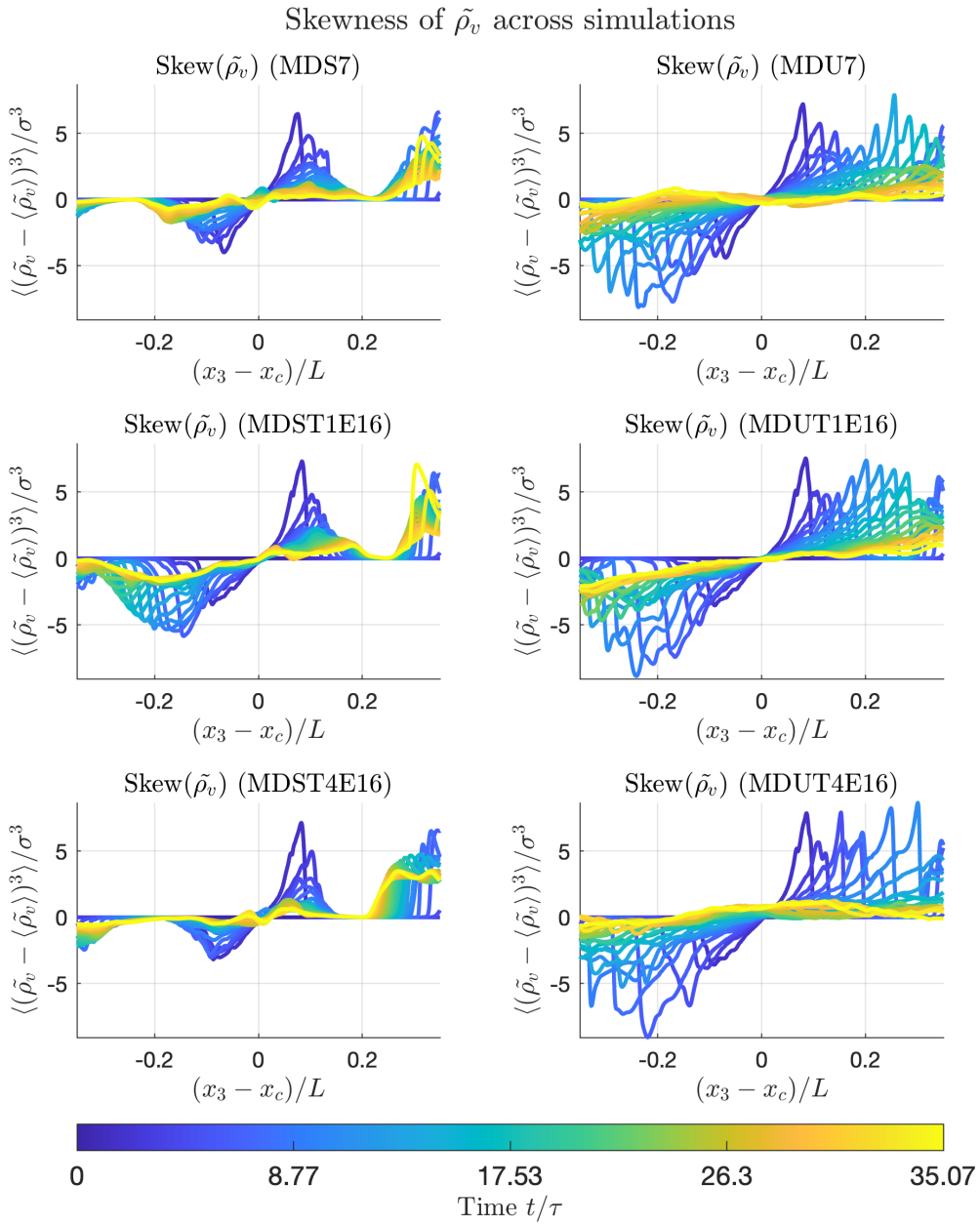

Figure 3.11: Temporal evolution of the vertical profiles of the skewness of normalized vapor density Skew$[\tilde{\rho}_v]$ for different simulations. The colors represent the normalized time t/τ_0. We have the stable cases on the left and unstable ones on the right.

Figure 3.12 reports the temporal evolution of the kurtosis of the normalized vapor density fluctuations, $\langle(\tilde{\rho}_v - \langle\tilde{\rho}_v\rangle)^4\rangle/\sigma^4$, for all simulated cases, with stable configurations shown on the left and unstable ones on the right. In the stably stratified cases, the kurtosis reaches its highest values for the smallest ΔT, indicating strong intermittency associated with sharp gradients in vapor concentration across the interface. The pronounced peaks localized around the transition region reflect the occurrence of rare, intense vapor anomalies—typical of regions where turbulent mixing competes with stratification. As the stratification weakens (larger ΔT), the kurtosis profiles become smoother, with enhanced values extending on the clear-air side, suggesting the presence

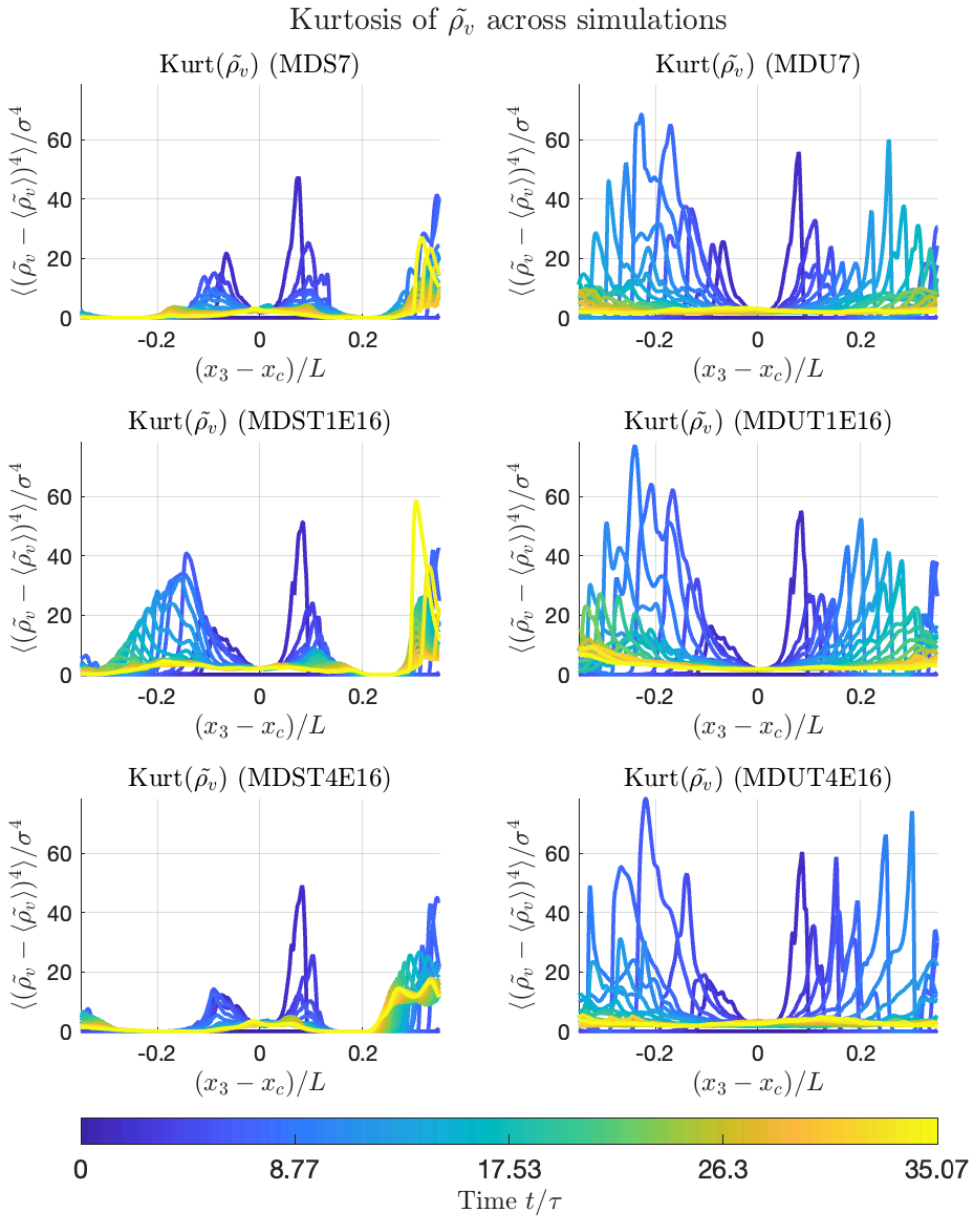

Figure 3.12: Temporal evolution of the vertical profiles of the skewness of normalized vapor density Kurt$[\tilde{\rho}_v]$ for different simulations. The colors represent the normalized time t/τ_0. We have the stable cases on the left and unstable ones on the right.

of intermittent entrainment events and non-Gaussian vapor fluctuations. In contrast, the unstable configurations display a kurtosis evolution that closely resembles that of temperature (see Figure 3.8). Initially, strong peaks appear near the center of the interface, corresponding to localized bursts of vapor transport linked to convective overturning. These peaks progressively move outward from the interface as mixing intensifies, and eventually decay toward lower values as the flow becomes more homogeneous. The overall reduction of kurtosis at late times in all simulations indicates that vapor fluctuations gradually approach a nearly Gaussian distribution, consistent with the decay of turbulence and the diminishing role of coherent, intermittent structures.

The statistical profiles exhibit the same physical behaviour as in Fig. 7 of Gallana et al. [31], where, at the fixed time $t/\tau_0 = 6$, the profiles at different stratification levels are shown in a similar manner, albeit with a different domain-size configuration.

3.3 Buoyancy frequency and Froude number

After presenting the scalar statistics in the previous section, we now introduce a set of derived quantities aimed at assessing the role and relative importance of buoyancy effects, which arise from the vertical gradients of scalar fields such as temperature and vapor density.

As a preliminary step, we evaluate the influence of turbulence on the flow dynamics by computing characteristic time and length scales. In particular, we focus on the large-eddy turnover time and the integral length scale, both computed as functions of the vertical coordinate and tracked over time to analyze their temporal evolution. These quantities provide a reference framework for comparing the intensity of turbulence with the effects of buoyancy. The results of this analysis are shown in figures 3.13,3.14,3.15.

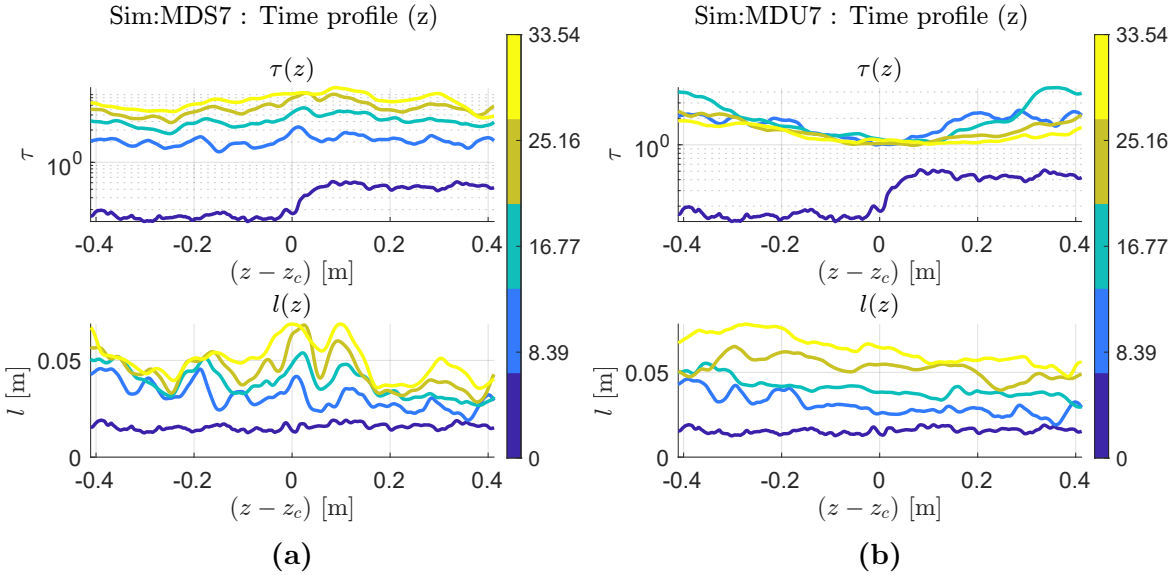

Figure 3.13: Evolution over time of the vertical profiles of the large-eddy characteristic time scale, $\tau(x_3, t)$, and the integral length scale, $L(x_3, t)$, highlighting how turbulence characteristics vary along the vertical direction. Different time-steps are denoted by the color of the curve (spanning from 0 (blue) to 33 t/τ_0 (yellow)). The cases presented are the MDS7 (a) and MDU7 (b).

The integral length scale, here denoted by l, is shown as a function of the vertical coordinate, obtained through the discrete version of (2.14), as described in Chapter 2. The first notable difference is between the stable and unstable cases. In both situations, one may observe a general increase of l throughout the vertical extent, reflecting the progressive enlargement of the turbulent structures as mixing proceeds.

However, the stable cases exhibit a wavy pattern with pronounced peaks near the interface. These localized maxima indicate regions where turbulent activity becomes more organized, suggesting intermittent episodes of enhanced mixing within the otherwise stratified layer. This behaviour reflects the inhomogeneous and anisotropic nature of stably stratified turbulence, in which turbulent motions are typically confined to narrow bands characterized by intensified shear or buoyancy fluctuations. Similar localized peaks of the integral length scale near a density interface have also been reported in laboratory oscillating–grid experiments, where $l(z)$ develops pronounced maxima just above the interface before collapsing at the interface itself [32]. Moreover, the stronger the stratification, the sharper and more pronounced these peaks become, indicating that mixing tends to concentrate within increasingly thin yet energetically significant regions. In contrast, the unstable configurations display a smoother and more monotonic vertical distribution of l, consistent with a more homogeneous and sustained turbulent field, where convective overturning promotes the growth, interaction, and merging of large-scale eddies across the entire layer.

The temporal scale, denoted as τ and defined through Eq. (2.13), represents the large-eddy turnover time. At early stages of the simulation (dark blue curves), the vertical profiles highlight the initial contrast in turbulent kinetic energy (TKE) between the cloudy and the clear-air regions. In both stable and unstable configurations, τ exhibits an overall increase over time, consistent with the decay of turbulence and the progressive enlargement of the dominant eddies. During the initial phase, the unstable cases display a faster growth of the turnover time, characterized by slightly convex profiles along the vertical direction, whereas the stable cases maintain a weak but persistent vertical gradient, reflecting the inhibition of mixing by stratification. In the later stages, the unstable configurations show a turnover of this trend: τ decreases near the interface and eventually reaches a nearly stationary, vertically uniform profile, indicating that the turbulence has achieved a quasi-equilibrium state with balanced production and dissipation.

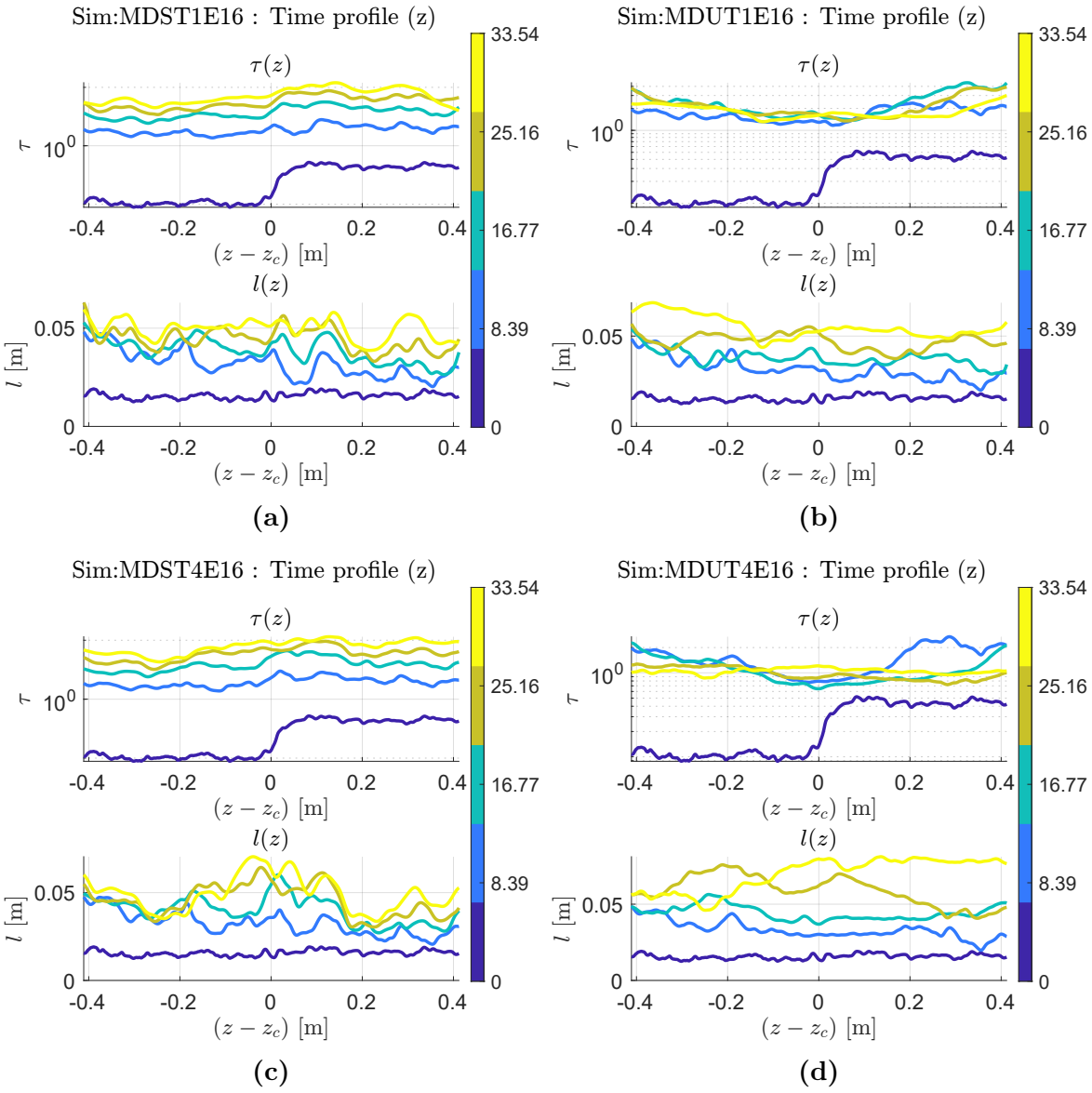

Figure 3.14: Evolution over time of the vertical profiles of the large-eddy characteristic time scale, $\tau(x_3, t)$, and the integral length scale, $L(x_3, t)$, highlighting how turbulence characteristics vary along the vertical direction. Different time-steps are denoted by the color of the curve (from 0 (blue) to 33 t/τ_0 (yellow)). The cases presented are the mono-disperse simulations.

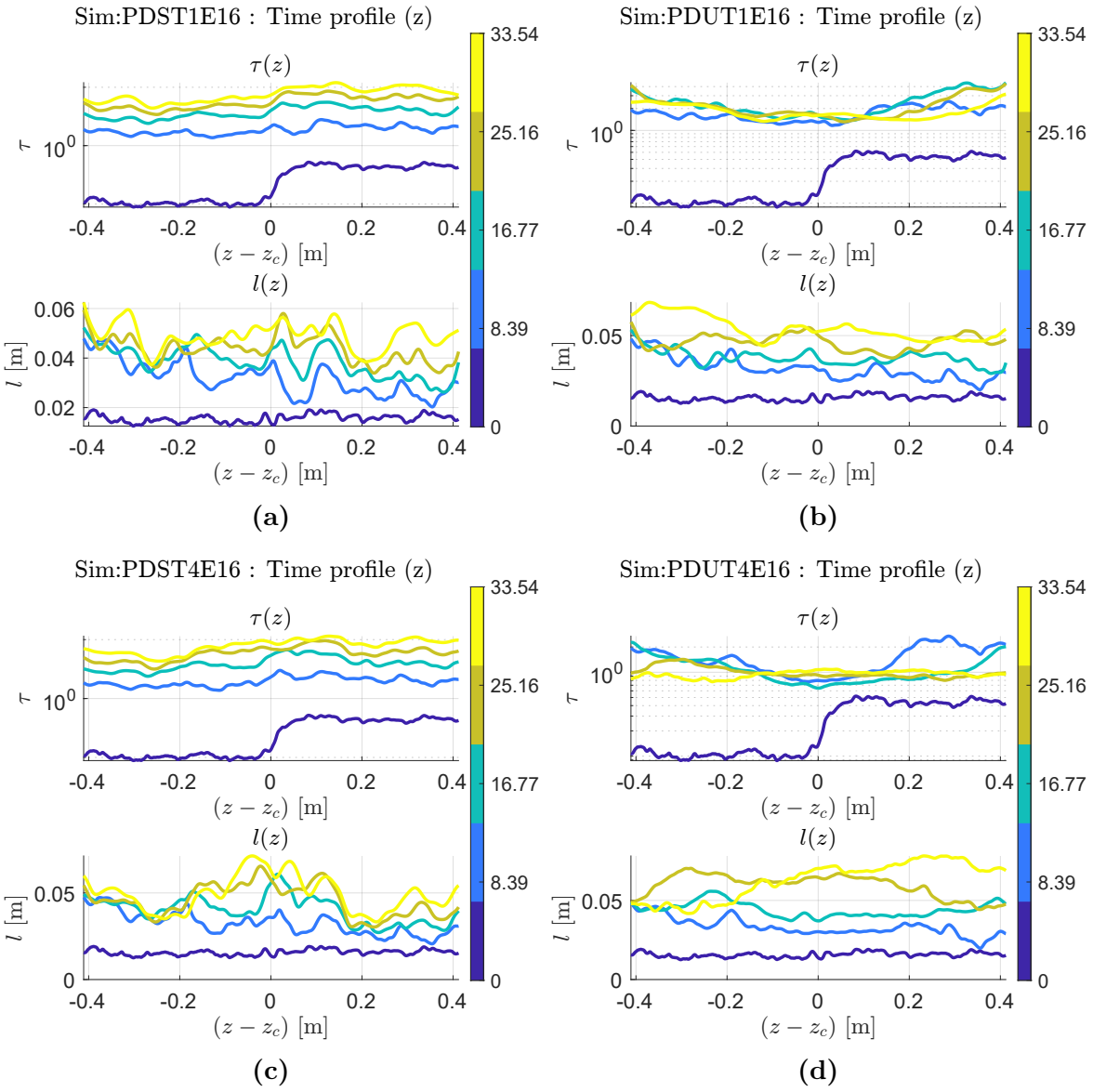

Figure 3.15: Evolution over time of the vertical profiles of the large-eddy characteristic time scale, $\tau(x_3, t)$, and the integral length scale, $L(x_3, t)$, for the poly-disperse simulations. Different time-steps range from 0 (blue) to 33 t/τ_0 (yellow).

Buoyancy frequency

After the previous section, where the statistics of the scalar quantities were presented, we now examine their dynamical impact on the velocity field, which is parametrized through the buoyancy frequency. Figures 3.16 and 3.17 show the vertical and temporal evolution of $\mathcal{N}^2$ for all simulations, including the contribution of moisture to the effective buoyancy frequency. Figure 3.16 shows separately the contributions of temperature and vapor gradients, denoted respectively by $\mathcal{N}_\theta^2 = (g/\theta_0)\, d\overline{\theta}/dz$ and $\mathcal{N}_{q_v}^2 = g\,\beta\, d\overline{q_v}/dz$, while Figure 3.17 displays the combined effective value $\mathcal{N}_{\text{eff}}^2 = \mathcal{N}_\theta^2 + \mathcal{N}_{q_v}^2$, which quantifies the total (unsaturated) buoyancy restoring frequency governing vertical motions.

In the stably stratified configurations (left column), the temperature contribution

$\mathcal{N}_\theta^2$ dominates, exhibiting a sharp positive peak centered around the interface at early times (blue lines). This reflects the presence of a strong thermal stratification that resists vertical displacements. The corresponding vapor term $\mathcal{N}_{q_v}^2$ is negative, since the mean vapor density decreases with height; it therefore acts as a destabilizing correction that slightly reduces the effective stability of the layer. As the stratification becomes stronger, this vapor contribution becomes increasingly negligible, as vertical mixing is suppressed and the humidity gradient remains weak. During the temporal evolution, both $\mathcal{N}_\theta^2$ and $\mathcal{N}_{q_v}^2$ gradually decrease in magnitude, indicating that turbulent entrainment erodes the mean gradients. Moreover, the peak of $\mathcal{N}_\theta^2$ progressively shifts toward the clear-air side, especially in lower stratified cases, signalling that the interface is eroded more rapidly within the cloudy, turbulent region, while the sharper gradient persists in the less mixed, stably stratified air above.

Figure 3.17 illustrates the total effective buoyancy frequency $\mathcal{N}_{\text{eff}}^2$, obtained by combining the two contributions discussed above. In the stable cases, the resulting $\mathcal{N}_{\text{eff}}^2$ retains a well-defined positive peak, whose amplitude decreases over time as mixing proceeds. The clear temporal weakening of this maximum is a signature of the gradual erosion of stratification and of the reduction of buoyancy forces as the interface thickens.

A notable feature appears in the MDST1E16 configuration, where we clearly observe a displacement of the maximum temperature gradient toward the clear-air region, characterized by lower turbulent kinetic energy. This behaviour is consistent with the fact that, under relatively weak stratification, the effective turbulent diffusivity follows the vertical distribution of turbulence, with $K_{\text{turb}} \sim u'l$(Prandtl & Taylor). Where K_{turb} decreases, the scalar-flux balance requires a corresponding increase in the mean gradient, causing the maximum of $|\partial_z T|$ to migrate toward the less energetic region. Conversely, in more strongly stratified cases the interface acts as a dynamically stiff barrier: the stabilizing term $\mathcal{N}^2$ controls the effective diffusivity and forces K_{turb} to collapse at the interface. As a result, the temperature gradient remains anchored at the level of strongest stratification, and no displacement of its maximum is observed.

In contrast, the unstable configurations (right column) exhibit $\mathcal{N}_{\text{eff}}^2 < 0$ in the central region, indicating the persistence of convective instability at early times. As mixing proceeds, these negative peaks broaden and progressively lose coherence, giving rise to a disordered distribution of weakly positive and negative values oscillating around neutrality — a signature of the transition from organized convection to a fully mixed, quasi-neutral layer.

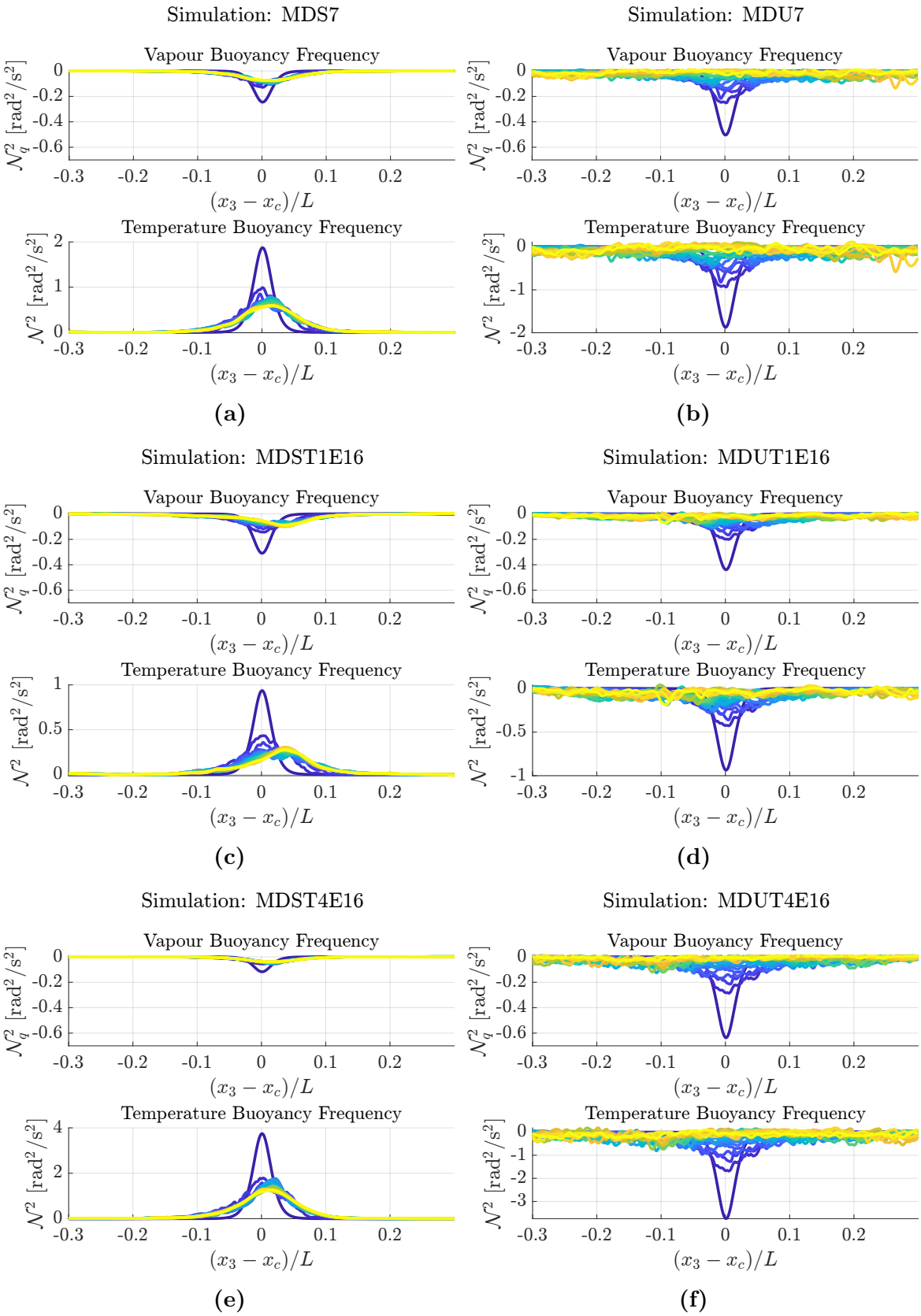

Figure 3.16: For each mono-disperse simulation we have the contribution to the Buoyancy frequency, from the vapour density gradient, on the top and from the temperature. The respective frequency number are denoted by $\mathcal{N}_q$ and $\mathcal{N}$.

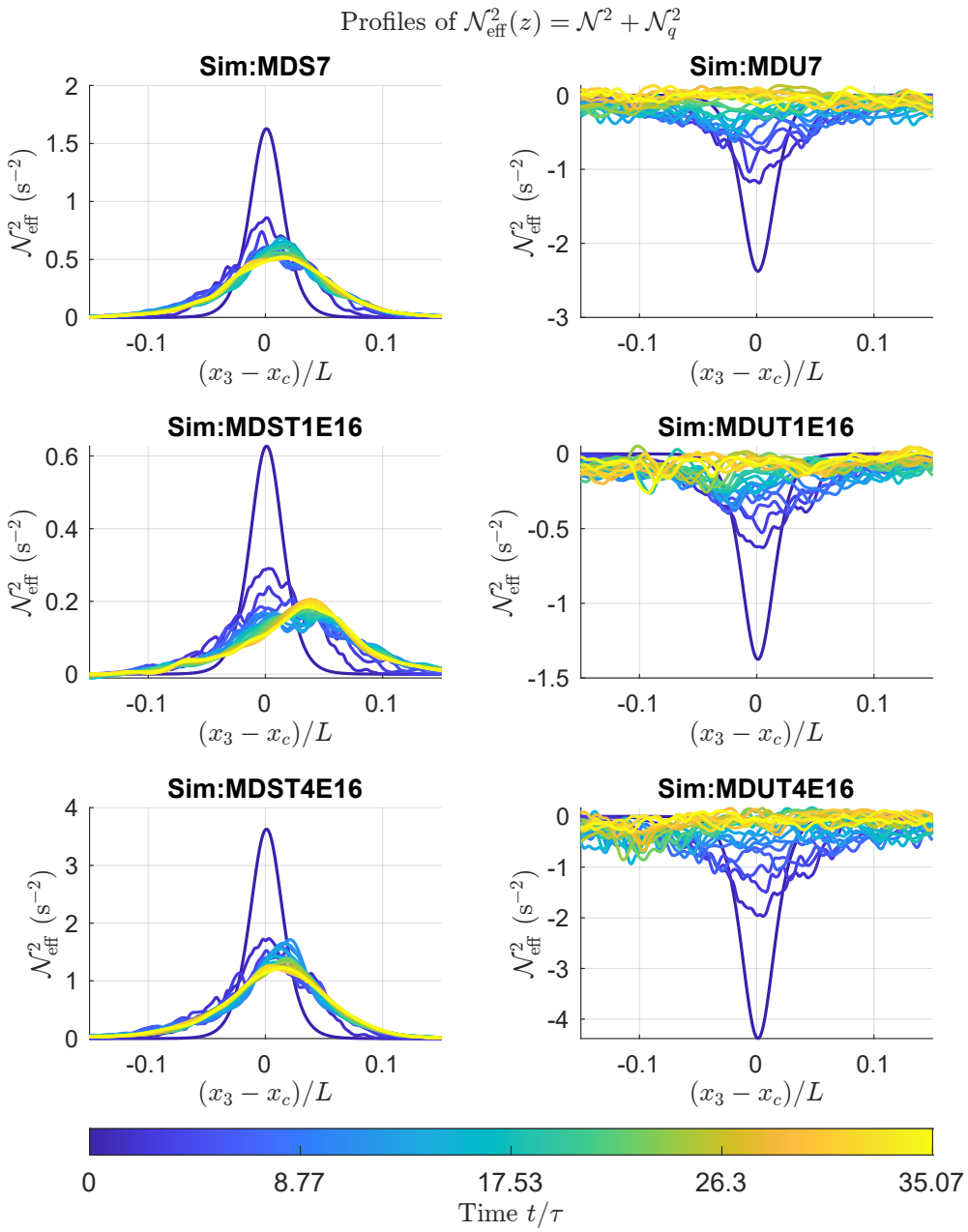

Figure 3.17: Unsatured Buoyancy frequency $\mathcal{N}_{eff}(x_3, t_i/\tau_0)$ vertical profiles at each time instance, for the mono-disperse simulations.

Overall, the comparison between the separate and combined representations highlights the relative importance of the thermal and moist components in modulating stratification. In strongly stable regimes, the moisture term remains secondary, and the buoyancy frequency is mainly controlled by the temperature gradient. Since the total vapor content is constant, the gradient of vapor density preserves its direction across all cases. Therefore, when the temperature gradient reverses in the unstable configurations, the vapor contribution retains the same sign, partially compensating or enhancing the thermal term depending on the relative magnitude of the two gradients. This behavior explains why the moist contribution becomes negligible in strongly stratified cases but remains comparable in weakly stratified or convective conditions.

The evolution of $\mathcal{N}^2_{\text{eff}}(z,t)$ thus captures the progressive balance between buoyancy restoration, turbulent mixing, and convective destabilization, providing a preliminary diagnostic of the transition from wave-dominated to turbulence-dominated regimes.

To complement the vertical analysis, Figure 3.18 shows the temporal evolution of the buoyancy frequencies averaged within the mixing layer, as defined in Section 2.3. The quantity is obtained by computing $\mathcal{N}^2$ and $\mathcal{N}\text{eff}^2$ over the vertical coordinates corresponding to the instantaneous mixing region, thus providing a representative measure of the mean stratification experienced by turbulent motions at the interface. At early times, the magnitude of $\langle\mathcal{N}^2\rangle$mixing reflects the imposed thermal contrast, with strongly stable configurations showing large positive values and unstable ones exhibiting negative ones. As time evolves, both groups approach smaller absolute values, indicating the progressive weakening of stratification within the layer due to entrainment and mixing. Stable cases relax toward weakly positive, nearly steady values consistent with a residual buoyancy restoring force, whereas unstable ones rise toward zero, marking the approach to a quasi-neutral equilibrium. The inclusion of the vapor contribution in $\langle\mathcal{N}\text{eff}^2\rangle$mixing slightly modifies the overall amplitude but does not alter the general trend. This confirms that temperature remains the dominant driver of buoyancy dynamics, while moisture plays a secondary yet coherent role in the evolution toward a mixed state.

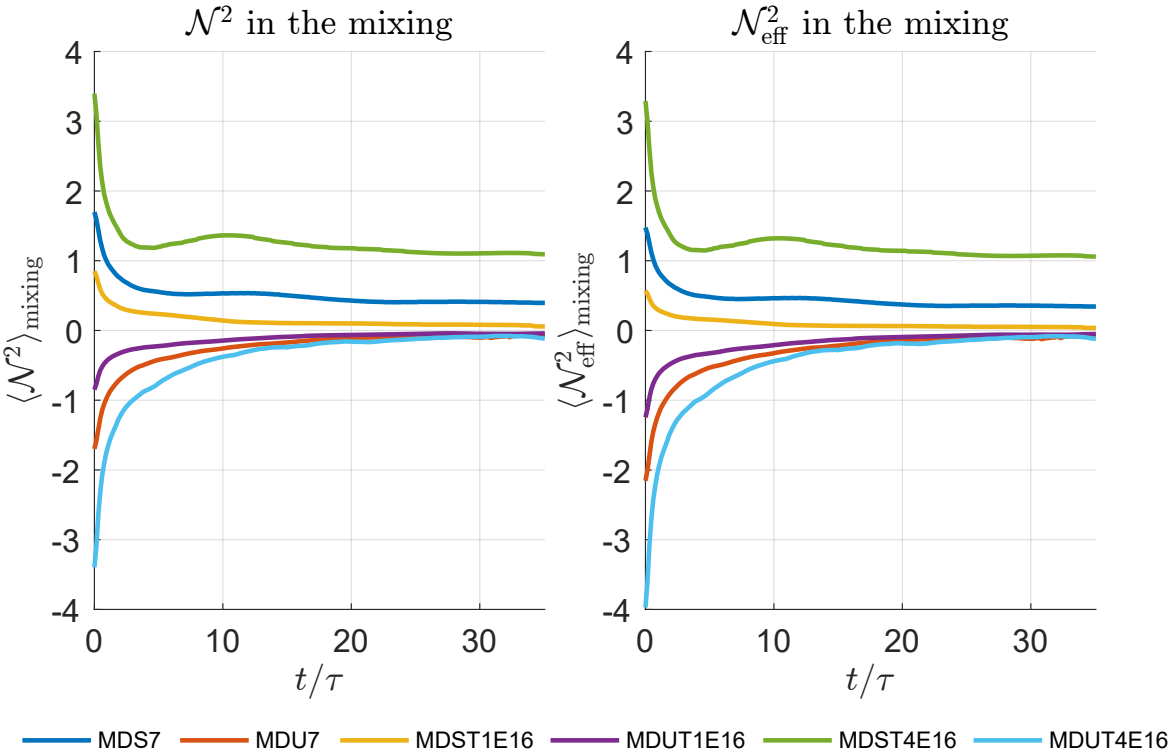

Figure 3.18: On the left we have the evolution in time of $\mathcal{N}^2$ averaged in the mixing, while on the right the evolution in time of effective Buoyancy frequency.

Froude number

Finally, we evaluate when and where turbulence dominates over buoyancy, and conversely when buoyancy controls the flow dynamics. The governing parameter is the Froude number, previously defined in Eq. (2.12), which expresses the ratio between the turbulent and buoyancy time scales. Values of $Fr > 1$ indicate turbulence-dominated motion, while $Fr < 1$ corresponds to buoyancy-controlled regimes.

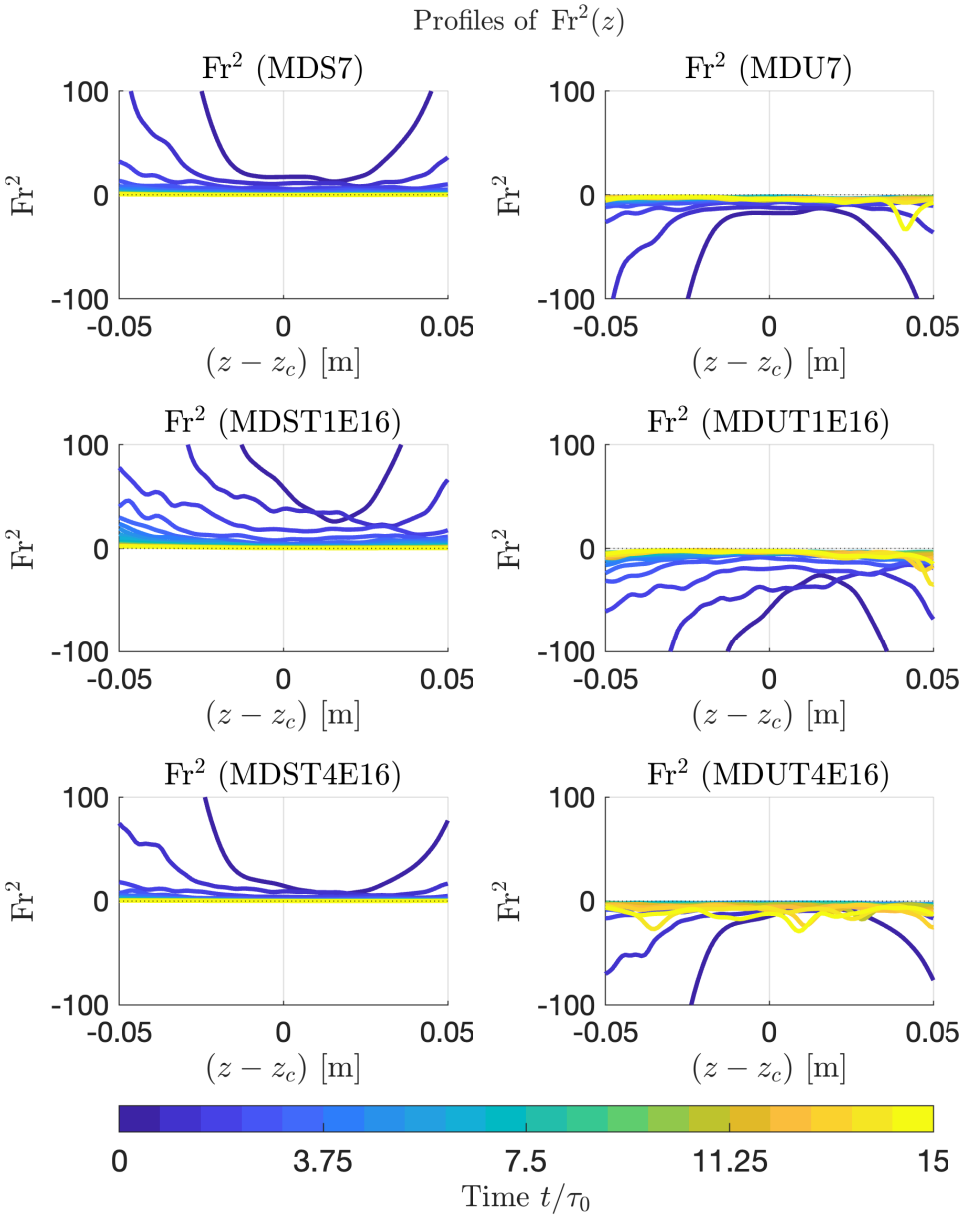

Figure 3.19: Squared Froude number values at each z coordinate in a narrow layer between $[-0.05, 0.05]$ m, for each mono-disperse simulation—the stable cases are on the left and the unstable ones on the right—each color denotes a time instance.

From Figure 3.19, one can observe the specular evolution between stable and unstable stratifications, with stable cases on the left and unstable ones on the right.

At early times, both configurations exhibit profiles that are convex (concave for the unstable cases) near the interface, showing a minimum (maximum) at the center where stratification is strongest. As time progresses, the profiles broaden, indicating the progressive thickening of the initially sharp stratified layer. The magnitude of this broadening depends on the imposed stratification intensity. Around $t/\tau_0 \approx 15$, the squared Froude number approaches unity and then decreases below it in both regimes, highlighting the increasing importance of buoyancy as turbulence decays. The unstable cases display a more irregular and intermittent behaviour, consistent with the coexistence of convective and oscillatory motions.

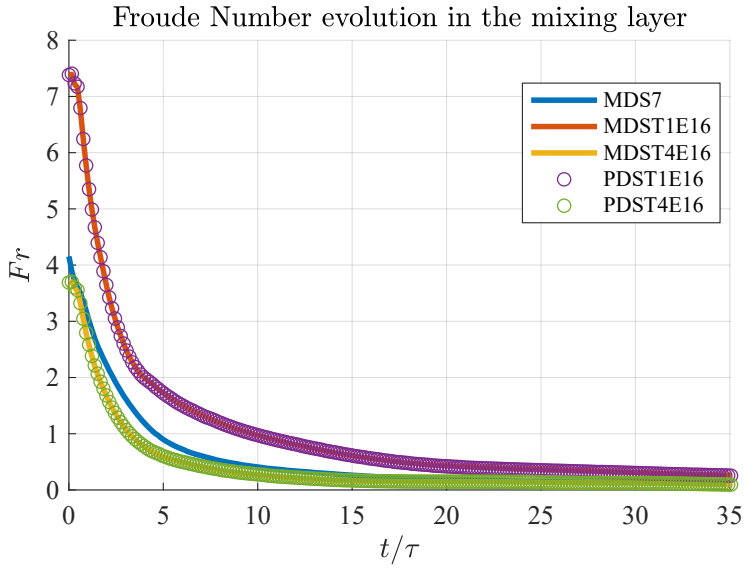

Figure 3.20: Froude number evolution in time calculated in the mixing layer through different cases. (The circles denotes the poly-disperse counterpart)

Focusing now on the stable configurations, Figure 3.20 shows the temporal evolution of Fr evaluated within the mixing layer (as defined in Section 2.3). Clear differences emerge among the three temperature gradients. The MDST1E16 case ($\Delta T = 1$ K) exhibits the highest values of Fr, nearly twice those of the other simulations at early times, before buoyancy starts to dominate after approximately $t/\tau_0 = 10$. The MDS7 ($\Delta T = 2$ K) and MDST4E16 ($\Delta T = 4$ K) cases display similar behaviour, both reaching $Fr < 1$ after roughly $t/\tau_0 = 5$. The different energy ratios between the cloudy and clear-air regions, $E^{\text{cloud}}/E^{\text{air}}$, modulate the rate of exponential decay of Fr, with higher ratios leading to a faster decrease. Finally, the circled curves represent the poly-disperse simulations, which exhibit indistinguishable behavior from their mono-disperse counterparts. Fig. 3.21 shows the time evolution of the squared Froude number together with exponential fits of the form $Fr^2(t) = c_0 + c_1 e^{-bt/\tau_0}$, in correspondence with the trends reported in Fig. 4 of Gallana et al. [31]. The exponential model accurately captures the initial decay, but it systematically underestimates the late–time decrease.

In summary, the temporal evolution of the Froude number and the associated integral quantities delineates a clear picture of the transition from active turbulent mixing to stratified, quasi-laminar motion. To gain deeper insight into the underlying dynamical processes, the following section focuses on a spectral analysis of the velocity field itself, examining how energy and buoyancy are distributed and exchanged across temporal and spatial scales.

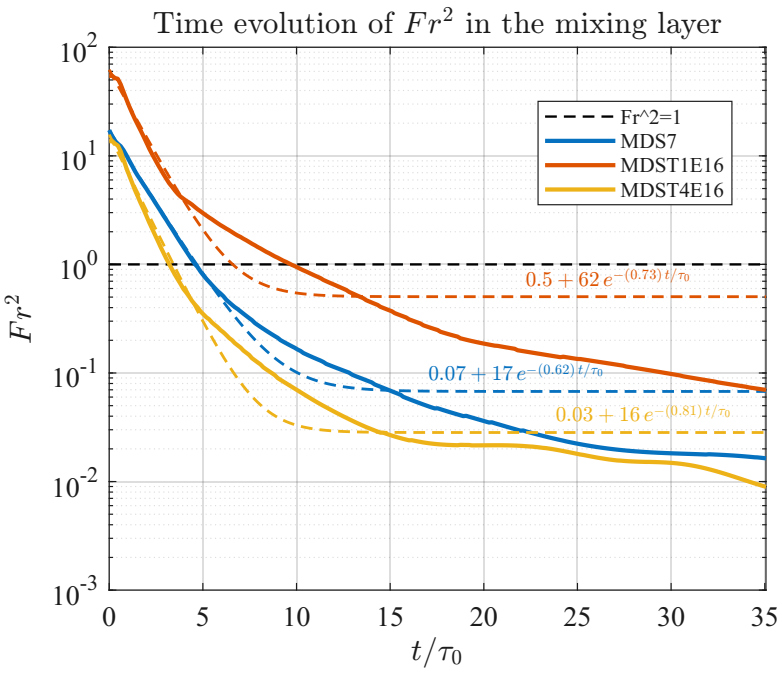

Figure 3.21: Time evolution of Fr^2 for all mono-disperse stable simulations . Solid lines show the instantaneous values, while dashed curves denote exponential fits $Fr^2 = c_0 + c_1 e^{-b\,t/\tau_0}$. A reference line at $Fr^2 = 1$ is included.

3.4 Spectral Analysis

Given that the numerical solver is based on a pseudo-spectral formulation, it is natural to extend the analysis to spectral space. This representation provides a direct view of how kinetic energy is distributed among the Fourier modes resolved by the simulation, and allows for a precise identification of the dominant spatial and temporal scales involved in the flow dynamics. In stratified turbulence, such spectral information is particularly insightful: turbulent motions populate a broad continuum of wavenumbers, while internal gravity waves leave distinct signatures along dispersion branches controlled by the local buoyancy frequency. By analyzing both spatial spectra $E(\mathbf{k}, t)$ and joint frequency–wavenumber spectra, we can distinguish between turbulence-dominated and wave-dominated regimes, and follow their evolution during the decay. In addition to these global spectra, local time series of the velocity field at fixed spatial positions were examined through temporal Fourier transforms. This complementary analysis at constant (x_0, y_0, z_0) enables the characterization of intermittent bursts and the detection of coherent wave-like oscillations in physical space.

Starting from the Fig. 3.22, the six panels display the temporal evolution of the isotropic energy spectrum $E(\kappa)$ for stably (S) and unstably (U) stratified cases. At early times, all spectra exhibit a pronounced peak around $\kappa \simeq 61$ m^{-1}, corresponding to the dominant large-scale mode. In the stably stratified runs (MDS7, MDST1E16, MDST4E16), this peak progressively shifts towards smaller wavenumbers (approximately $\kappa \simeq 24.5$ m^{-1} at late times), not because of an inverse energy transfer, but rather due to the preferential decay of small-scale motions. Stable stratification damps vertical fluctuations and inhibits the forward cascade, allowing the large-scale structures to persist while the total kinetic energy continues to decay. As a consequence, the inertial range becomes shorter and the spectrum steepens at intermediate wavenumbers. In contrast, the unstably stratified cases (MDU7, MDUT1E16, MDUT4E16) reveal a distinct re-energisation of the flow. Initially, energy grows at intermediate and large scales, signalling the onset of buoyancy-driven motions and the breakdown of the mean stratification. This growth subsequently feeds the smaller scales through a renewed forward cascade, leading to an overall increase of spectral energy at high κ. Hence, unstable stratification promotes a two-stage revival of turbulence: first through the amplification of large-scale overturning structures, and then through the restoration of small-scale activity approaching the Kolmogorov $k^{-5/3}$ behaviour.

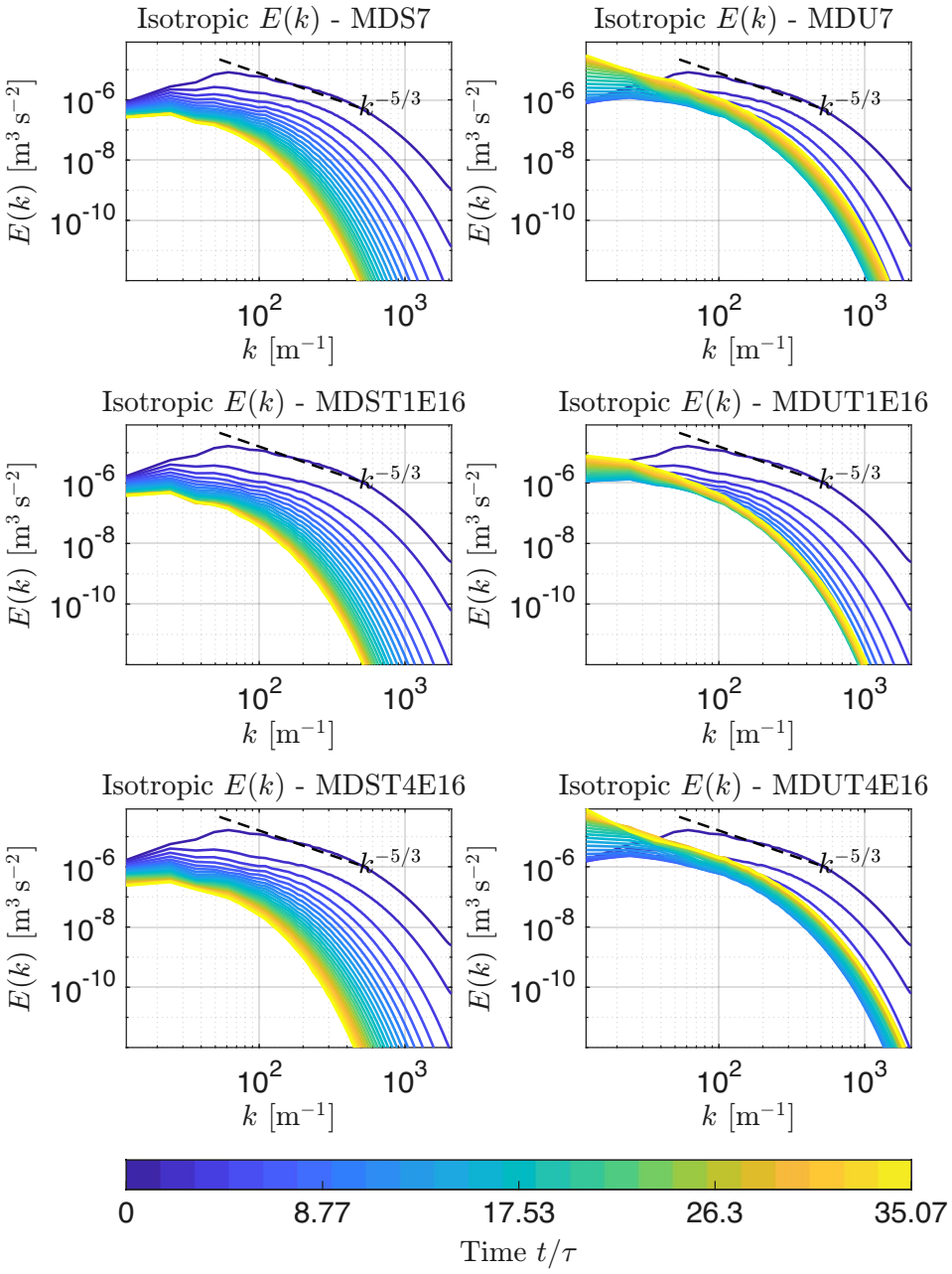

Figure 3.22: Isotropic Energy spectra $E(\kappa)$ are plotted for each simulation— we have the stable cases on the left and unstable on the right, which are clearly identified by their behaviour asymptomatically; each color represents a time instances as described by the colorbar (blue is the beginning and yellow the last simulated instance). The dotted line represents the theoretical $k^{-5/3}$ Kolmogorov scaling.

Afterwards, this section presents the temporal spectra shown in Figures 3.23–3.40. Each figure reports the temporal spectra of velocity and acceleration evaluated at fixed locations within the domain. At each point, the time series has been spatially averaged over a small horizontal neighbourhood, as described in Section 2.3. In the first row of

each figure, the velocity and acceleration components are plotted as functions of time, while the second to fourth rows display the corresponding temporal spectra for each component. This analysis has been carried out for all mono-disperse simulations. For each configuration, three representative points have been selected: one at the interface region (approximately $(0, 0, 0)$ m), one within the cloudy region (around $(0, 0, -0.2)$ m), and one in the clear-air region (around $(0, 0, 0.2)$ m).

Temporal spectra for the stably stratified case (MDS7). Figures 3.23–3.25 show the temporal evolution of velocity and acceleration for the stably stratified simulation (MDS7). The spectra are computed as functions of the angular frequency ω after applying a symmetric taper (Hann or Hamming window) to each signal, to mitigate spectral leakage and obtain smoother frequency distributions. The total record length corresponds to about 35–40 t/τ_0 with $\tau_0 = 0.35$ s, giving a maximum period $T_{\max} \simeq 14$ s and a spectral resolution of

$$\Delta\omega = \frac{2\pi}{T_{\max}} \simeq 0.45 \text{ rad s}^{-1}.$$

As a result, the spectral accuracy at low frequencies is limited, and the broad peaks observed at small ω represent the aggregation of the lowest resolvable modes rather than discrete oscillations. In the strongly stratified zone, the acceleration spectra display a dominant peak around $\omega \simeq 1$ rad s^{-1}, which closely matches the local buoyancy frequency $\mathcal{N} \in [\sqrt{0.5}, \sqrt{1.5}]$ rad s^{-1} (0.7–1.2 rad s^{-1}). This correspondence suggests that the temporal dynamics are governed by internal gravity waves generated by the stable stratification near the interface. Above and below this range, the spectral energy decays rapidly, indicating that motions faster than the buoyancy period are effectively damped.

It is also noteworthy that a weaker but still recognizable peak around $\omega \simeq \mathcal{N}$ is observed even in regions relatively far from the stratified layer, particularly in the clear-air region ($z \simeq 0.19$ m). This behaviour suggests that part of the internal-wave energy produced near the interface propagates outside the strongly stratified zone. Internal gravity waves with frequencies $\omega \lesssim \mathcal{N}$ can travel through neighbouring regions of weaker stratification as long as the local dispersion relation $\omega = \mathcal{N}\, k_h/|\mathbf{k}|$ is approximately satisfied. In layers where $\mathcal{N}^2 \approx 0$, these waves can persist as evanescent or pressure-coupled modes, retaining part of their oscillatory energy before being gradually attenuated. The reduced amplitude of the spectral peak away from the interface therefore reflects partial transmission and progressive damping of internal-wave energy, rather than the presence of locally generated oscillations.

The acceleration spectra, as expected from $\hat{a}(\omega) = i\,\omega\,\hat{u}(\omega)$, enhance higher frequencies. The amplitude of both velocity and acceleration spectra decreases with height: the cloudy region ($z \simeq -0.21$ m) exhibits the strongest energy and the broadest frequency

content, the interface ($z \simeq 0$ m) shows a balanced but weaker signal, and the clear-air region ($z \simeq 0.19$ m) displays the lowest and steepest spectra. Overall, the temporal analysis confirms that the stably stratified flow is dominated by oscillations around the buoyancy frequency, with energy progressively confined to large-scale, low-frequency motions as turbulence decays away from the interface.

Temporal spectra for the unstably stratified case (MDU7). Figures 3.26–3.28 show the temporal evolution of velocity and acceleration for the unstably stratified simulation (MDU7). The spectra are computed as functions of the angular frequency ω, using the same temporal window and averaging procedure adopted for the stable cases. In this configuration, the total record length corresponds to $T_{\max} \simeq 35\,\tau_0 = 12.25$ s, which gives a spectral resolution of

$$\Delta\omega = \frac{2\pi}{T_{\max}} \simeq 0.51 \text{ rad}\,\text{s}^{-1}.$$

This defines the lowest resolvable frequency and limits the sharpness of the peaks at small ω.

In contrast to the stable case, the velocity and acceleration signals exhibit larger and more irregular fluctuations, indicating the development of convective overturning and vigorous turbulence. The corresponding temporal spectra show no distinct peak around the nominal buoyancy frequency ($\mathcal{N} \in [\sqrt{0.5},\ \sqrt{1.5}]$ rad s^{-1} in the stable configuration), confirming that oscillatory wave-like motions are absent once the stratification becomes unstable. Instead, spectral energy is distributed in an irregular and fragmented manner across a wide range of frequencies, with significant amplitudes extending up to $\omega \sim$ 10–20 rad s^{-1}. This non-uniform spectral behaviour reflects the collapse of the stratified-layer dynamics and the emergence of a strongly non-stationary convective regime dominated by non-linear interactions.

The energy initially appears at low frequencies, corresponding to the slow growth of large-scale buoyant plumes, and progressively extends toward higher ω as turbulence develops and energy cascades to smaller temporal scales. Acceleration spectra are strongly enhanced at high frequencies, as expected from $\hat{a}(\omega) = i\,\omega\,\hat{u}(\omega)$, highlighting the presence of fast temporal fluctuations and vigorous small-scale activity. Overall, the MDU7 spectra confirm that no internal-wave regime develops under unstable stratification. Instead, the flow is dominated from the outset by buoyancy-driven overturning motions, which rapidly evolve into a fully turbulent convective state. The absence of a spectral peak near $\mathcal{N}$, together with the broadband distribution of energy, demonstrates that the flow is fully dominated by turbulent convective motions and no longer constrained by buoyancy oscillations.

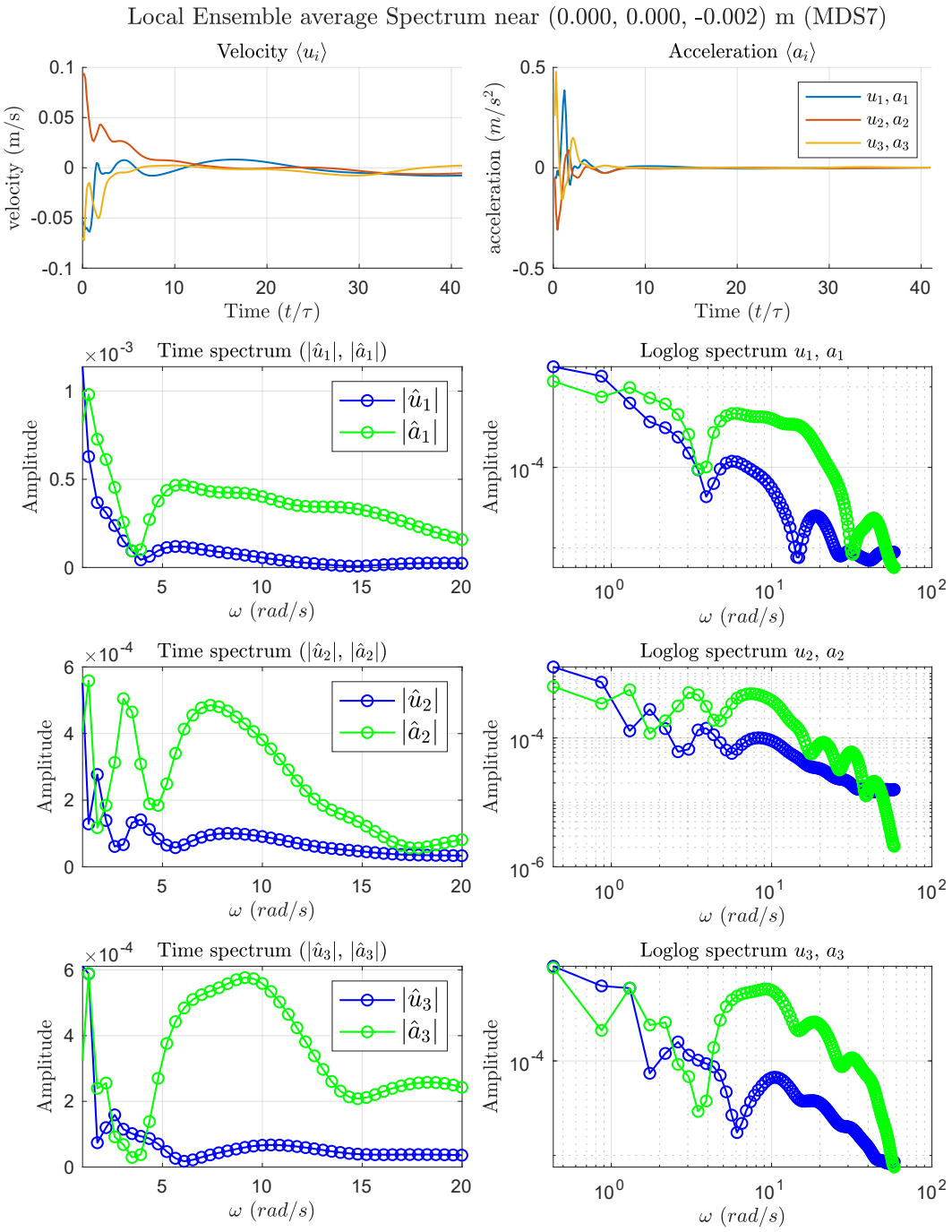

Figure 3.23: Temporal spectra of velocity and acceleration at $z \simeq -0$ m for the stably stratified case (MDS7). A distinct peak near $\omega \simeq 1$ rad s^{-1} indicates the dominance of oscillations at the local buoyancy frequency.

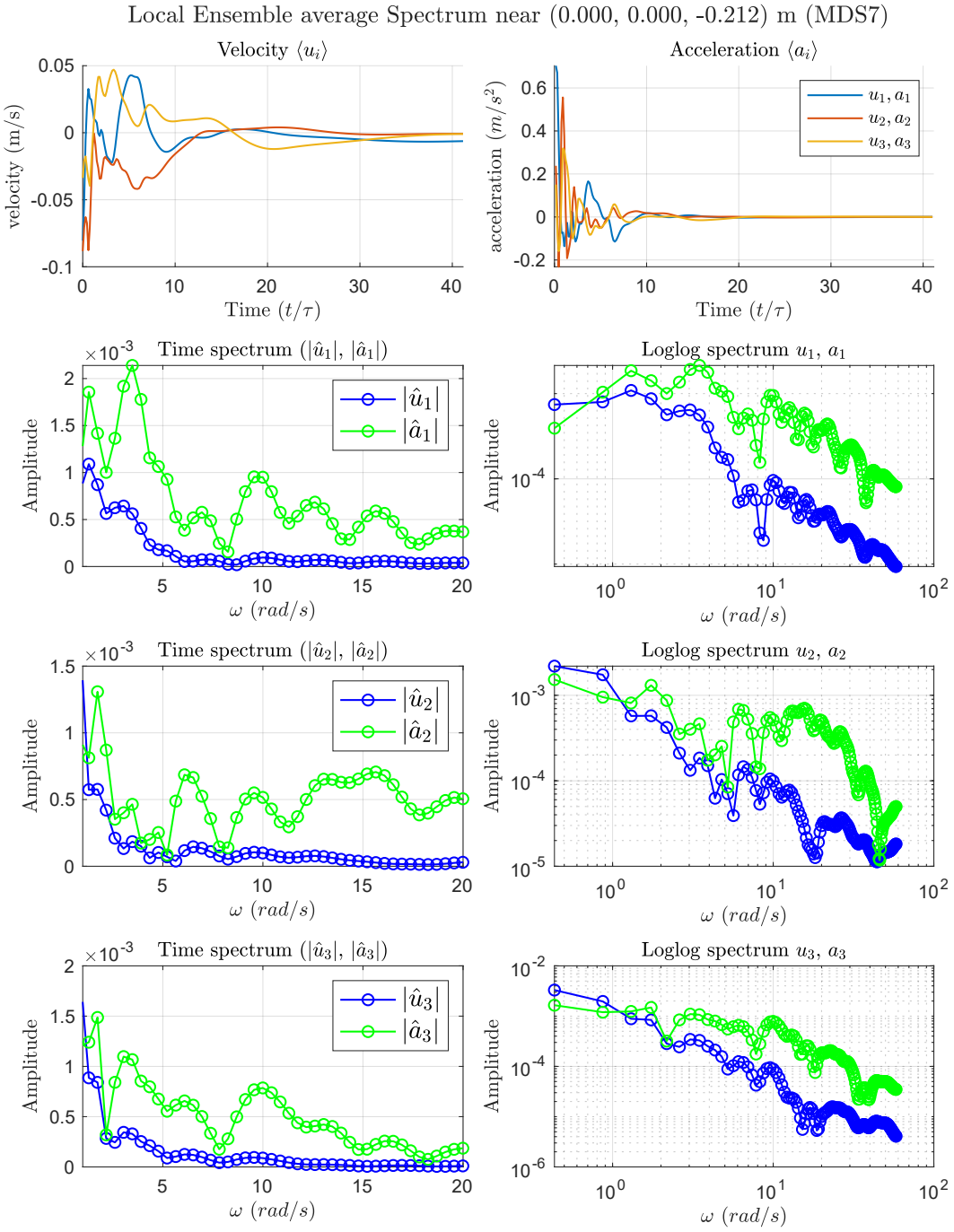

Figure 3.24: Temporal spectra of velocity and acceleration at $z \simeq -0.2$ m for the stably stratified case (MDS7). A distinct peak near $\omega \simeq 1$ rad s^{-1} indicates the dominance of oscillations at the local buoyancy frequency.

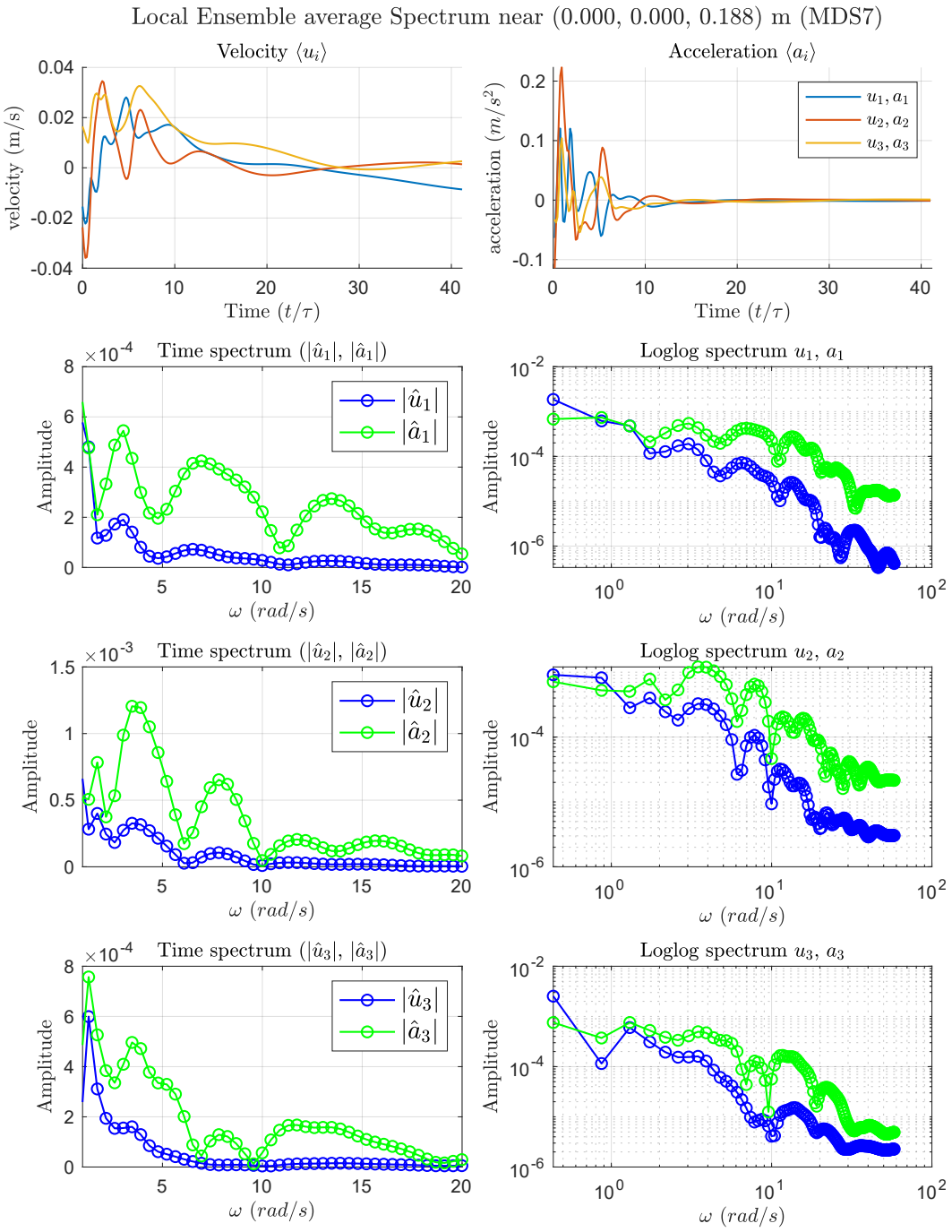

Figure 3.25: Temporal spectra of velocity and acceleration at $z \simeq 0.2$ m for the stably stratified case (MDS7). A distinct peak near $\omega \simeq 1$ rad s^{-1} indicates the dominance of oscillations at the local buoyancy frequency.

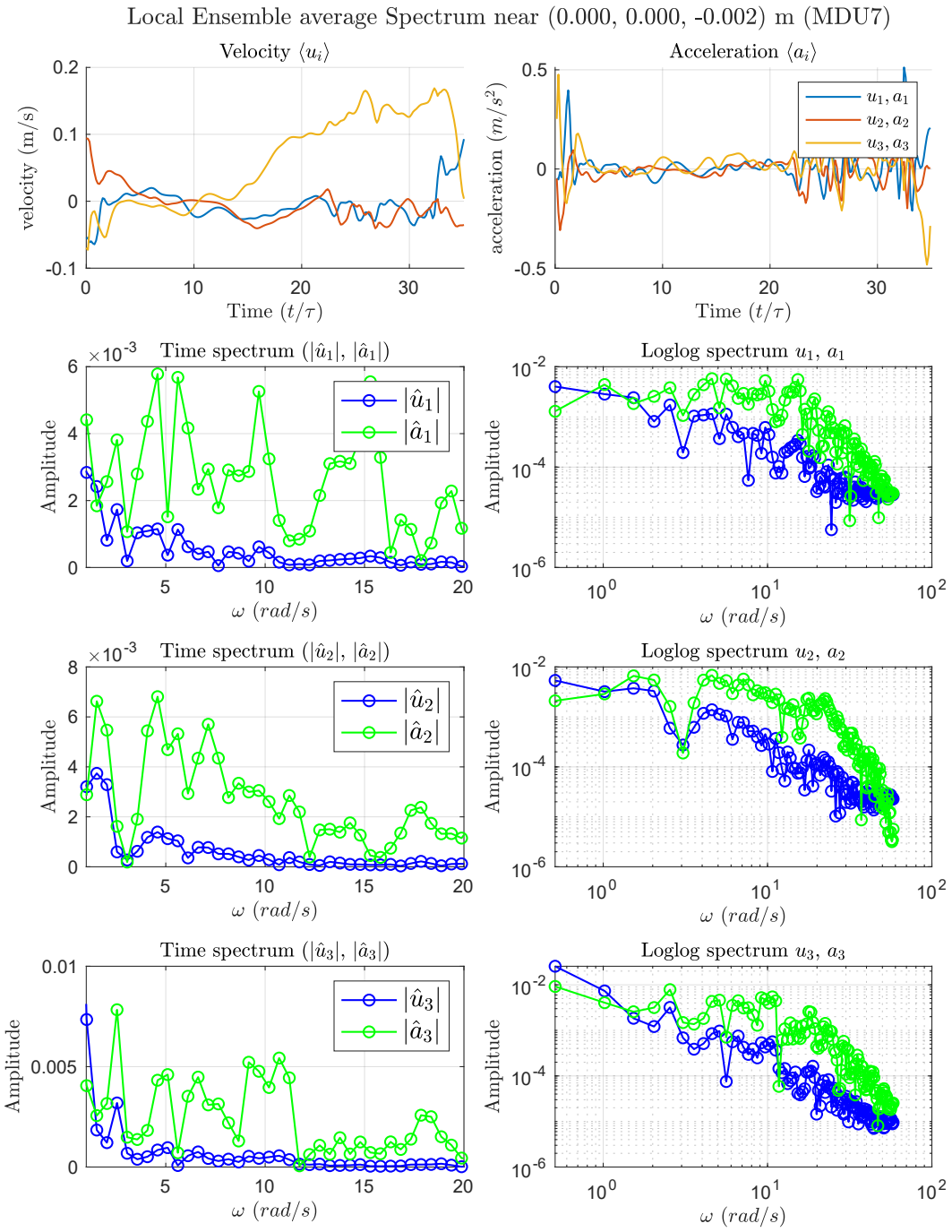

Figure 3.26: Temporal spectra of velocity and acceleration at $z \simeq 0$ m for the unstably stratified case (MDU7). No peak at $\omega \simeq 1$ rad s^{-1} is observed; energy spreads over a wide frequency range due to active convection.

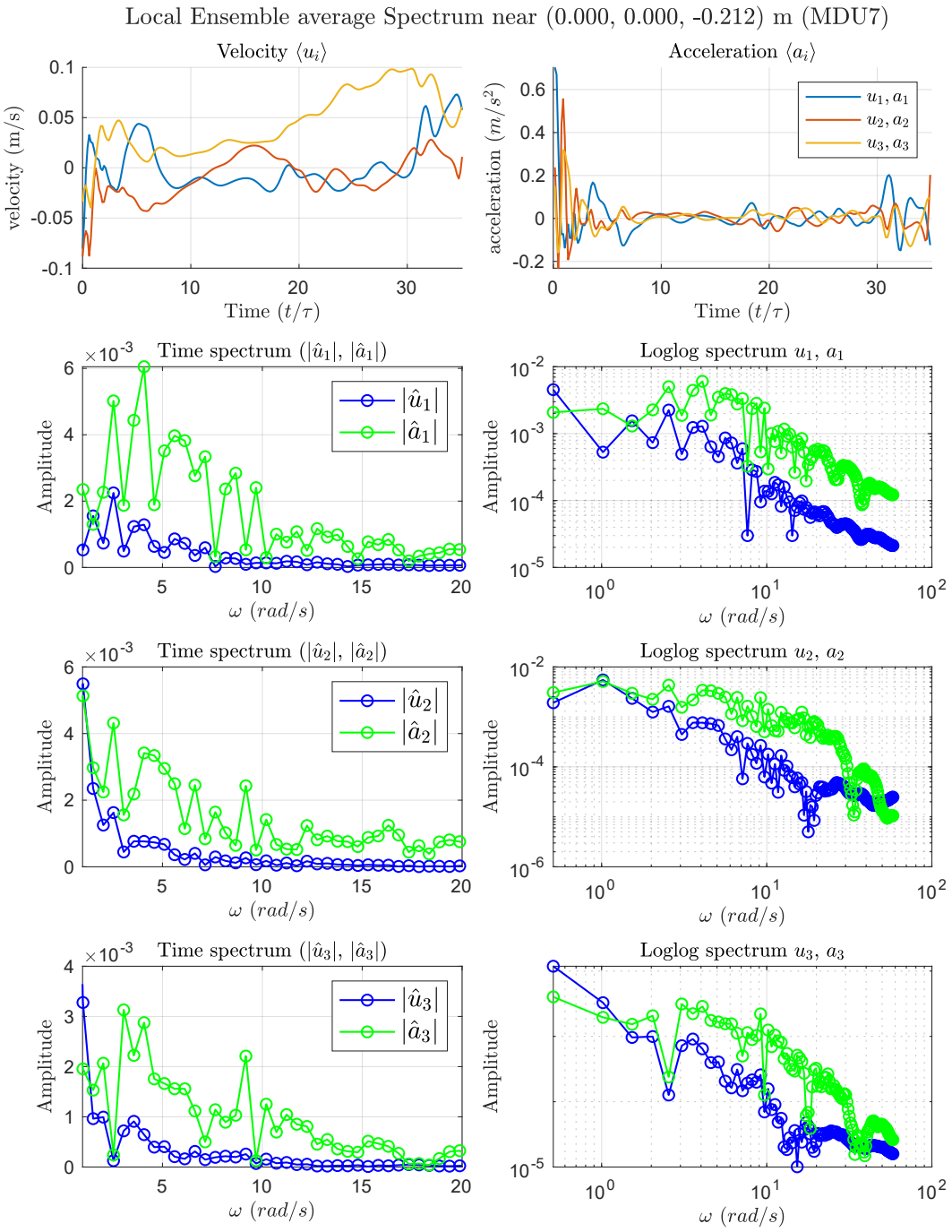

Figure 3.27: Temporal spectra of velocity and acceleration at $z \simeq -0.2$ m for the unstably stratified case (MDU7). No peak at $\omega \simeq 1$ rad s^{-1} is observed; energy spreads over a wide frequency range due to active convection.

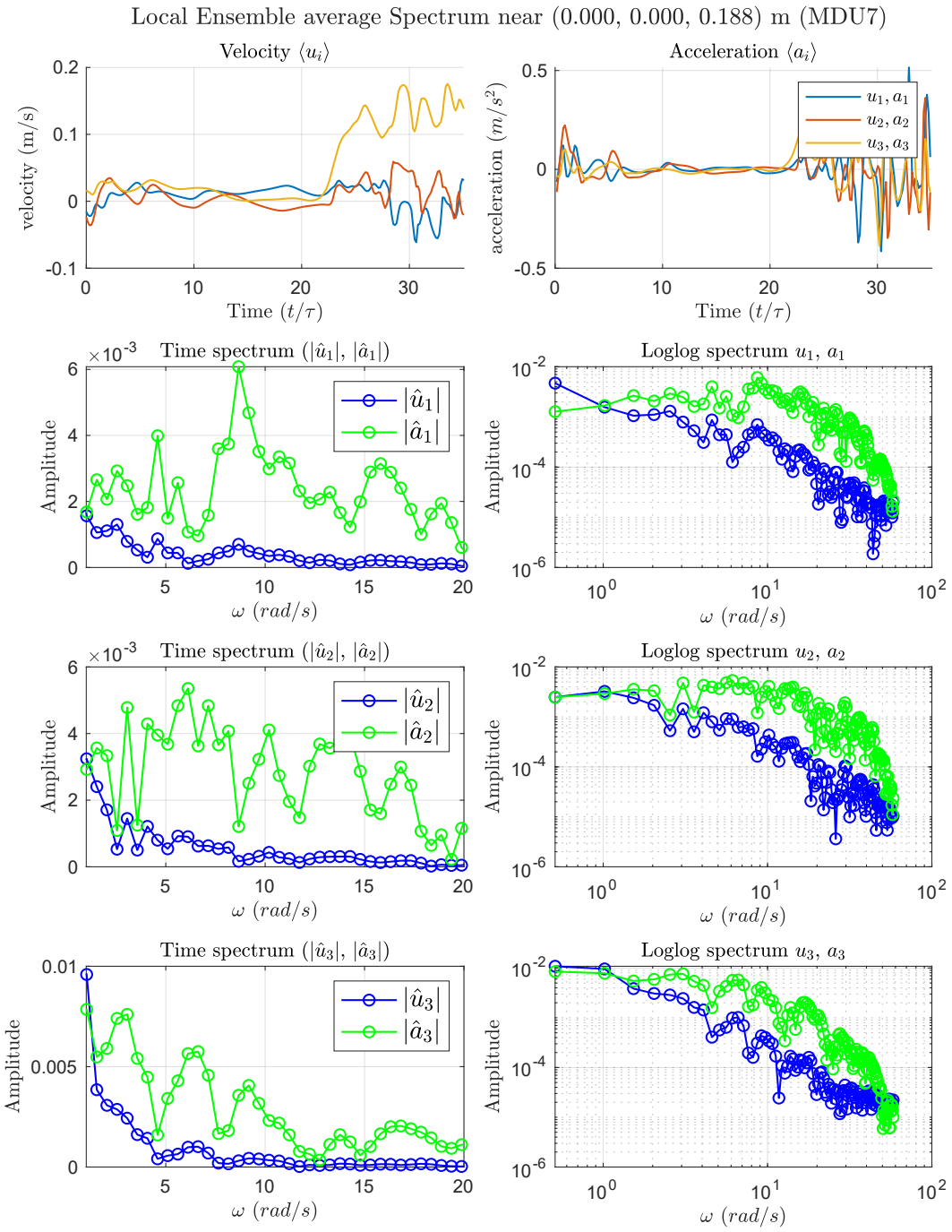

Figure 3.28: Temporal spectra of velocity and acceleration at $z \simeq 0.2$ m for the unstably stratified case (MDU7). No peak at $\omega \simeq 1$ rad s^{-1} is observed; energy spreads over a wide frequency range due to active convection.

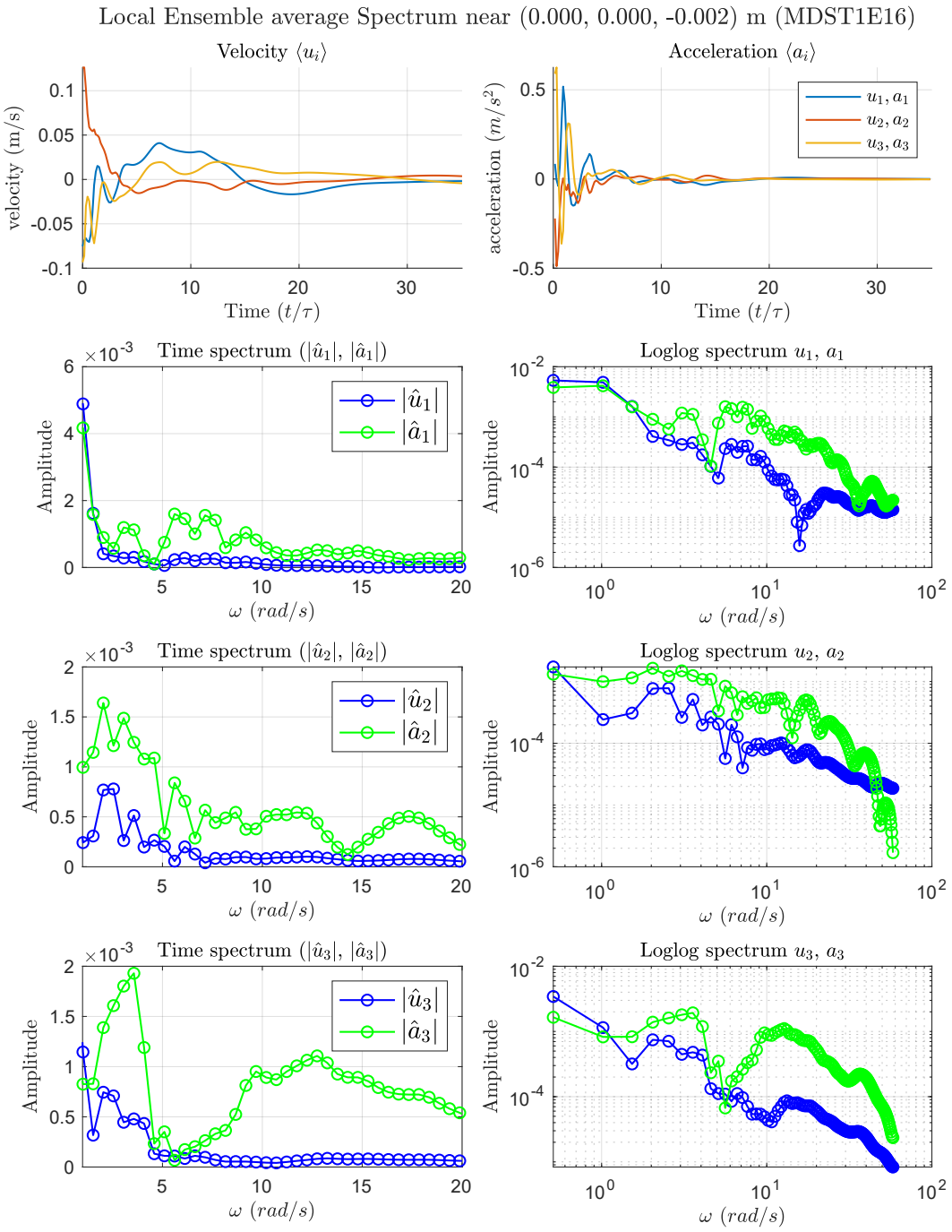

Figure 3.29: Temporal spectra of velocity and acceleration at $z \simeq 0$ m for the weakly stratified stable case (MDST1E16). No distinct peak appears near $\omega \simeq \mathcal{N}$; energy is irregularly distributed over intermediate frequencies, indicating weak wave activity and suppressed small-scale turbulence.

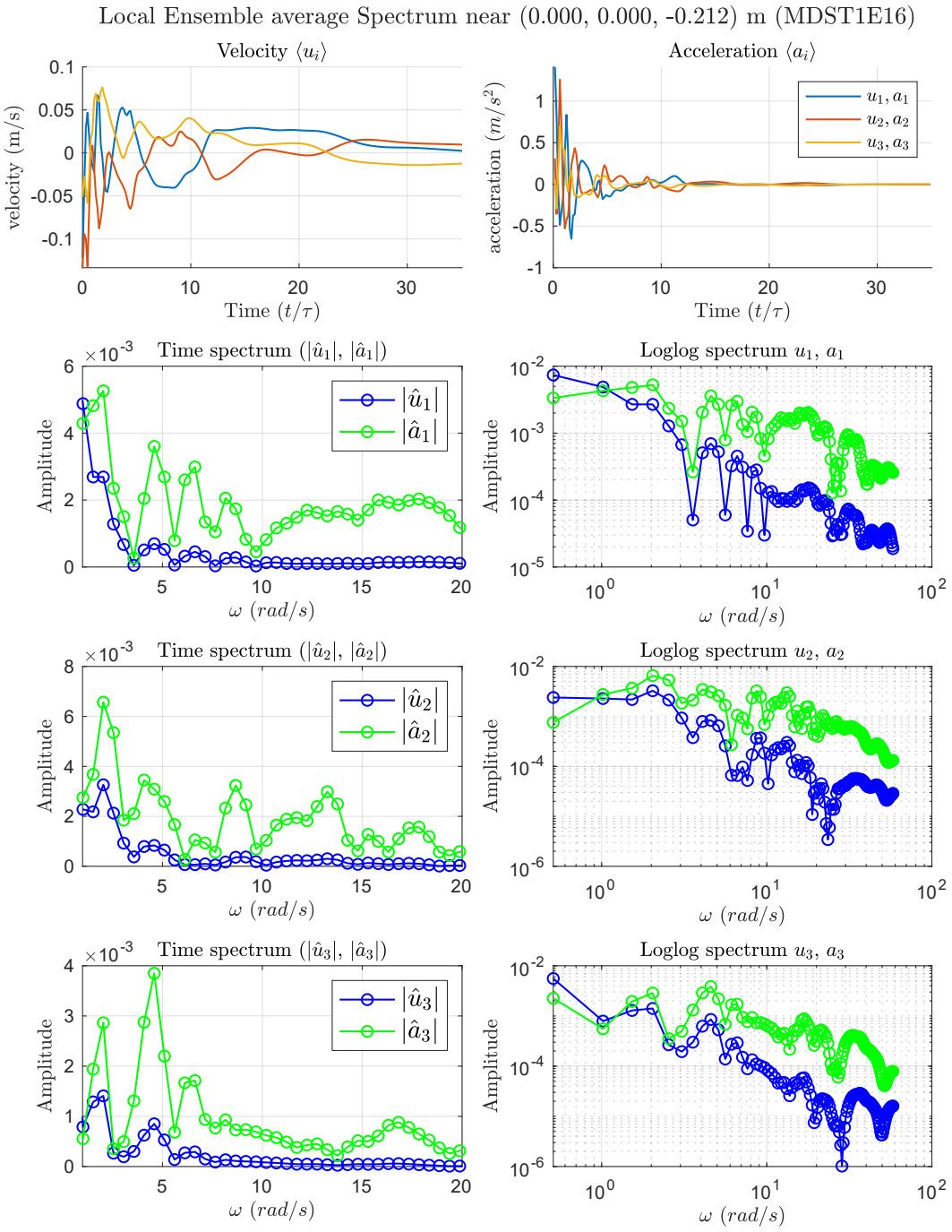

Figure 3.30: Temporal spectra of velocity and acceleration at $z \simeq -0.21$ m (cloudy region) for the weakly stratified stable case (MDST1E16). The spectra show no coherent oscillatory peak and limited energy at high frequencies, consistent with weak but stabilizing stratification preventing the formation of small-scale motions.

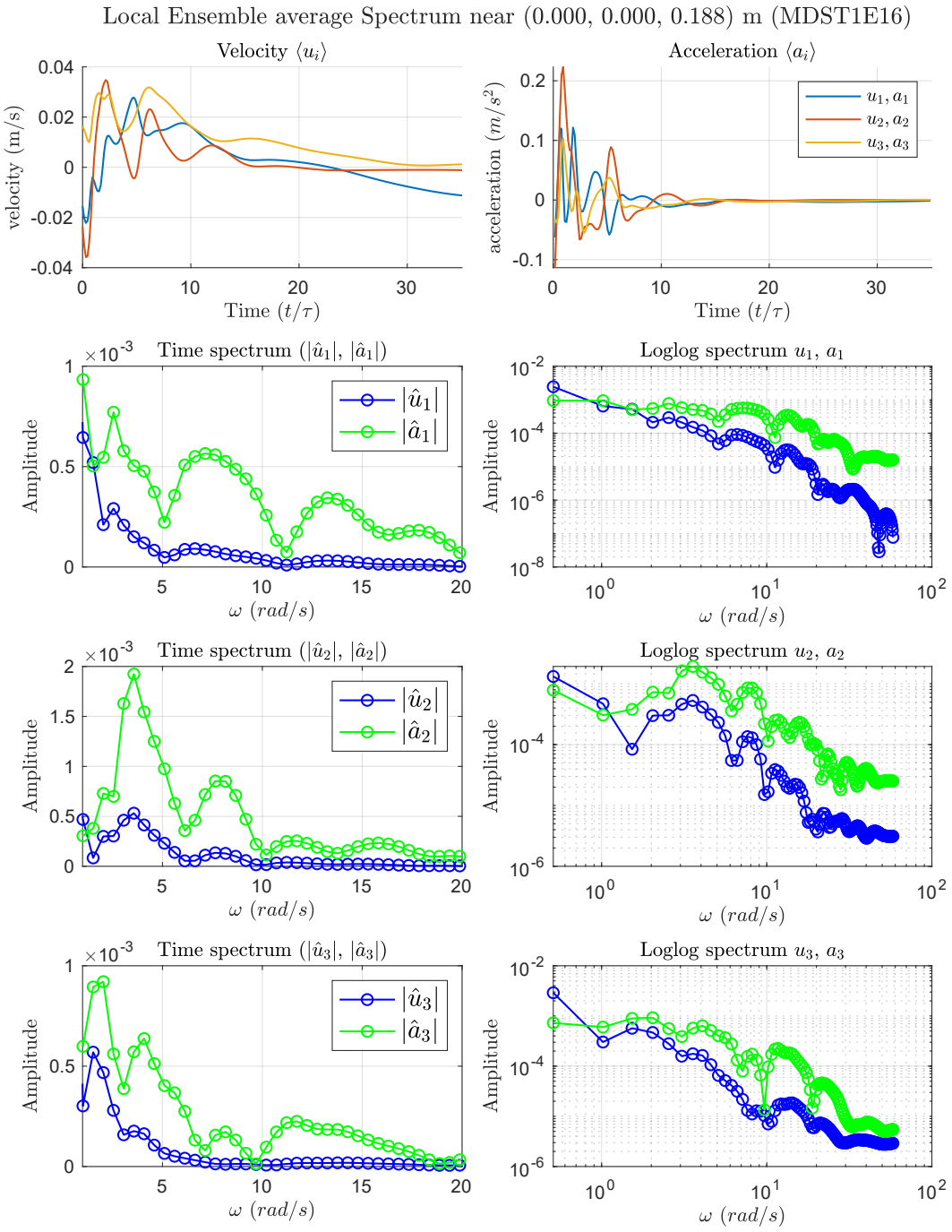

Figure 3.31: Temporal spectra of velocity and acceleration at $z \simeq 0.19$ m (clear-air region) for the weakly stratified stable case (MDST1E16). No peak near $\omega \simeq \mathcal{N}$ is visible; the overall spectral energy remains low and irregular, suggesting that stability inhibits both wave activity and high-frequency turbulent fluctuations.

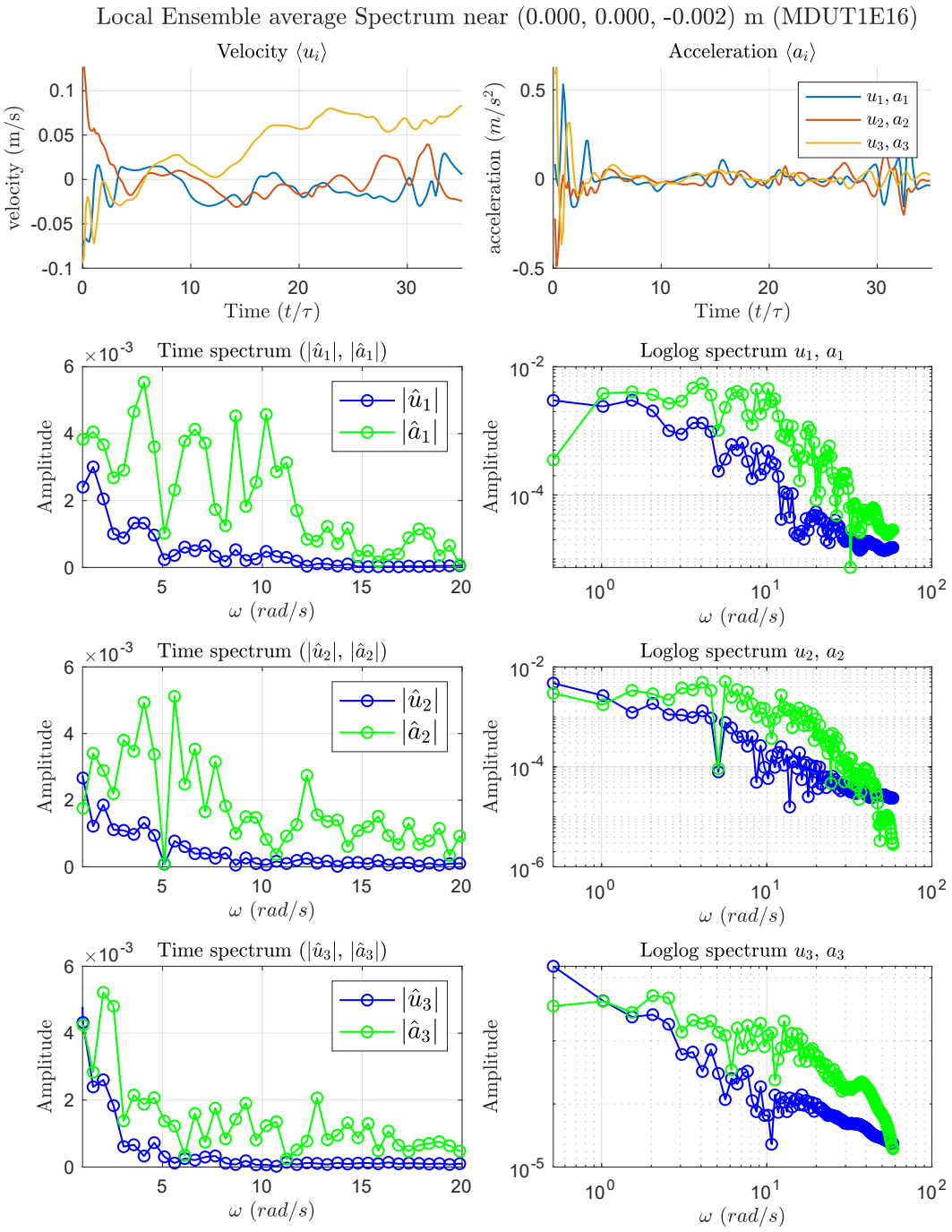

Figure 3.32: Temporal spectra of velocity and acceleration at $z \simeq 0$ m for the unstably stratified case (MDUT1E16). No coherent peak is observed, and the energy is distributed in an irregular, fragmented pattern across frequencies, reflecting non-stationary convective dynamics similar to but weaker than those in MDU7.

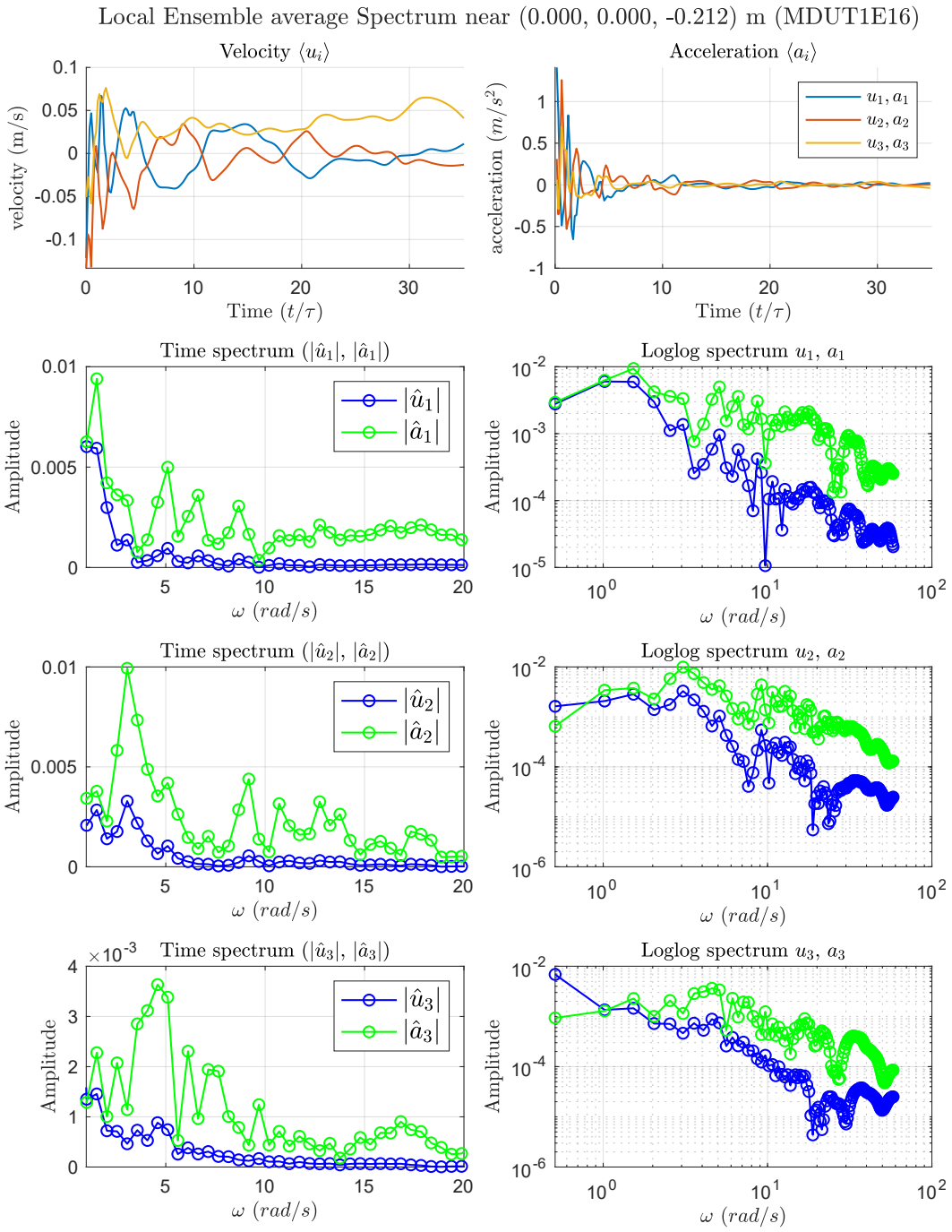

Figure 3.33: Temporal spectra of velocity and acceleration at $z \simeq -0.21$ m (cloudy region) for the unstably stratified case (MDUT1E16). Spectra exhibit scattered and irregular peaks with no identifiable oscillatory frequency, indicating intermittent convective bursts rather than a fully developed turbulent regime.

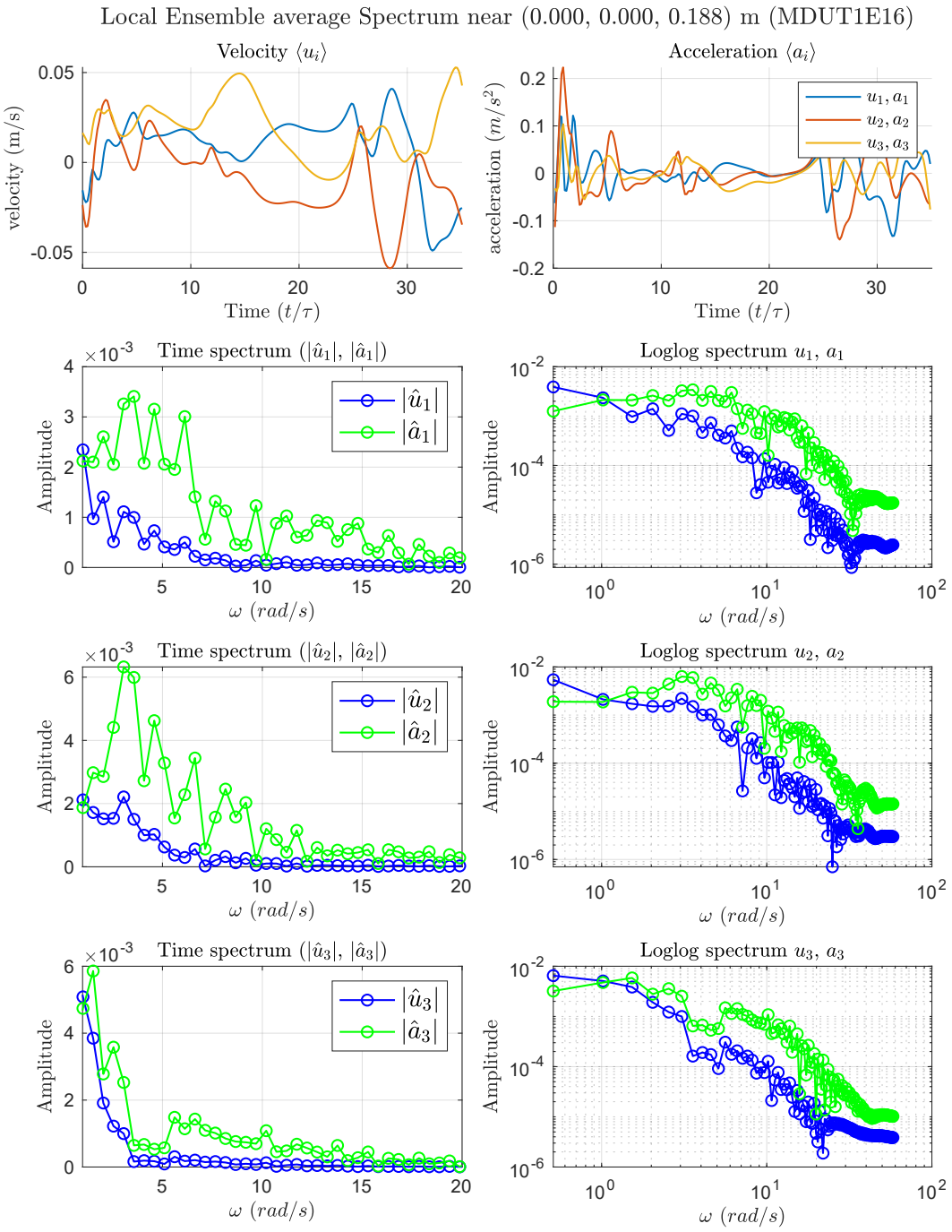

Figure 3.34: Temporal spectra of velocity and acceleration at $z \simeq 0.19$ m (clear-air region) for the unstably stratified case (MDUT1E16). The spectra remain highly irregular and non-continuous, suggesting that convective activity is intermittent and spatially localized, without the emergence of persistent oscillations or steady turbulence.

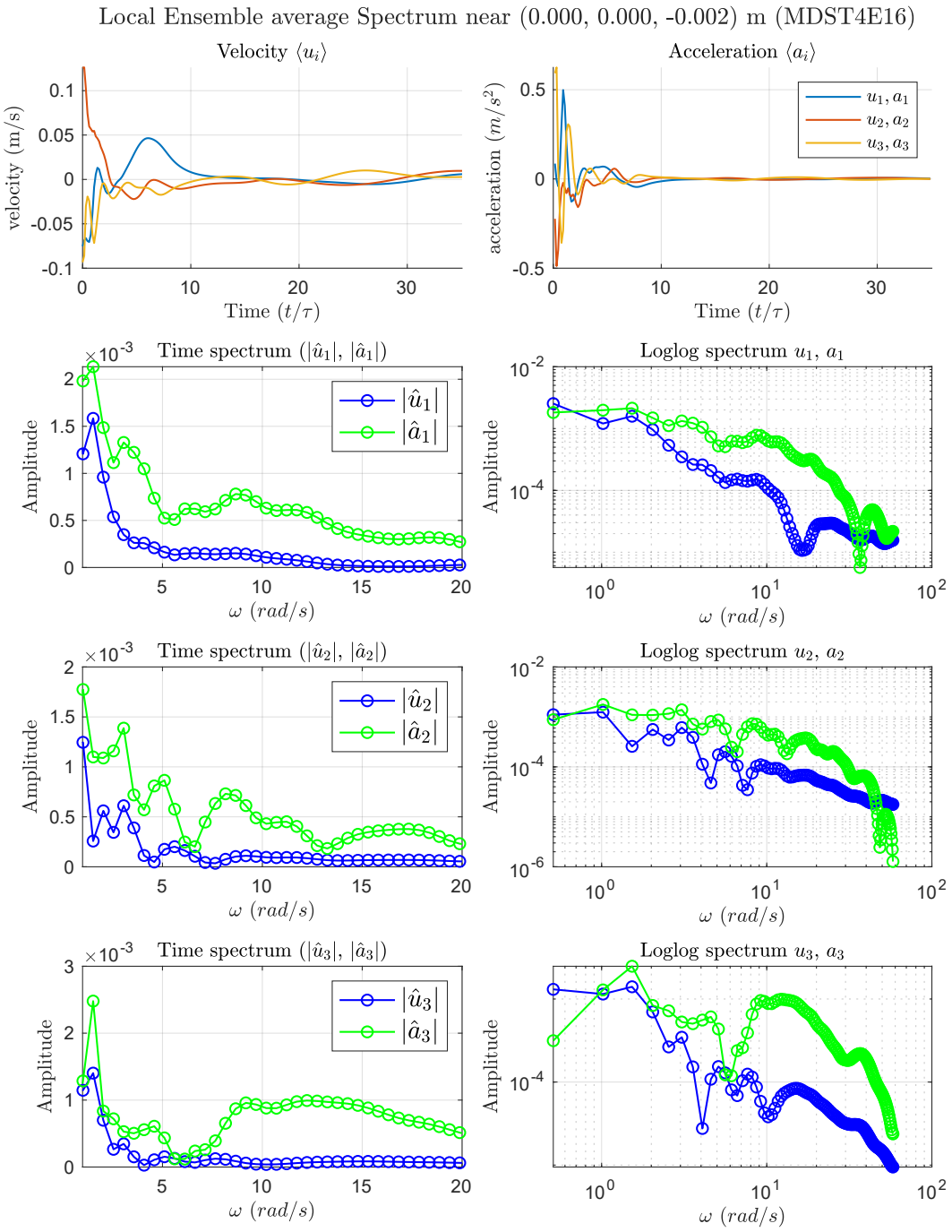

Figure 3.35: Temporal spectra of velocity and acceleration at $z \simeq 0$ m for the highly stable case (MDST4E16). A pronounced peak occurs at $\omega \simeq \mathcal{N}$, indicating internal-wave dynamics strongly confined to the stratified interface and suppression of high-frequency fluctuations.

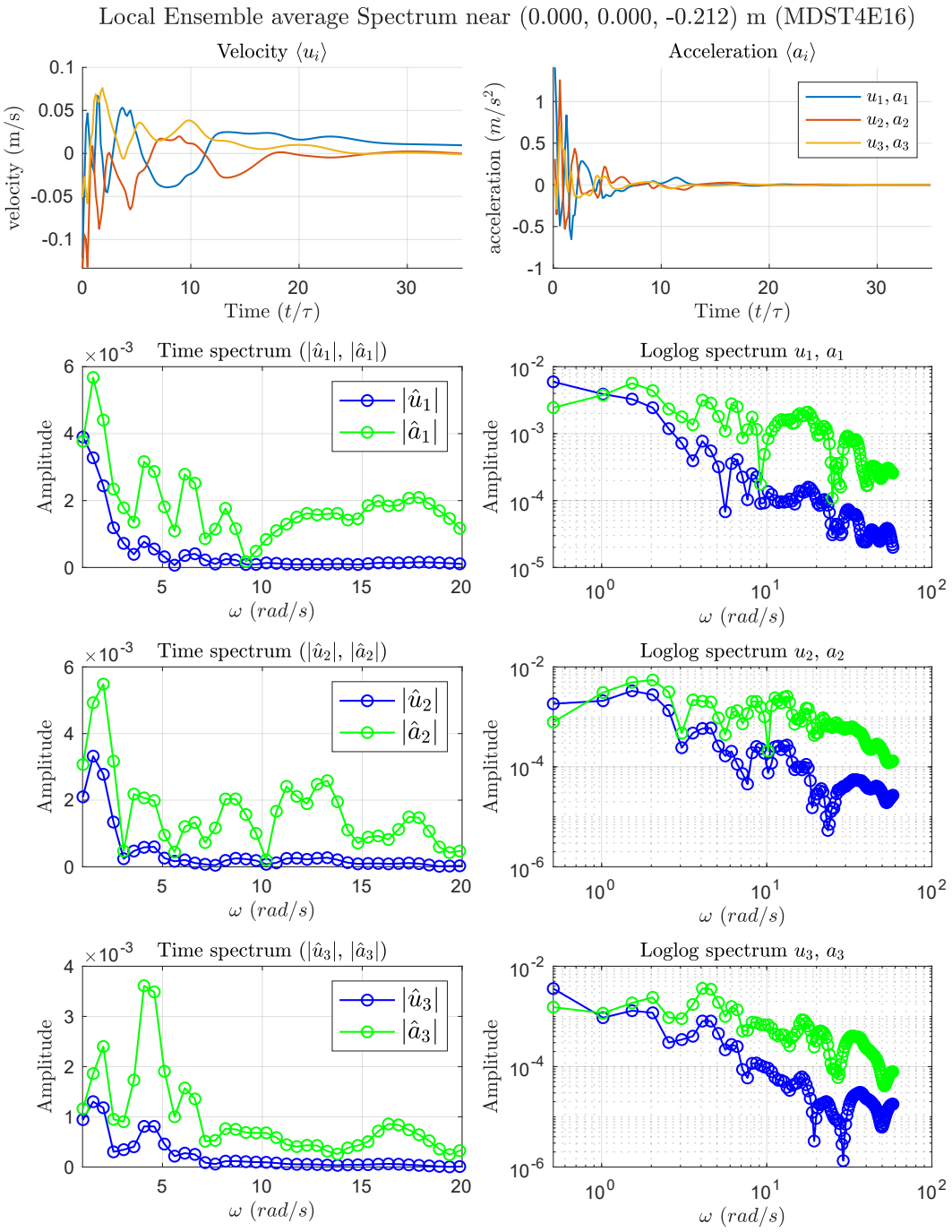

Figure 3.36: Temporal spectra of velocity and acceleration at $z \simeq -0.21$ m (cloudy region) for the highly stable case (MDST4E16). The oscillatory peak is significantly reduced compared to the interface, showing that the strong stratification confines wave energy and inhibits small-scale turbulence below the interface.

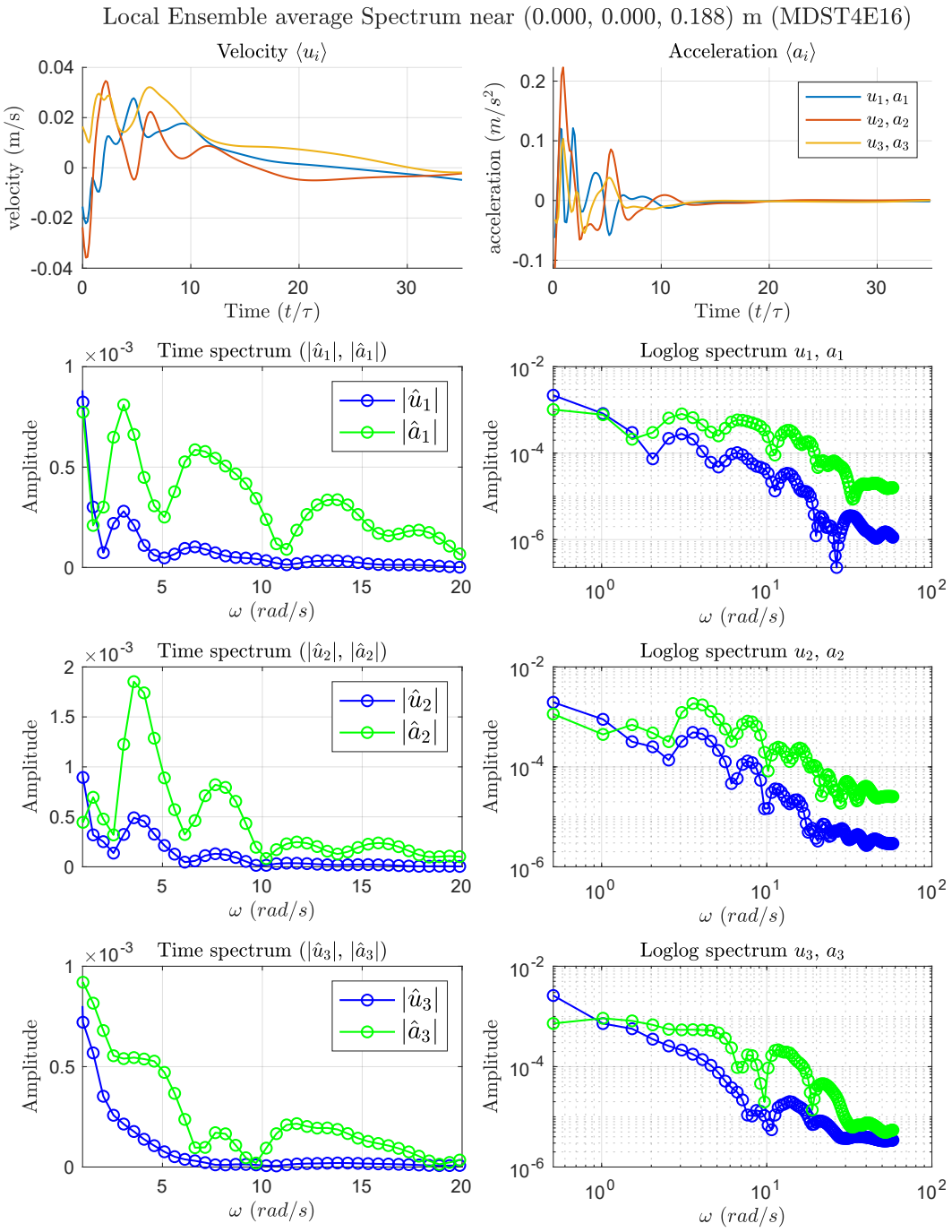

Figure 3.37: Temporal spectra of velocity and acceleration at $z \simeq 0.19$ m (clear-air region) for the highly stable case (MDST4E16). Only a weak oscillatory signature remains, indicating limited upward transmission of internal-wave energy and very strong suppression of turbulent fluctuations above the interface.

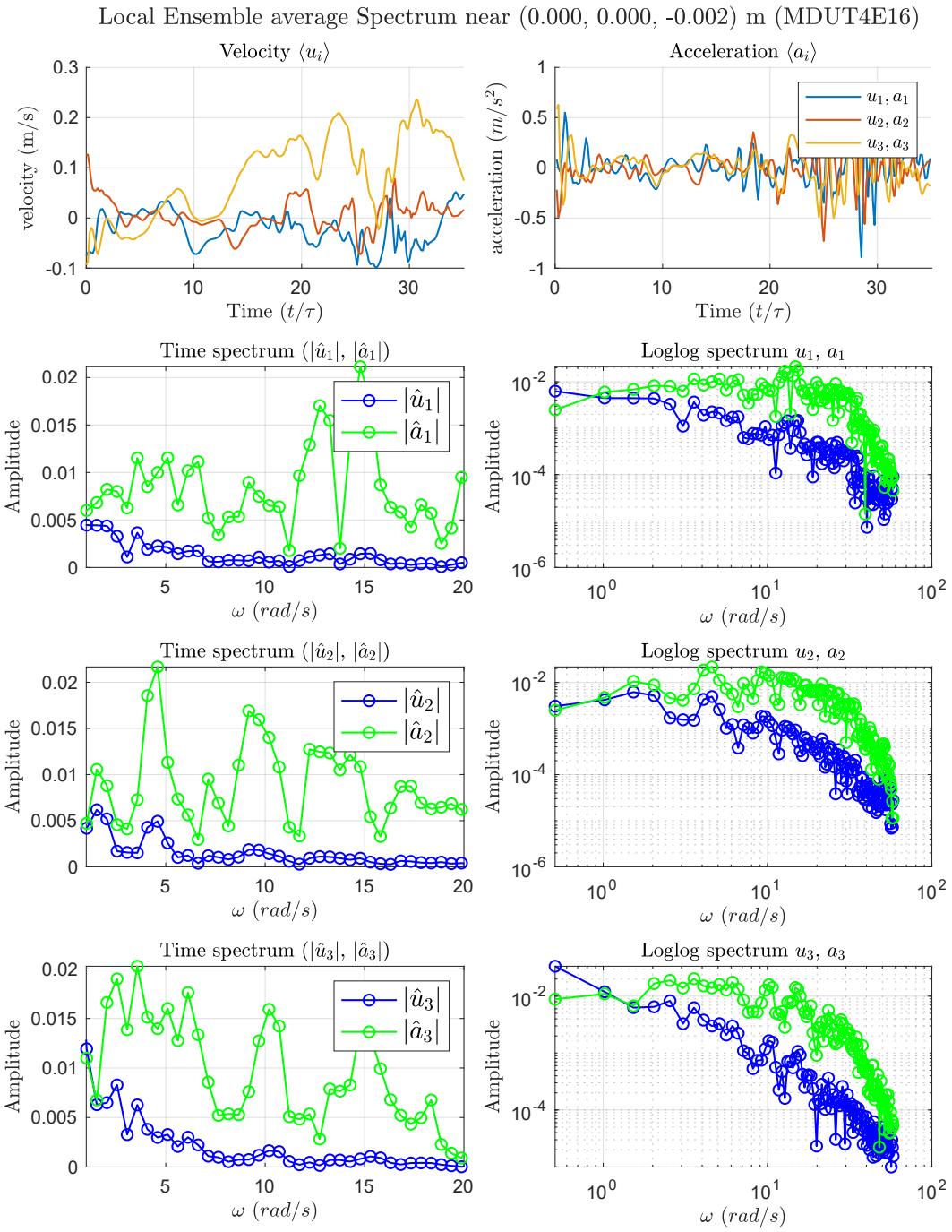

Figure 3.38: Temporal spectra of velocity and acceleration at $z \simeq 0$ m for the highly unstable case (MDUT4E16). Energy is strongly distributed toward intermediate and high frequencies, with no peak in the $\mathcal{N}$ range, reflecting intense and fully non-stationary convective motions.

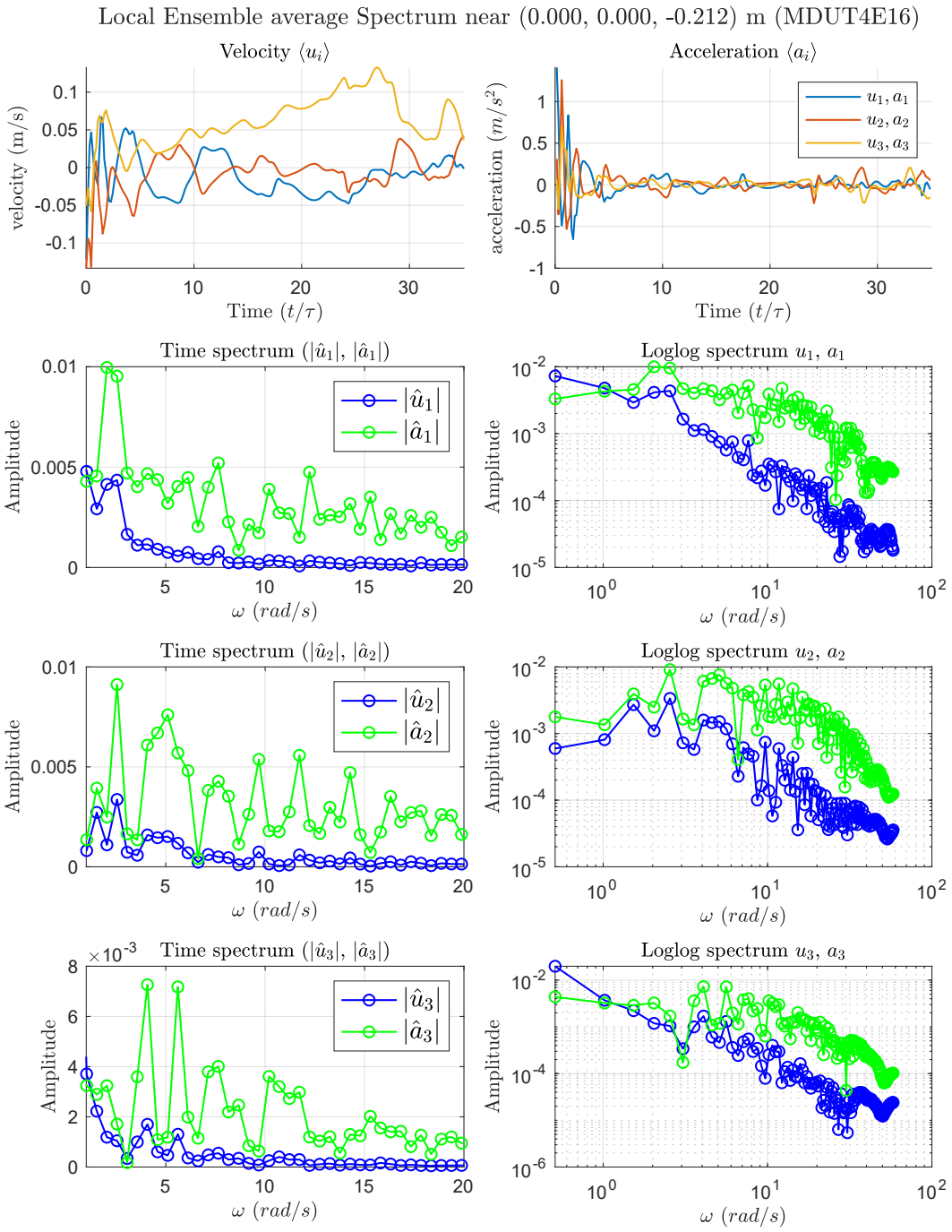

Figure 3.39: Temporal spectra at $z \simeq -0.21$ m (cloudy region) for the highly unstable case (MDUT4E16). The fragmented spectral structure indicates intermittent convective bursts dominating the temporal dynamics, without any coherent oscillatory mode.

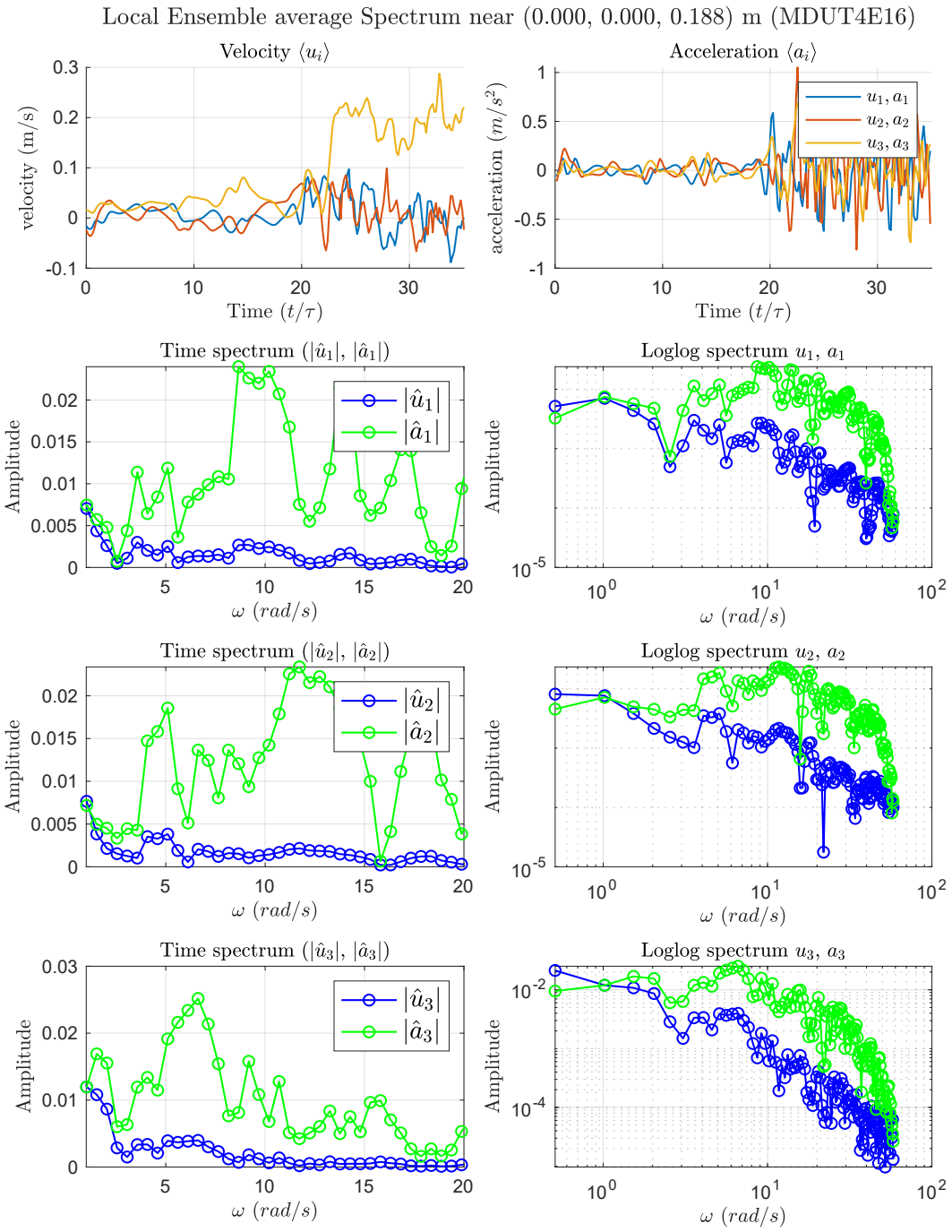

Figure 3.40: Temporal spectra at $z \simeq 0.19$ m (clear-air region) for the highly unstable case (MDUT4E16). The spectra remain irregular and dominated by high-frequency components, showing the absence of stratified constraints and the persistence of vigorous turbulence.

Temporal spectra for the weakly stratified cases (MDST1E16, MDUT1E16). At all three heights (cloudy, interface, and clear-air), the temporal spectra do not exhibit a distinct peak near the buoyancy range $\mathcal{N} \in [0.5, 1]$ rad s^{-1}. Instead, energy is spread over broader frequency bands and extends toward higher ω, indicating that turbulence dominates over narrow-band oscillatory motions. This behaviour is consistent with (i) a comparatively weak stratification ($\mathcal{N}^2 \in [0.25, 1]$), which reduces the restoring force and the wave signature; (ii) the finite record length, which sets the spectral resolution $\Delta\omega \simeq 2\pi/T_{\max}$ and limits the ability to isolate a sharp peak near $\mathcal{N}$; and (iii) the use of a taper (Hamming) that mitigates leakage at the cost of broadening spectral lobes. Although the stratification is weak, it remains stably configured and therefore inhibits the generation of small-scale turbulent motions, preventing the full development of high-frequency fluctuations. Overall, the spectra suggest that any internal-wave activity, if present, is masked by irregular turbulent fluctuations, while the acceleration spectra further emphasize the high-ω content through the relation $\hat{a}(\omega) = i\,\omega\,\hat{u}(\omega)$.

Similarly to the strongly unstable configuration (MDU7), the spectra for MDUT1E16 show no evidence of coherent oscillatory peaks in the frequency range where internal waves would typically appear in stable conditions. At all three vertical positions, the spectral energy is distributed in an irregular and fragmented fashion, with scattered and intermittent peaks extending up to $\omega \sim$ 10–20 rad s^{-1}. However, compared to MDU7, the spectral features are less energetic and more chaotic, indicating a weaker yet more temporally irregular convective activity. This behaviour reflects a regime in which unstable stratification ($\mathcal{N}^2 < 0$) still drives vertical overturning, but without establishing persistent large-scale structures or statistically stationary turbulence. The flow therefore remains dominated by non-linear, transient convective bursts, whose episodic nature produces fragmented spectral distributions rather than a continuous broadband shape. Acceleration spectra further emphasize this behaviour, exhibiting enhanced but sporadic high-frequency amplitudes associated with localized plume dynamics.

Temporal spectra for the strongly stratified cases (MDST4E16,MDUT4E16). The temporal spectra for MDST4E16 exhibit a clear oscillatory signature only in the vicinity of the stratified interface. At the interface height ($z \simeq 0$ m), a sharp peak appears around $\omega \simeq$ 1–1.2 rad s^{-1}, which is consistent with the local buoyancy frequency. Indeed, $\mathcal{N}$ evolves in time: it starts from relatively high values, $\mathcal{N}(t = 0) \simeq \sqrt{3.6} \approx$ 1.9 rad s^{-1}, and progressively relaxes towards $\mathcal{N}(t \to \text{end}) \simeq \sqrt{1.1} \approx 1.05$ rad s^{-1}. Away from the interface, however, the peak rapidly weakens and becomes barely detectable in both the cloudy ($z \simeq -0.21$ m) and clear-air ($z \simeq 0.19$ m) regions. Unlike the moderately stable case MDS7, where internal-wave energy still reaches the upper layer, here the oscillatory dynamics appear strongly confined near the region of maximum stratification. This behaviour may be associated with (i) the stronger

stability ($\Delta T = 4$ K instead of 2 K), which enhances the local restoring force and thus the confinement of internal gravity waves to the density gradient, and (ii) the larger initial energy contrast between cloud and air (16 instead of 7). At higher frequencies, the spectral energy decays steeply at all heights, with negligible acceleration content. Overall, MDST4E16 represents a strongly wave-dominated and locally confined regime, in which stable stratification very effectively limits vertical motion and prevents both the development of small-scale turbulence and the propagation of internal-wave energy across the domain. In the highly unstable configuration MDUT4E16, the temporal spectra at all three heights exhibit significantly stronger energy levels than in the other unstable runs. The spectral distribution is heavily biased toward intermediate and high frequencies ($\omega \gtrsim 10$ rad s^{-1}), with pronounced and irregular fluctuations, reflecting the presence of vigorous convective motions and rapid small-scale dynamics. Compared with MDUT1E16 and MDU7, the intensification of unstable stratification leads to more energetic and persistent high-ω contributions, especially in the acceleration spectra. The resulting temporal behaviour indicates a strongly turbulent and highly non-stationary regime, in which intense convective bursts dominate the dynamics throughout the domain.

The temporal spectra discussed above reveal a clear sensitivity of the flow dynamics to the degree and sign of stratification. In the strongly and moderately stable cases (MDST4E16, MDS7), energy remains confined to low frequencies, with a marked signature of oscillations near $\mathcal{N}$ in regions directly influenced by the Temperature gradient. Such wave-dominated behaviour corresponds to weak or absent small-scale turbulence and a progressive localisation of motion around the interface as stability increases. Conversely, unstable configurations (MDU7, MDUT1E16, MDUT4E16) exhibit a substantial redistribution of energy toward intermediate and high frequencies, indicating the growth of intense convective activity. The most unstable case (MDUT4E16) generates highly irregular spectra with persistent high–ω contributions, highlighting the dominance of non-linear overturning motions and the fully turbulent nature of the flow. While standard Fourier analysis in time provides insight into the global frequency content of the signals, it cannot capture their markedly non-stationary character. The temporal signatures of these flows are continuously evolving: oscillatory motions strengthen or fade depending on local stratification, and convective bursts appear intermittently with different intensities. A representation that retains both temporal localisation and frequency resolution is therefore required to better distinguish between transient oscillatory phases and vigorously turbulent episodes. To this end, we now quantify how the distribution of energy over frequencies changes over time by computing spectrograms of acceleration at the same fixed locations. This time–frequency analysis allows us to track the activation of different temporal scales during the decay and to assess more precisely the interplay between wave-like and convective dynamics in stably and unstably stratified regimes, at the price of the usual

frequency broadening in $\Delta\omega$ that accompanies improved temporal localisation.

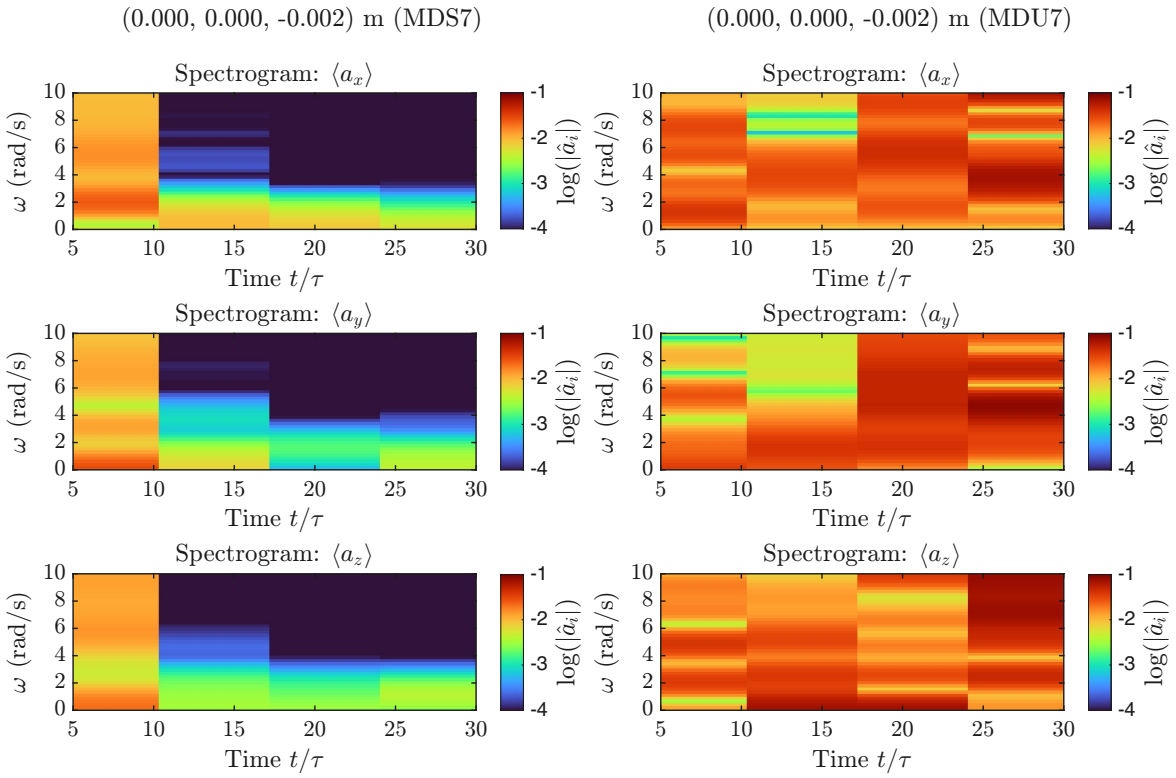

Figure 3.41: Spectrograms of acceleration at the interface ($z \simeq 0$ m) for the moderately stable case (MDS7, left) and the strongly unstable case (MDU7, right).

Figures 3.41–3.43 show the spectrograms of the acceleration field at the interface location. A clear distinction emerges between stable and unstable stratification. Under stable conditions, most of the energy remains concentrated at low frequencies and gradually decays over time. The moderate stability case (MDS7) preserves a broader spectral support for longer, indicating the persistence of internal–wave activity before progressive damping takes place. When stability weakens (MDST1E16), the spectral energy becomes more diffuse and irregular, as turbulence more effectively disrupts the oscillatory signature. In the highly stable configuration (MDST4E16), fluctuations rapidly lose intensity and remain strongly confined to the low–frequency band, consistent with wave trapping near the interface. In contrast, all unstable configurations display a sustained broadening of frequency support. Buoyancy–driven overturning injects energy into a wide range of temporal scales, resulting in persistent activity especially at intermediate and high frequencies. The degree of instability governs the level of intermittency: while MDUT1E16 shows episodic bursts of fast accelerations, the most unstable case (MDUT4E16) maintains highly non-stationary dynamics across the whole simulation, with vigorous fluctuations and continuously active small-scale motions. Overall, the interface spectrograms clearly illustrate a transition from wave-controlled motion in stable regimes to strongly turbulent convective dynamics when stratification becomes unstable.

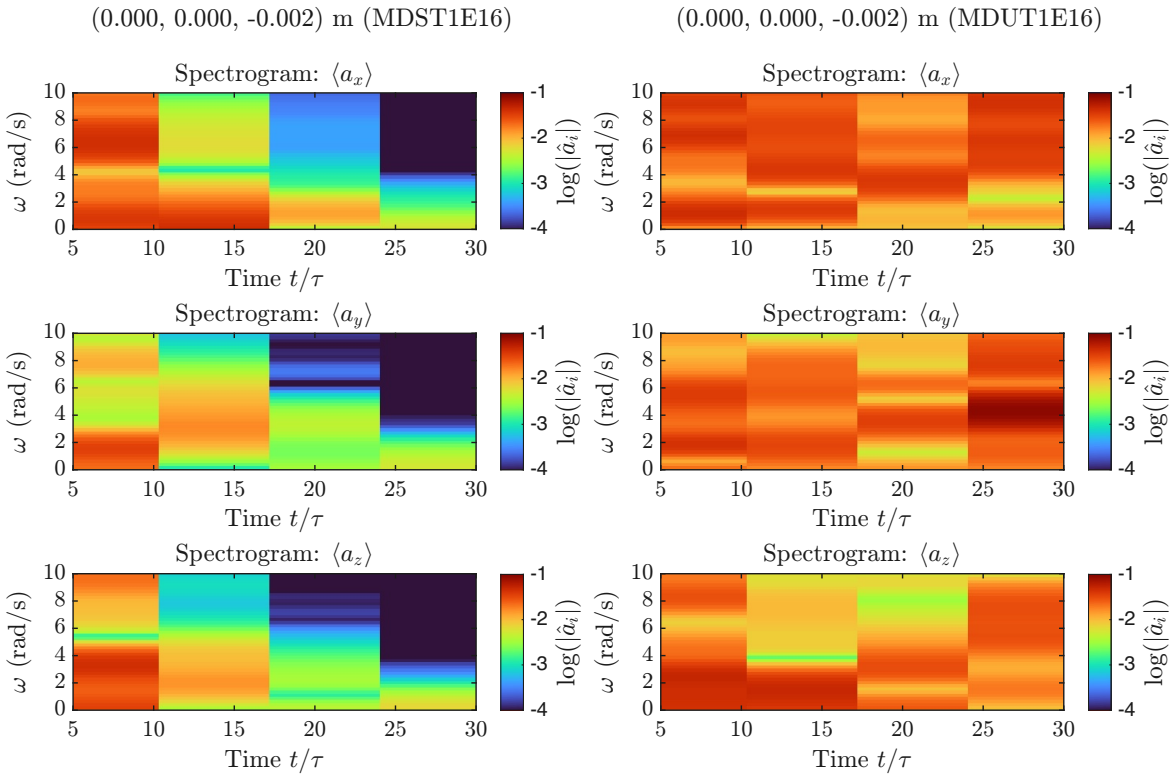

Figure 3.42: Same as Fig. 3.41, but for the weakly stable case (MDST1E16, left) and the weakly unstable case (MDUT1E16, right).

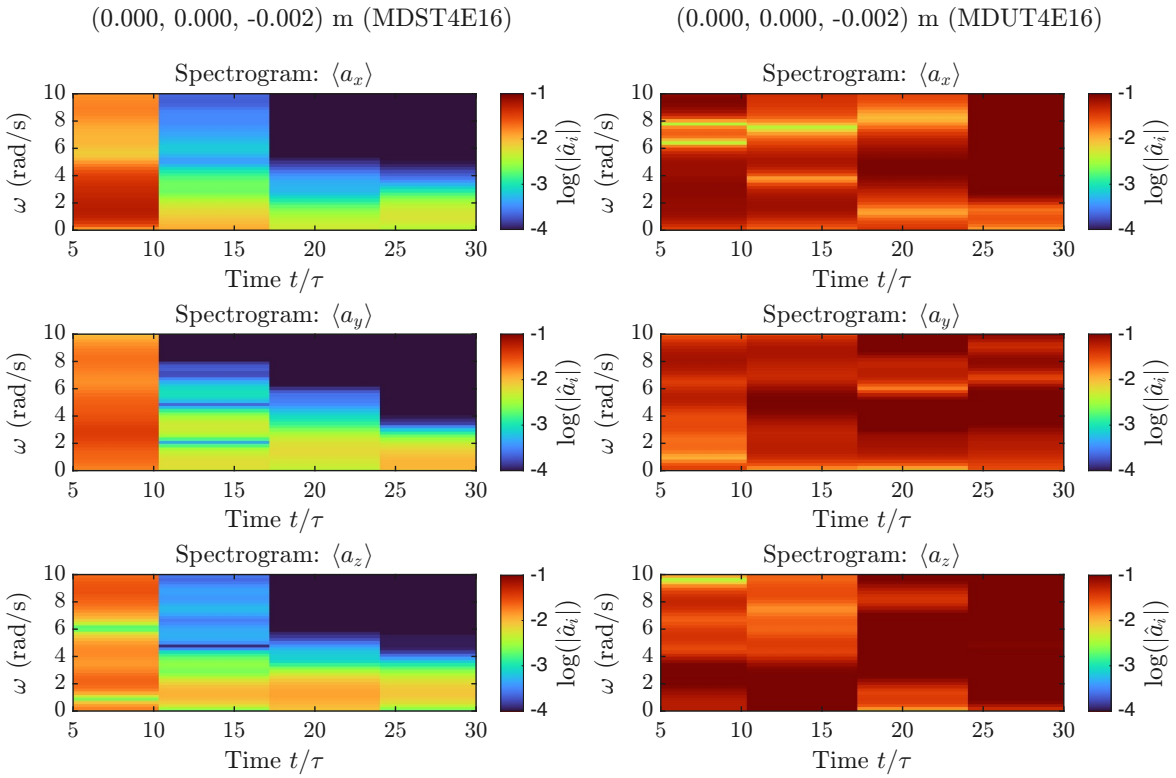

Figure 3.43: Same as above, but for the highly stable (MDST4E16, left) and highly unstable (MDUT4E16, right) regimes.

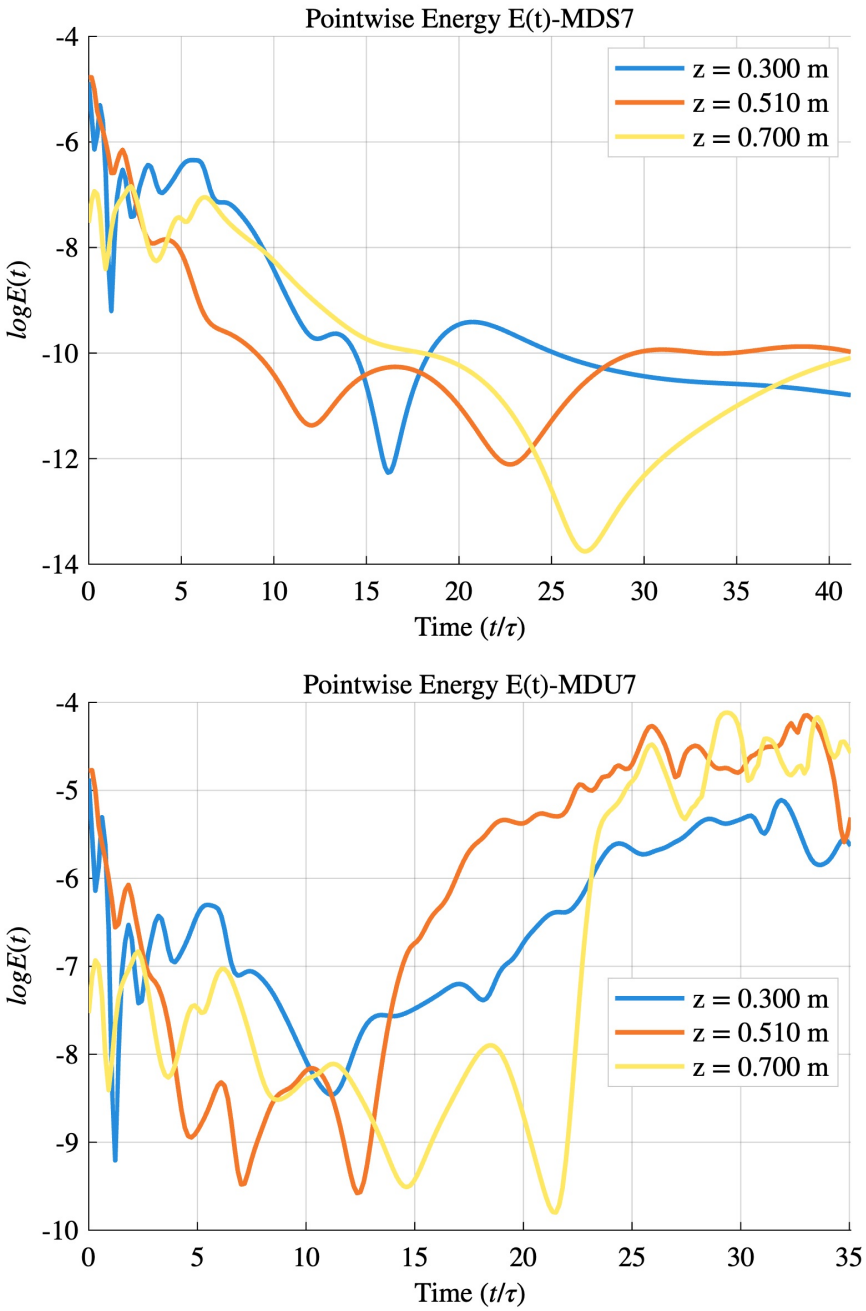

Figure 3.44: Temporal evolution of the TKE at three fixed spatial points with different z-coordinates. The blue curve corresponds to a point inside the cloud region, the red curve to the cloud–clear-air interface, and the yellow curve to the clear-air region. Results are shown for simulations MDS7 and MDU7.

As a complement to the pointwise analysis, we examine the temporal evolution of TKE at three fixed vertical positions: inside the cloud (blue curve), at the cloud–clear-air interface (red curve), and in the clear-air region (yellow curve). Figures 3.44, 3.45, and 3.46 show these trends for the MDS7–MDU7, MDST1E16–MDUT1E16, and MDST4E16–MDUT4E16 simulation pairs, respectively.

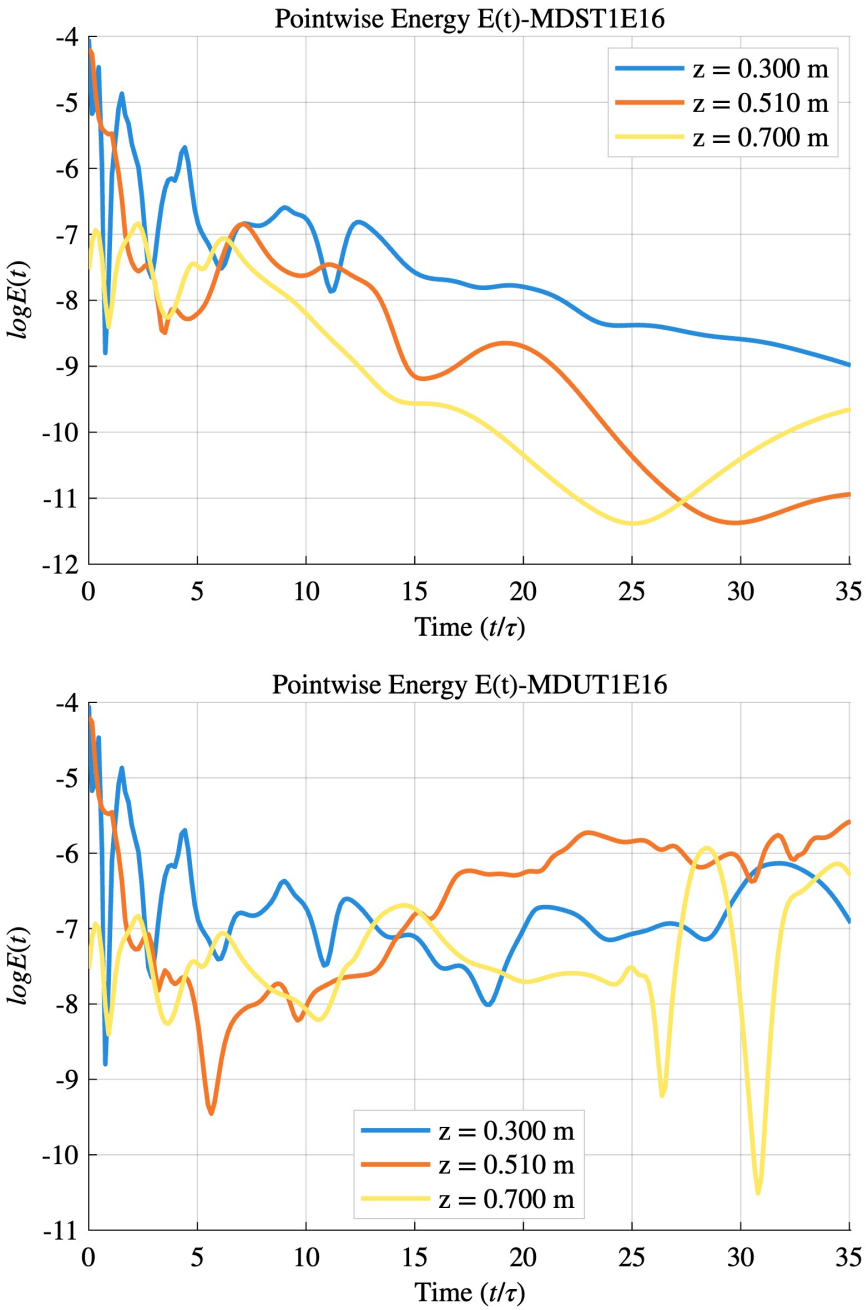

Figure 3.45: Temporal evolution of the TKE at three fixed spatial points with different z-coordinates. The blue curve corresponds to a point inside the cloud region, the red curve to the cloud–clear-air interface, and the yellow curve to the clear-air region. Results are shown for simulations MDST1E16 and MDUT1E16.

Starting from Fig. 3.44, we observe a clear divergence between the stable (MDS7) and unstable (MDU7) cases, particularly at the interface. The red curves separate after approximately $5\,t/\tau_0$. In the stable case, after this divergence, two main energy drops occur—previously discussed in relation to stratification effects—followed by a mild recovery and a subsequent stabilization at values of order $\mathcal{O}(10^{-10})$. Conversely, the unstable configuration displays a pronounced growth beginning at about $12\,t/\tau_0$, eventually exceeding the initial TKE magnitude.

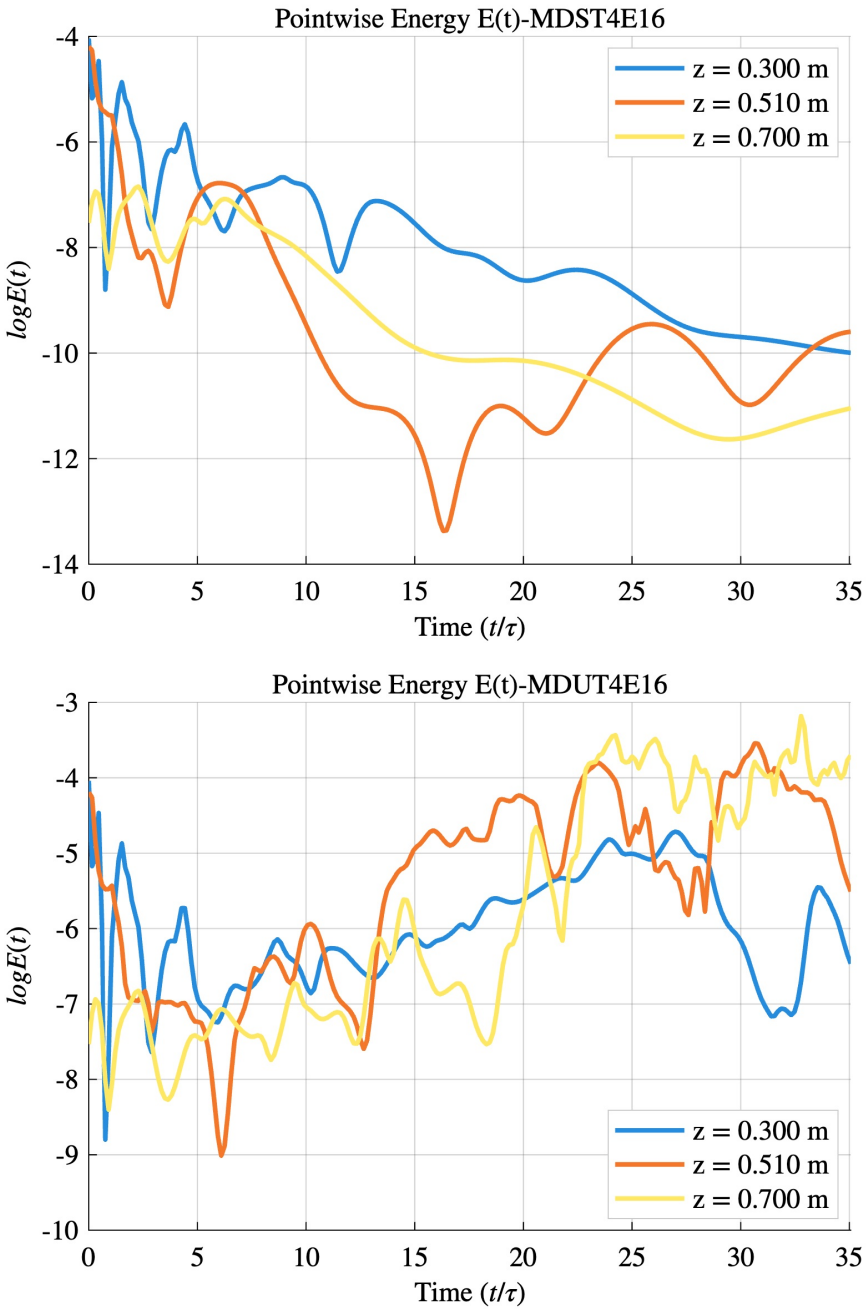

Figure 3.46: Temporal evolution of the TKE at three fixed spatial points with different z-coordinates. The blue curve corresponds to a point inside the cloud region, the red curve to the cloud–clear-air interface, and the yellow curve to the clear-air region. Results are shown for simulations MDST4E16 and MDUT4E16.

The other two locations qualitatively follow this behaviour, with differences related to their distance from the interface. The cloud-interior point (blue) responds later to stratification: the stable and unstable evolutions remain almost indistinguishable until $\sim 12\,t/\tau_0$, after which the curve gradually aligns with the interface trend but with reduced intensity. The clear-air point (yellow) shows the slowest response: deviations between stable and unstable cases appear only after $\sim 8\,t/\tau_0$, and the stratification-related features (energy decay in the stable case and energy growth in the unstable

one) emerge only beyond $20\,t/\tau_0$.

A similar interpretation applies to Fig. 3.45. Again, the interface curve exhibits good agreement between stable and unstable behaviours during the first $5\,t/\tau_0$. However, the decay here is noticeably steeper compared to the previous configuration, likely due to the higher initial TKE-to-stratification ratio. Moreover, because of the reduced temperature jump ΔT, stratification effects are less pronounced: both the energy pits and the late-time recovery/growth observed in the first case are significantly attenuated.

Finally, Fig. 3.46 reports the strongly stratified simulations. The behaviour changes substantially: the interface curves diverge as early as $\sim 3\,t/\tau_0$, showing that strong stratification accelerates the separation between stable and unstable dynamics. After an initially similar decay phase, the stable case exhibits a temporary TKE growth in place of the strong energy minimum observed previously at $\sim 6\,t/\tau_0$. Beyond this point, the two cases evolve in almost specular patterns: in the stable configuration the TKE resumes decaying, whereas in the unstable one it begins to rise. The stable case also presents a noticeable wavy pattern after reaching its minimum around $\sim 16\,t/\tau_0$, highlighting the onset of wave-dominated dynamics.

$\omega - k$ maps. The ω–k_z maps (Figs. 3.47–3.49) provide an empirical view of how spectral energy distributes across vertical wavenumbers and angular frequencies for selected horizontal modes $(k_x, k_y) = (1,1), (2,2), (3,3)$. They can be regarded as empirical dispersion diagrams, revealing how the flow redistributes energy between oscillatory and turbulent motions in the presence of stratification. A marked difference emerges between the stable (MDS) and unstable (MDU) configurations. In the stable cases, energy remains concentrated in a narrow band at low frequencies (typically below 1–2 rad/s, depending on the stratification), with only weak dependence on k_z. This indicates the prevalence of coherent oscillations—consistent with internal-wave dynamics—whose frequency is limited by the local Brunt–Väisälä value. The roughly horizontal energy contours in the (ω, k_z) plane suggest that the vertical structure of these motions is largely coherent rather than dispersive.

In contrast, the unstable runs display a broader and more irregular energy distribution, often tilted with respect to the ω axis. This oblique spreading reflects enhanced coupling between vertical and horizontal motions and a continuous redistribution of energy across both frequency and vertical wavenumber. Rather than a purely wave-to-turbulence transition, these patterns reveal a turbulent regime where remnants of wave-like activity coexist with vigorous convective fluctuations. The inclined energy ridges represent signatures of nonlinear wave–eddy interactions and vertical energy transfers typical of stratified turbulence.

Across all configurations, differences among the three velocity components are also evident. The horizontal components (u_1, u_2) generally carry higher energy and show broader support in k_z, while the vertical component (u_3) remains more confined and

significantly weaker at high k_z. This reflects both the restraining effect of stratification, which suppresses vertical motions, and the incompressibility constraint in spectral space,

$$k_x\hat{u}_1 + k_y\hat{u}_2 + k_z\hat{u}_3 = 0.$$

Hence, $\hat{u}_3$ must decrease as k_z increases if the horizontal components remain finite, producing a natural anisotropy in the energy distribution.

When comparing the different levels of stratification, further trends emerge:

- **Weakly stratified cases (MDST1E16, MDUT1E16):** Energy extends over a relatively broad frequency range in both stable and unstable configurations. The unstable run shows an early tendency toward vertical energy transfer, while the stable case retains low-frequency content consistent with weakly stratified wave motions.

- **Moderately stratified cases (MDS7, MDU7):** The difference between regimes becomes clearer. The stable configuration exhibits compact energy localized at low ω, whereas the unstable case presents a more diffuse cloud spanning a wider portion of the (ω, k_z) plane, reflecting the breakdown of vertical coherence and the onset of convective overturning. The oblique energy structures indicate strong nonlinear coupling between waves and turbulence.

- **Strongly stratified cases (MDST4E16, MDUT4E16):** The stable case displays very narrow low-frequency peaks around $\omega \simeq 1\,\mathrm{rad/s}$ and minimal high-frequency activity, consistent with internal-wave trapping. The unstable configuration, although more turbulent, still retains a faint low-frequency ridge, indicating that residual internal waves coexist within the turbulent background. These features highlight the persistence of stratification-induced coherence even under strong instability.

Figures 3.50–3.52 complement this picture by displaying the temporal evolution of selected Fourier modes. In the stable configurations, the amplitudes of all components oscillate around zero with nearly constant intensity, and higher-k_z modes decay faster, as expected from viscous damping and weaker coherence at small scales. In the unstable configurations, instead, low-k_z vertical modes, particularly $\hat{u}_3(k_x{=}1, k_y{=}1, k_z{=}0)$, exhibit a net growth in time. This large-scale mode corresponds to the initiation of convective overturning at the interface, which injects energy into a wide range of vertical scales. The logarithmic ω–k_z maps (Figs. 3.53–3.55) confirm that, while the most energetic peaks occur for $\omega \lesssim 2\,\mathrm{rad/s}$, significant energy also populates higher frequencies, especially in the unstable runs. This extended spectral support indicates that turbulence sustains a broad continuum of temporal scales rather than being dominated by a single oscillatory band. Overall, the gradual broadening of spectral

energy with increasing instability captures the coexistence and non-linear interaction of internal waves and turbulence within the evolving stratified layer.

In summary, the ω–k_z analysis reveals that stable runs are characterized by coherent, low-frequency oscillations with weak vertical dependence, while unstable runs exhibit broadband spectra and complex energy redistribution across scales. Increasing stratification enhances anisotropy and coherence, whereas instability promotes spectral broadening and non-linear coupling between waves and convective turbulence. These maps thus provide a compact and quantitative diagnostic of the interplay between stratification, instability, and turbulent dynamics in the flow.

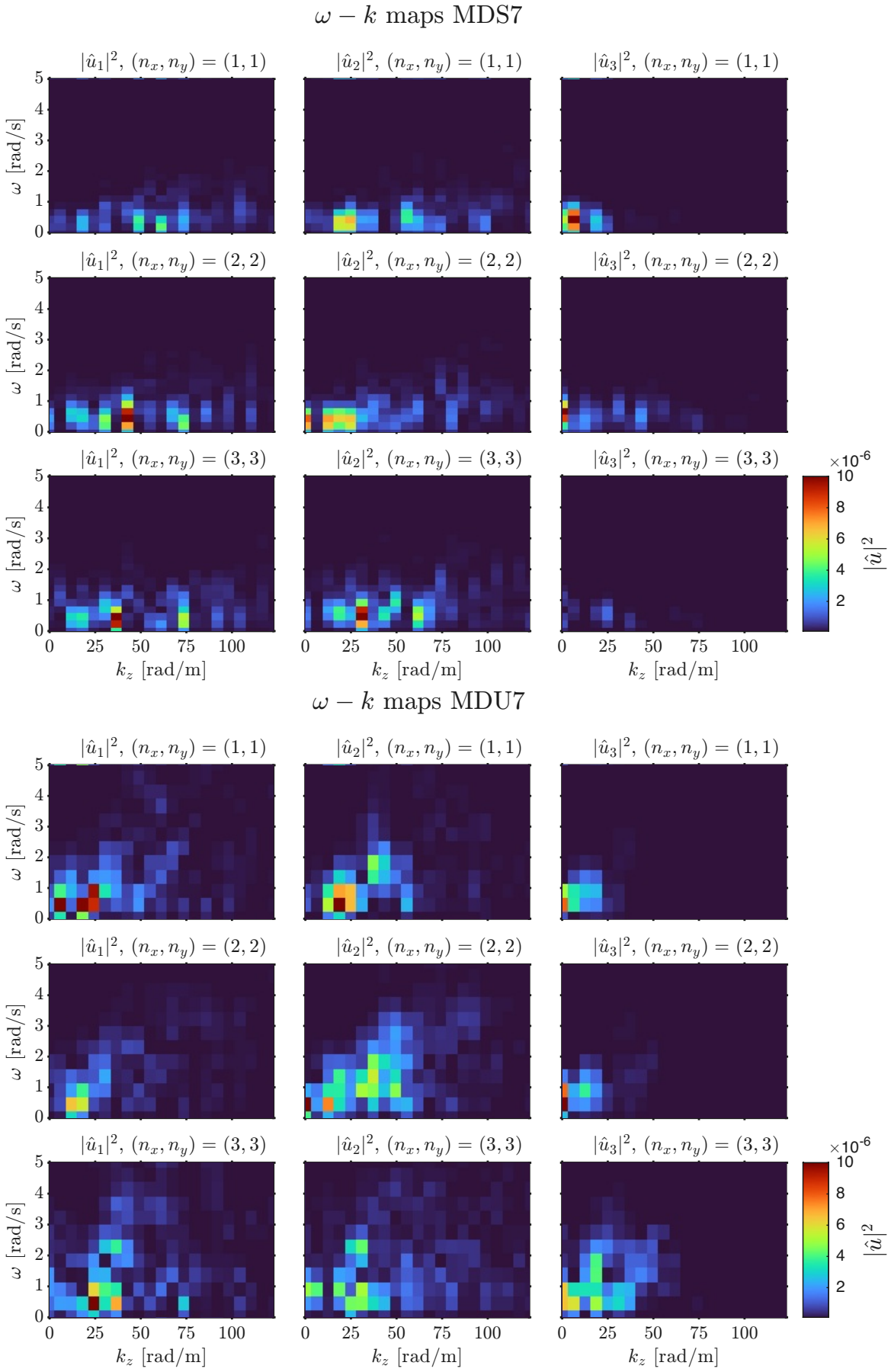

Figure 3.47: ω–k_z spectra for $(k_x, k_y) = (1,1), (2,2), (3,3)$. MDS7 shows wave–dominated energy at low k_z, whereas MDU7 exhibits broader turbulent excitation.

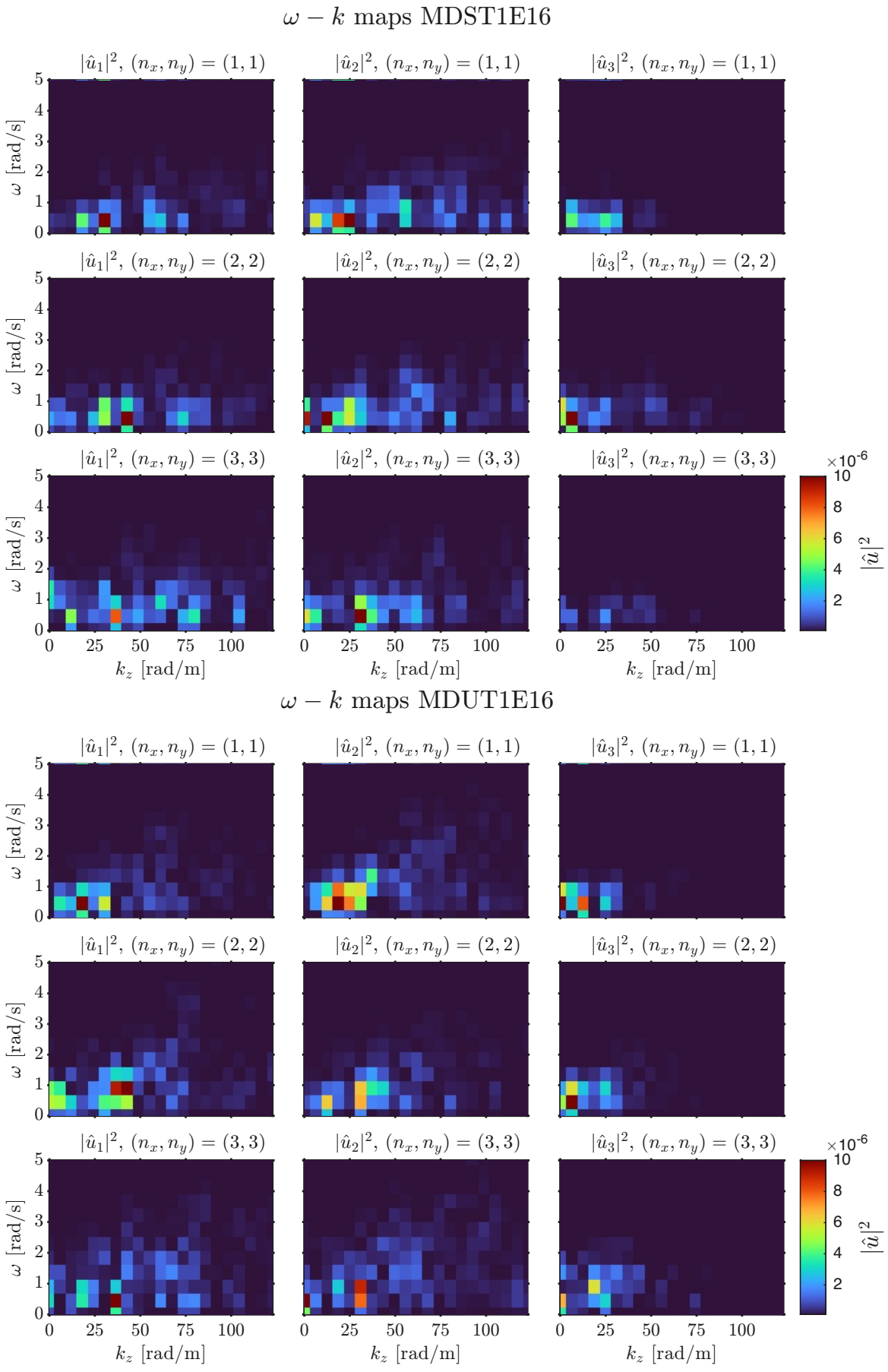

Figure 3.48: ω–k_z spectra for $(k_x, k_y) = (1,1), (2,2), (3,3)$. Weakly stratified cases MDST1E16 (top), MDUT1E16 (bottom).

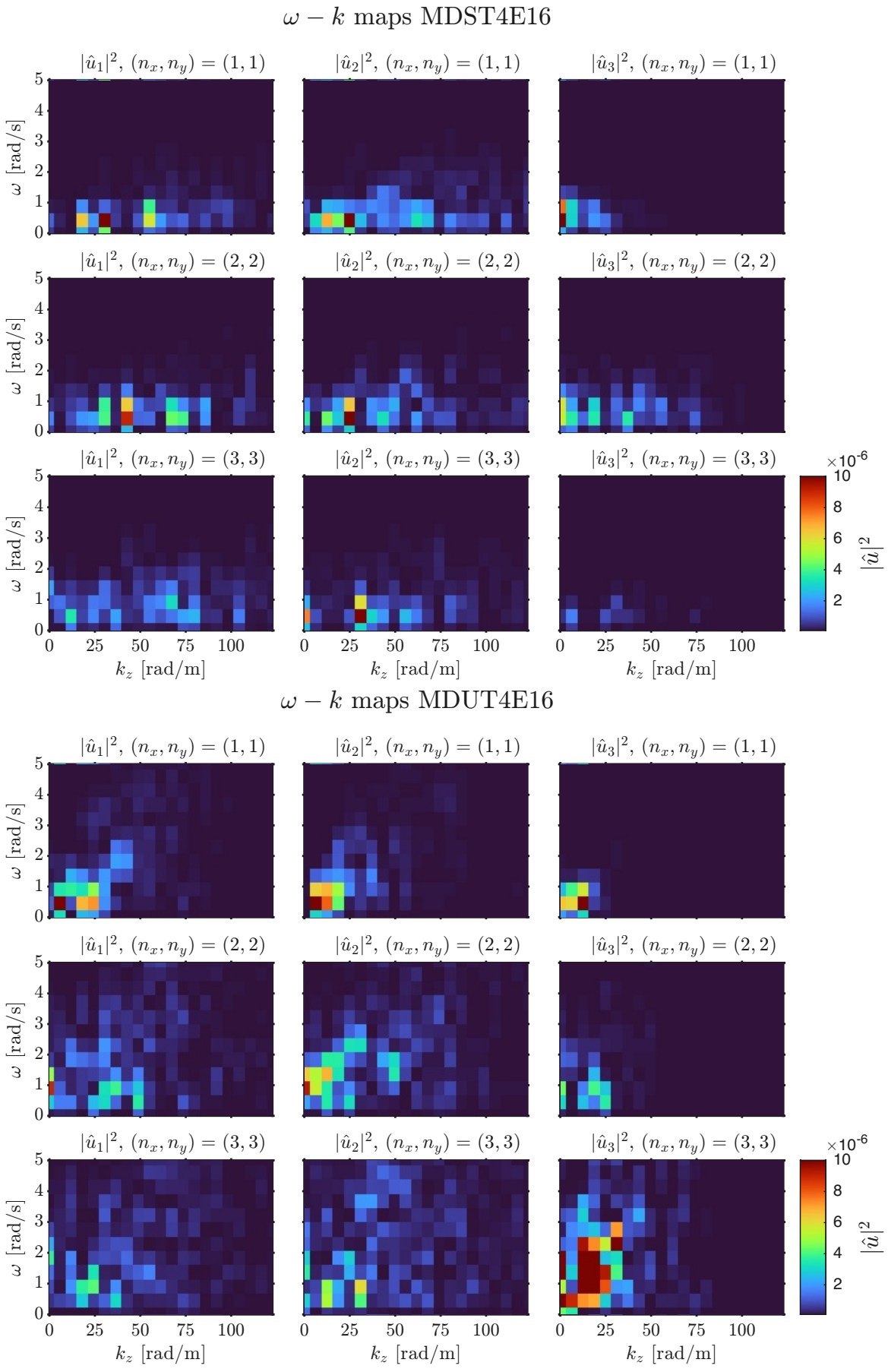

Figure 3.49: ω–k_z spectra for $(k_x, k_y) = (1,1), (2,2), (3,3)$. Strongly stratified cases MDST4E16 (top), MDUT4E16 (bottom).

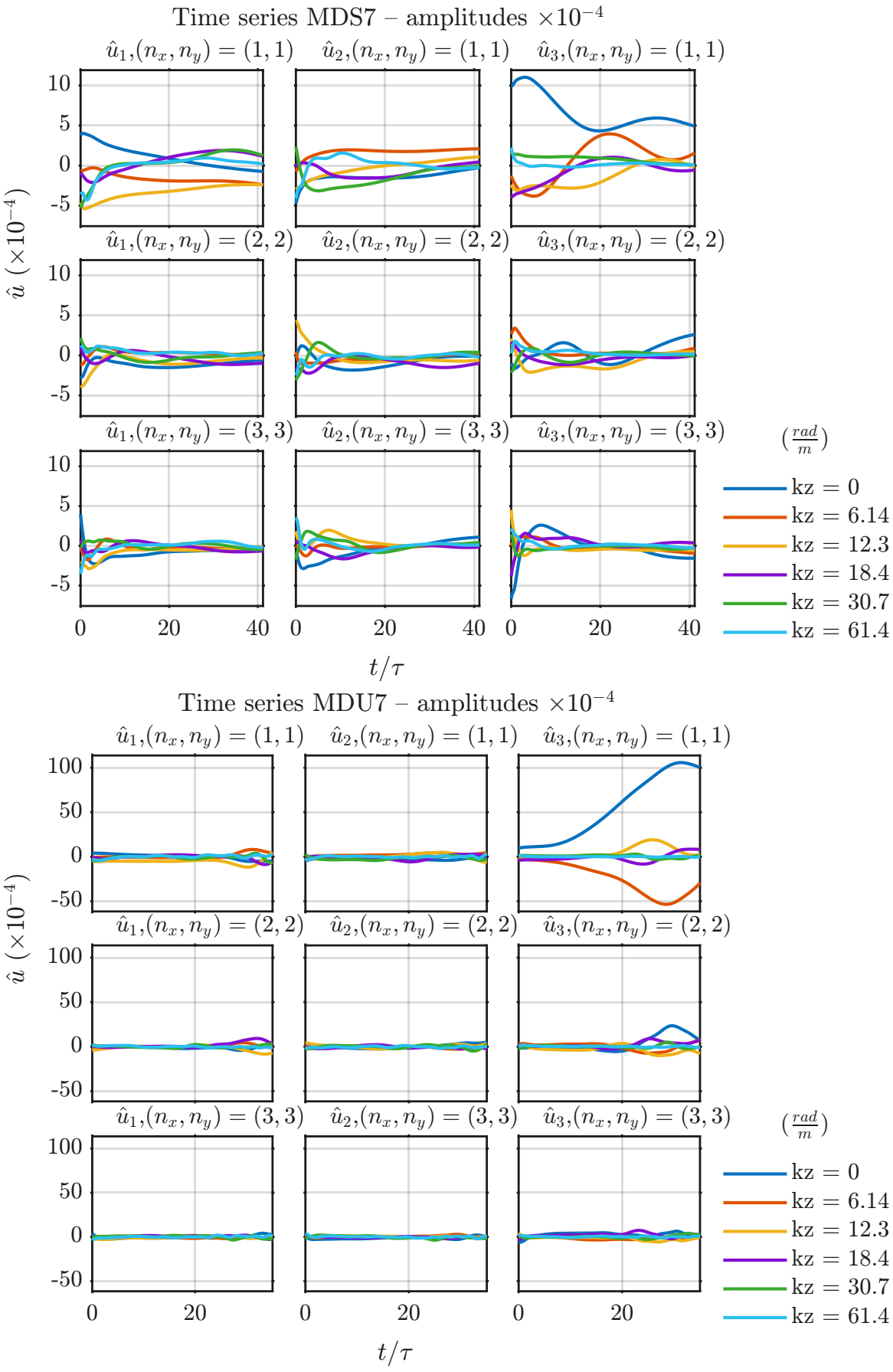

Figure 3.50: Modes at fixed $(k_x, k_y) = \{(1,1);(2,2);(3,3)\}$ at different k_z as function of time—on the top the stable MDS7 case and on the bottom MDU7.

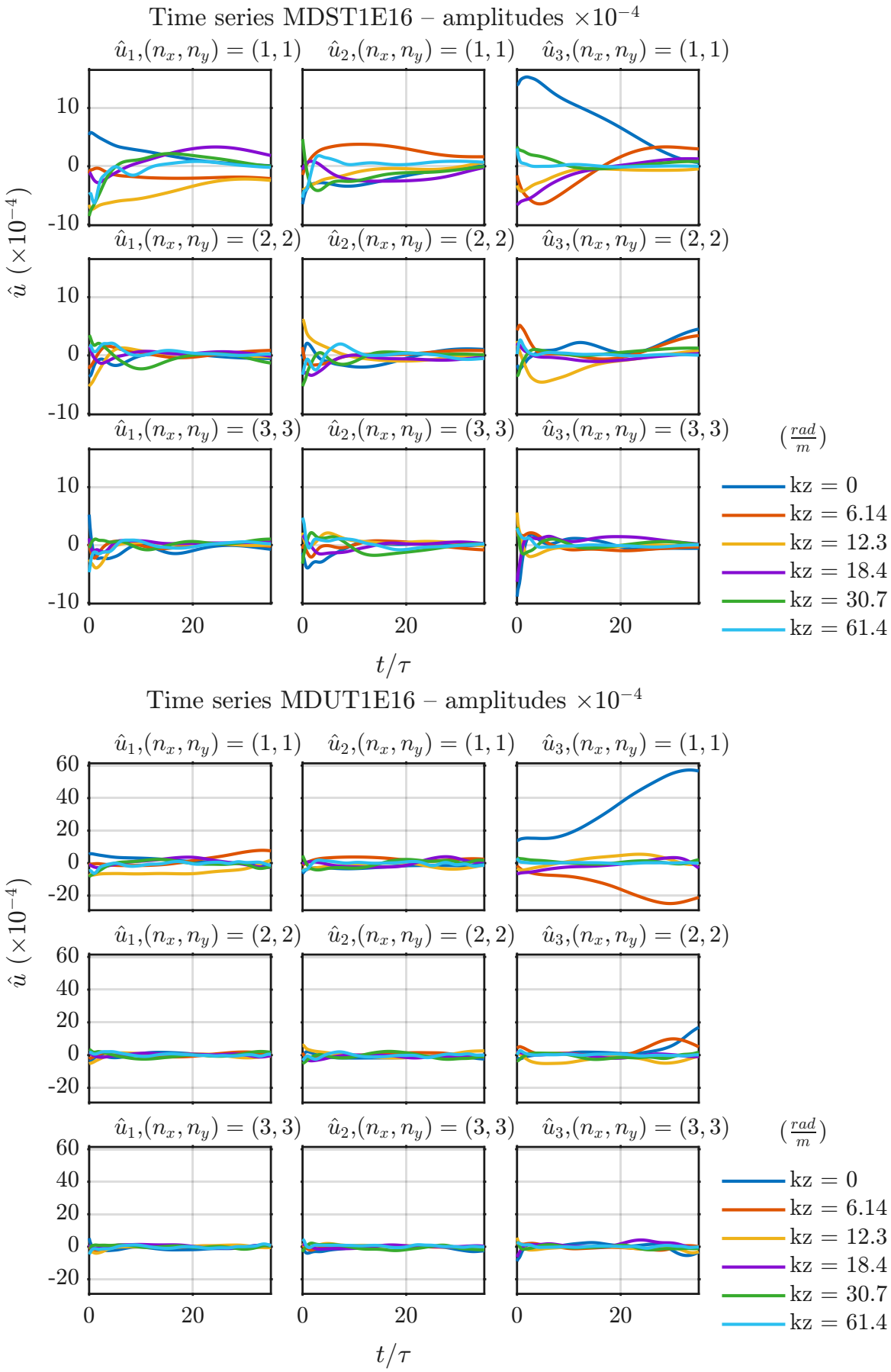

Figure 3.51: Modes at fixed $(k_x, k_y) = \{(1,1);(2,2);(3,3)\}$ at different k_z as function of time—on the top the stable MDST1E16 case and on the bottom MDUT1E16.

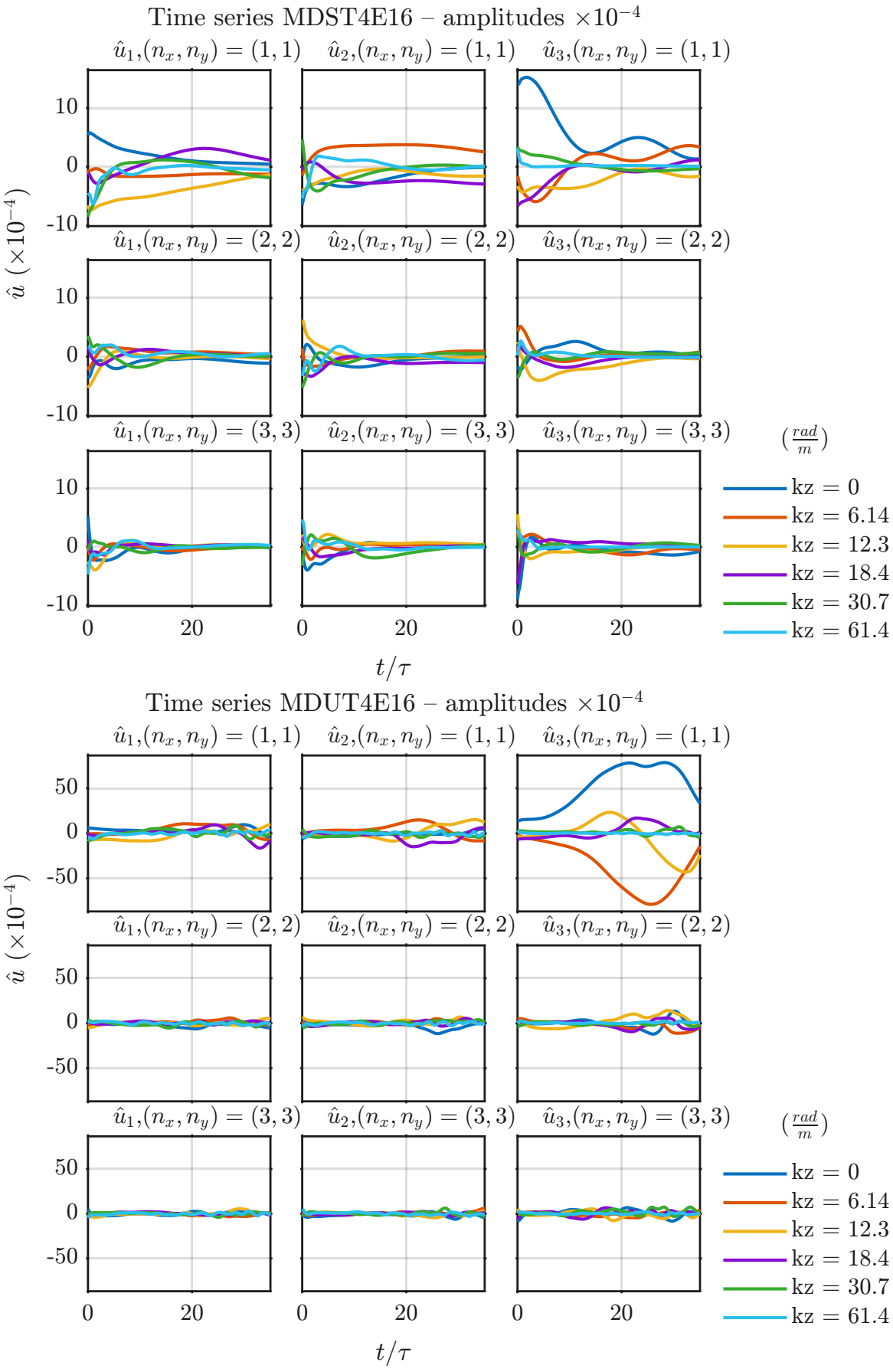

Figure 3.52: Modes at fixed $(k_x, k_y) = \{(1,1);(2,2);(3,3)\}$ at different k_z as function of time—on the top the stable MDST4E16 case and on the bottom MDUT4E16.

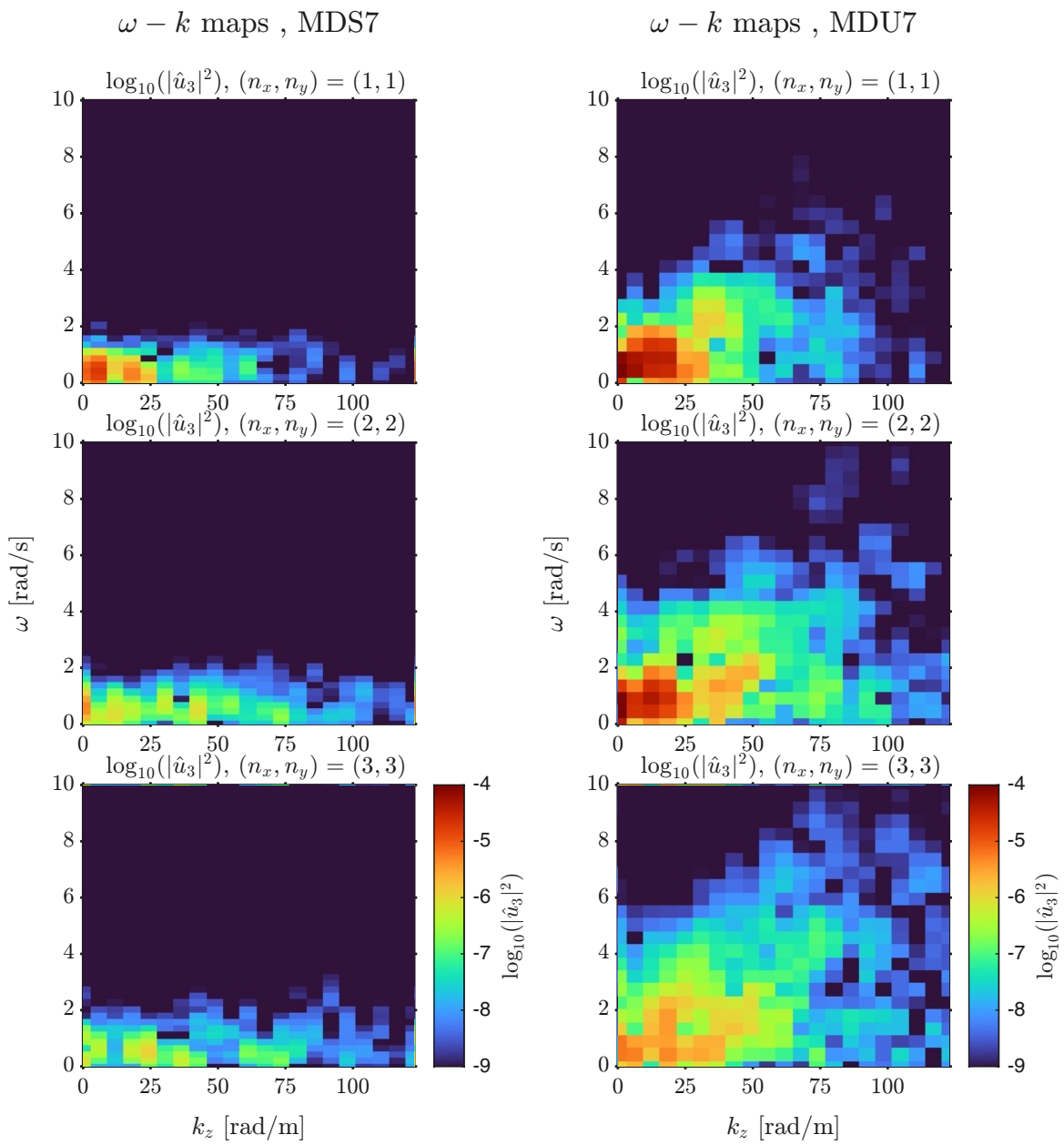

Figure 3.53: ω–k_z spectra of u_3 for $(k_x, k_y) = (1, 1), (2, 2), (3, 3)$, in logarithmic scale—MDS7 on the left and MDU7 on the right.

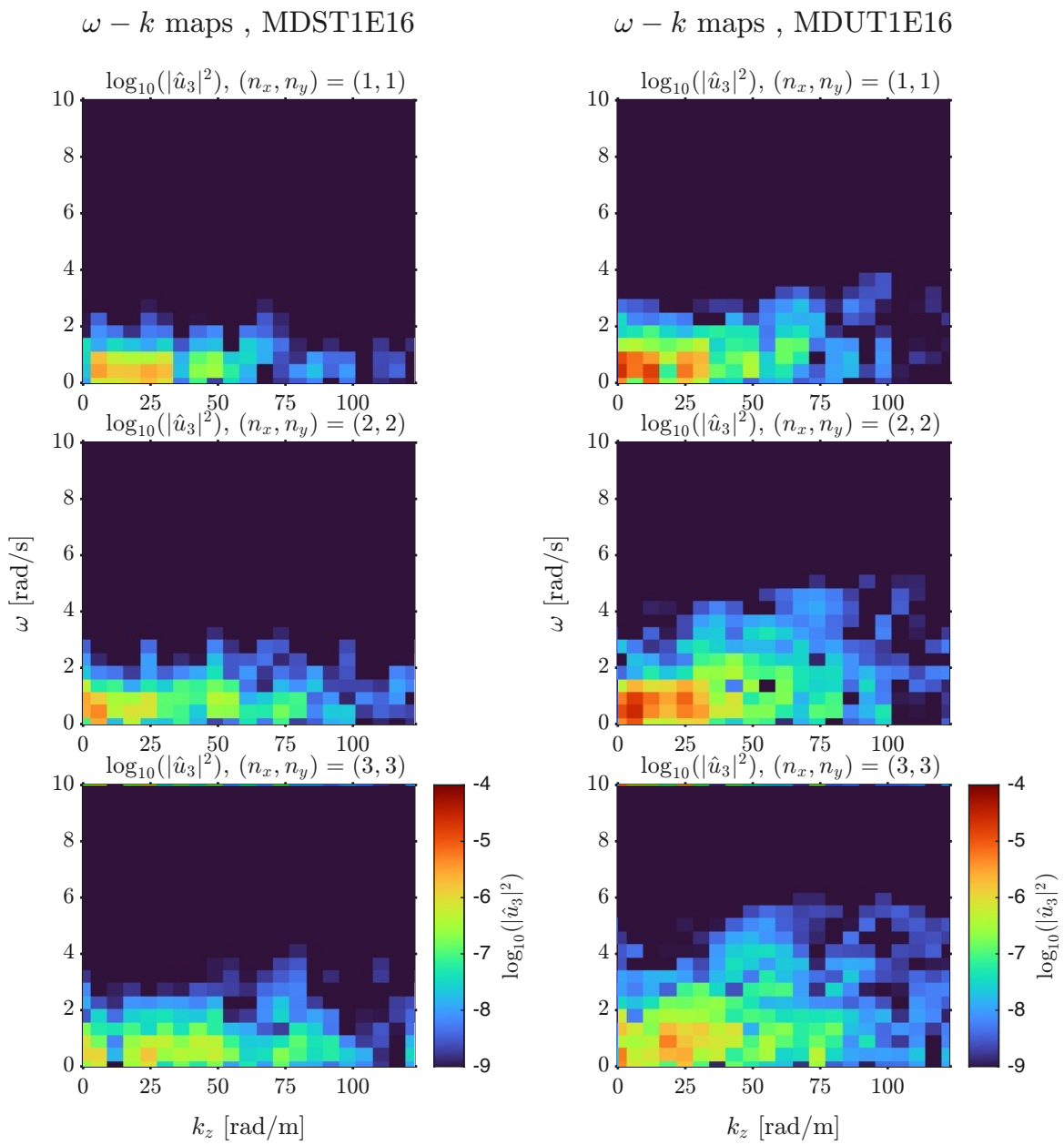

Figure 3.54: ω–k_z spectra of u_3 for $(k_x, k_y) = (1, 1), (2, 2), (3, 3)$, in logarithmic scale—MDST1E16 on the left and MDUT1E16 on the right.

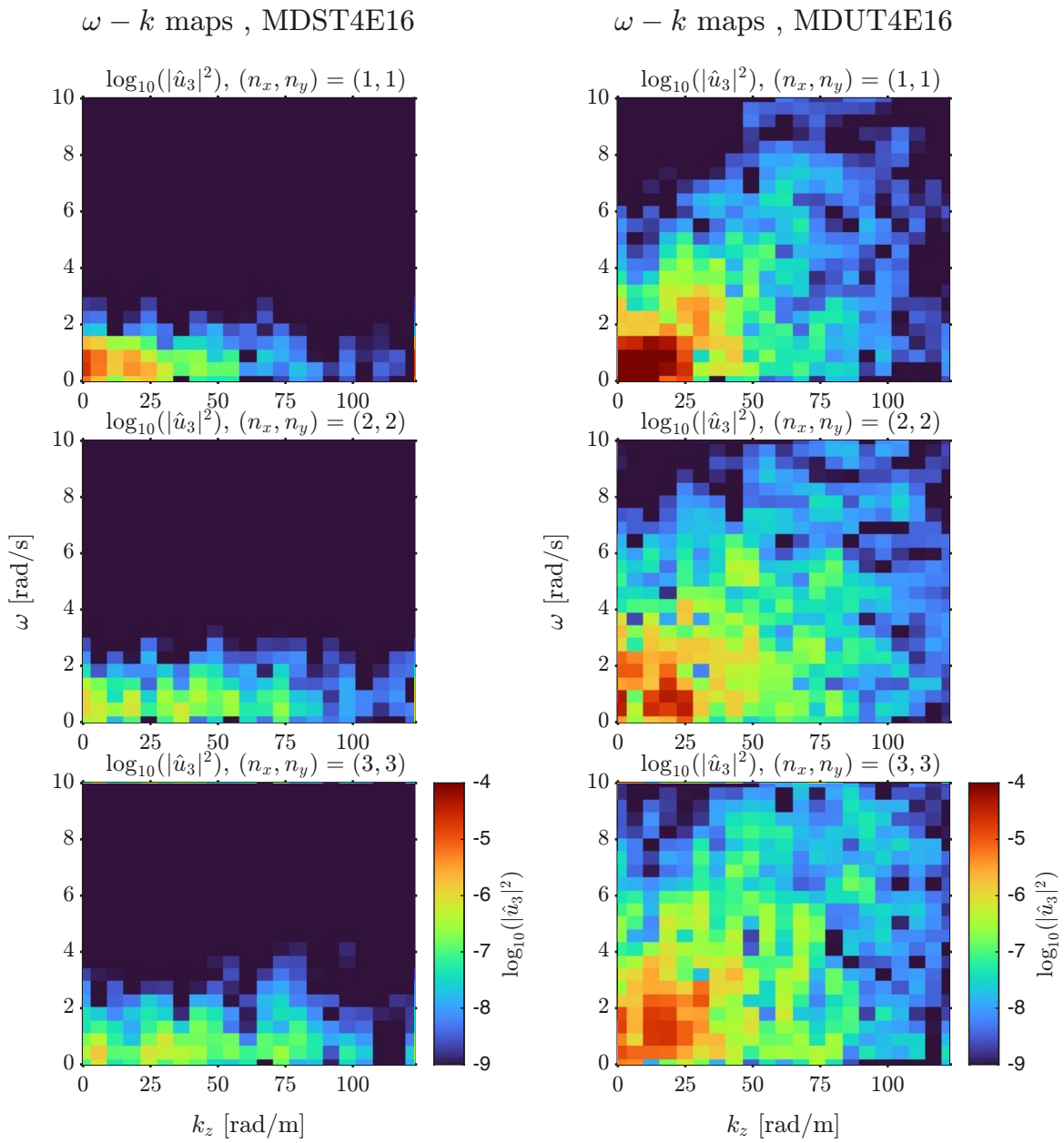

Figure 3.55: ω–k_z spectra of u_3 for $(k_x, k_y) = (1, 1), (2, 2), (3, 3)$, in logarithmic scale—MDST4E16 on the left and MDUT4E16 on the right.

Chapter 4

Conclusions

In this work, the dynamics of mixing between cloudy and clear-air regions have been investigated by means of high-resolution pseudo-spectral Direct Numerical Simulations (DNS) within the Boussinesq approximation. The simulations were designed to isolate the effects of stratification on a two-phase turbulent field, exploring both stable and unstable configurations and including the influence of advected Lagrangian droplets through latent-heat release.

Summary of results The temporal evolution of the turbulent kinetic energy (TKE) revealed the strong modulation induced by buoyancy. In the stably stratified regime, vertical motions are inhibited and the TKE decays more rapidly near the interface, exhibiting oscillatory behaviour associated with internal gravity waves (IGWs). In contrast, in the unstable regime, convective overturning regenerates turbulent fluctuations, leading to sustained mixing and enhanced small-scale activity.

Thermodynamic and microphysical quantities, such as potential temperature and vapour content, indicate that the mixing layer thickens in time while scalar variance decreases as buoyancy progressively dominates over inertial dynamics. The computed Brunt–Väisälä frequency $\mathcal{N}^2(z,t)$ and Froude number Fr quantify this transition, marking the shift from a turbulence-dominated state ($Fr > 1$) to a buoyancy-controlled regime ($Fr < 1$).

Spectral analyses in both space and time domains showed the coexistence of turbulent and wave-like dynamics. In stably stratified runs, the frequency spectra of vertical velocity and acceleration exhibit sharp peaks close to the local buoyancy frequency, confirming the presence of coherent IGW modes. In contrast, unstable configurations are characterised by broadband spectra without dominant frequencies, consistent with convective turbulence.

A notable aspect of the present simulations is the temporal extent: integrations are significantly longer than in previous micro-scale DNS studies. This extended duration allows the system to evolve across multiple buoyancy periods, revealing the progressive establishment of low-frequency oscillations and the nonlinear coupling between residual

turbulence and wave activity. Such behaviour is rarely captured in previous numerical studies, which typically truncate the evolution before the slow IGW dynamics emerge.

The analysis of droplet populations showed that microphysical dispersion exerts a secondary influence on the global energy budget within the simulated timescales, but differences between mono- and poly-disperse cases become visible at later stages, particularly in the vertical distribution of energy. Further analysis can be made to have an insight on the causation of this differences.

Physical interpretation The results demonstrate that stratification introduces a fundamental anisotropy in the turbulent field, suppressing vertical transport and enhancing horizontal coherence. The observed oscillations in TKE and the spectral peaks near $\mathcal{N}$ are clear signatures of wave–turbulence coupling, in which energy is periodically exchanged between kinetic and potential components. In unstable configurations, buoyancy acts in the opposite sense, driving convective overturning and restoring turbulence, with increased dissipation and mixing efficiency. The comparison between stable and unstable regimes thus illustrates the dual role of buoyancy as both a stabilising and destabilising mechanism depending on the sign of the stratification.

At the microscales considered here, where both the Kolmogorov and buoyancy scales are directly resolved, the present results provide rare numerical evidence of the gradual transition from isotropic turbulence to mixed wave–turbulent dynamics. The extended temporal evolution highlights that IGW activity can persist even as turbulence decays, implying that the small-scale mixing layer retains a slow oscillatory memory of the stratified structure.

Limitations and future perspectives The present simulations, though fully resolved, are limited to an idealised small-scale domain and neglect radiative processes, droplet feedback on momentum, and large-scale environmental forcing. Nevertheless, the framework developed here opens several avenues for future investigation:

- Exploring Fourier-Spectral analysis of the Lagrangian datasets of the droplets.
- Computing joint probability density functions (PDFs) of droplet radius, supersaturation, and vertical velocity to quantify the statistical imprint of stratification on microphysical variability.
- Extending the analysis of polydisperse populations. A deeper investigation of polydisperse droplet fields should be carried out, examining how size distribution width, condensation growth, and gravitational settling influence the local stratification, the temporal evolution of $\mathcal{N}^2$, and the small-scale spectra of velocity and temperature. Such analysis could clarify under which conditions microphysical diversity becomes dynamically relevant.

- Exploring larger computational domains or hybrid multi-scale approaches that couple DNS with reduced-order or stochastic subgrid models, in order to connect micro-scale results with mesoscale and atmospheric-scale parametrisations.

Closing remarks Overall, this study provides a detailed numerical picture of the interplay between turbulence, stratification, and microphysics in cloud–clear-air mixing at the micro-scale. The results emphasise how buoyancy modulates the evolution of turbulent energy and triggers internal-wave activity that persists well beyond the active mixing stage. By combining high temporal resolution, extended integration time, and full spectral diagnostics, this work contributes to filling a gap in the literature on stratified micro-scale flows and offers a framework for future investigations on wave–turbulence–microphysics coupling in atmospheric systems.

Appendix A

Cloud Microphysics

A.1 Cloud Microphysics

In the present work, the evolution of droplets is not the primary focus. As will be shown in the system of equations (1.3), their dynamics exert only a minor, often negligible, influence on the velocity field. In fact, their effect appears solely in the energy equation (1.12), through the source term associated with latent heat ($\mathcal{L}$). Nevertheless, it is useful to outline the underlying physical setting and provide a concise theoretical background, in order to highlight the main physical processes governing the system. For this reason, a brief introduction to cloud microphysics is presented in this section. A more comprehensive and detailed treatment can be found in the literature [8, 33, 34]. Cloud microphysics investigates the small-scale processes that govern the formation, growth, and evolution of droplets and ice crystals. These processes provide the link between atmospheric aerosols, water vapour, and hydrometeors, ultimately determining cloud lifetime, radiative properties, and the onset of precipitation. In the context of this study we restrict our attention to *warm clouds*, where hydrometeors remain in the liquid phase, and focus on how turbulence modifies the pathways of droplet activation and growth.

A.1.1 Nucleation and Activation

Cloud formation begins with the phase transition of water vapor into liquid droplets or ice crystals. In the atmosphere, this process occurs predominantly through **heterogeneous nucleation**, where water vapor condenses on aerosol particles acting as **cloud condensation nuclei** (CCN). These nuclei reduce the equilibrium vapor pressure, making condensation possible at realistic supersaturation levels. In contrast, **homogeneous nucleation** — where droplets form without pre-existing particles — requires unrealistically high supersaturations ($s > 100\%$) and therefore does not occur under typical atmospheric conditions .

The equilibrium vapor pressure over a flat water surface, $e_s(T)$, varies with temper-

ature according to the **Clausius–Clapeyron relation**:

$$\frac{de_s}{dT} = \frac{\mathcal{L}_w e_s}{R_v T^2}, \tag{A.1}$$

where $\mathcal{L}_w$ is the latent heat of vaporization and R_v is the specific gas constant for water vapour. Integrating this equation (assuming $\mathcal{L}_w$ constant) yields the saturation vapour pressure:

$$e_s(T) = e_{s0} \exp\left[\frac{\mathcal{L}_w}{R_v}\left(\frac{1}{T_0} - \frac{1}{T}\right)\right], \tag{A.2}$$

where e_{s0} is the reference saturation vapor pressure at temperature T_0.

The actual state of the vapor field is commonly expressed by the **relative humidity**:

$$RH = \frac{e}{e_s},$$

where e is the actual vapor pressure. When $RH = 1$, the air is saturated and condensation and evaporation rates are balanced. It is often convenient to define the **supersaturation**:

$$s = \frac{e - e_s}{e_s} = RH - 1. \tag{A.3}$$

Positive values ($s > 0$) indicate conditions favorable for droplet growth, while $s < 0$ leads to evaporation.

Typical atmospheric supersaturations are very small, usually $s < 2\%$. As a result, cloud droplet formation almost always occurs on CCN. These CCN can be *inorganic* (e.g., sea salt, sulfates) or *organic* (e.g., products of biomass burning or biogenic emissions), with typical diameters ranging from 0.01 to 1 μm. Occasionally, giant CCN ($2-10\,\mu$m) are present and can activate at lower supersaturations, promoting rapid initial growth and facilitating early precipitation processes.

When environmental supersaturation exceeds a critical value, an aerosol particle becomes activated and grows spontaneously by vapor condensation.

A.1.2 Growth by Condensation

Once activated, droplets are no longer in equilibrium and grow primarily through diffusional condensation. Unlike nucleation, which involves the initial formation of stable clusters, condensational growth is continuous and proceeds as long as the surrounding air remains supersaturated.

According to the Köhler theory [35], the growth rate of a spherical droplet of radius r can be expressed as:

$$\frac{dr}{dt} = \frac{C_r}{r}\left[s - \left(\frac{A}{r} - \frac{B r_{\mathrm{dry}}^3}{r^3}\right)\right], \tag{A.4}$$

where:

- s is the ambient supersaturation,
- r_{dry} is the radius of the dry aerosol core,
- B is a hygroscopicity parameter representing solute effects,
- A is the Kelvin curvature coefficient,
- C_r is the condensation coefficient, which depends on the diffusivity of water vapor, thermal conductivity of air, temperature, and pressure.

The term in parentheses represents the equilibrium supersaturation over a droplet of radius r:

$$s_{eq}(r) = \frac{A}{r} - \frac{Br_{\text{dry}}^3}{r^3}, \tag{A.5}$$

which combines two competing effects:

1. **Kelvin effect** (A/r): due to surface curvature, small droplets exhibit higher equilibrium vapor pressures, making growth more difficult.
2. **Raoult effect** (Br_{dry}^3/r^3): dissolved solutes lower equilibrium vapor pressure, stabilizing small droplets and favoring condensation.

Thus, a droplet will grow ($dr/dt > 0$) when the ambient supersaturation exceeds $s_{eq}(r)$. Initially, growth is rapid for very small droplets due to steep vapor gradients, but slows as:

1. the droplet radius increases, reducing curvature effects,
2. local vapor is depleted by condensation.

At the cloud scale, supersaturation evolves dynamically as a competition between production and depletion:

$$\frac{ds}{dt} = P - C, \tag{A.6}$$

where:

- P is the **production term**, primarily driven by adiabatic cooling in rising air parcels,
- C is the **consumption term**, representing the vapor depletion due to condensation onto the droplet population.

A.1.3 Collision–Coalescence

Condensation alone cannot generate precipitation-sized droplets ($r > 100\,\mu$m) within the typical lifetime of a cloud (tens of minutes). As droplets grow by condensation to radii of approximately $10-20\,\mu$m, their gravitational settling velocities become significant. Beyond this threshold, the **collision–coalescence** process becomes the dominant growth mechanism.

Because larger droplets fall faster than smaller ones, they can overtake and collide with them. The rate at which a droplet of radius R collides with droplets of radius r is described by the *collection kernel* :

$$K(R, r) = \pi(R + r)^2 E(R, r) \left| V_t(R) - V_t(r) \right|, \tag{A.7}$$

where:

- $V_t(R)$ and $V_t(r)$ are the terminal fall velocities of the droplets,
- $E(R, r)$ is the *collection efficiency*, defined as the product of:
  1. the *collision efficiency*, i.e., the fraction of geometrically possible trajectories that actually result in a collision,
  2. the *coalescence efficiency*, i.e., the probability that two colliding droplets merge rather than bouncing or temporarily separating.

In natural clouds, turbulent air motions significantly increase collision rates through two main mechanisms:

(i) by increasing the *relative velocity* between droplets beyond that due to gravity alone,

(ii) by inducing *preferential concentration* or clustering of droplets in regions of high strain and low vorticity.

These turbulence-induced effects are especially important for the initial stage of precipitation formation. They promote the appearance of a few larger droplets, known as *collector drops*, which subsequently undergo rapid, *runaway growth* by sweeping up surrounding smaller droplets. This runaway process eventually produces raindrops within the cloud's lifetime.

A.1.4 Role of Turbulence and Mixing

At cloud boundaries, mixing between cloudy and clear air further influences microphysics. When entrainment of dry air occurs, droplets experience rapid changes in

local supersaturation, which can lead to either homogeneous or inhomogeneous mixing depending on the relative timescales of turbulence and microphysics.

A useful nondimensional parameter is the *Damköhler number*:

$$Da = \frac{\tau_{\text{turb}}}{\tau_{\text{micro}}}, \tag{A.8}$$

where τ_{turb} is a characteristic turbulent timescale and τ_{micro} a microphysical timescale (such as condensation time or phase relaxation time).

- If $Da \ll 1$, turbulence is fast compared to microphysics: mixing is homogeneous, and droplets respond uniformly.
- If $Da \gg 1$, microphysics is faster: mixing is inhomogeneous, producing a broadened size spectrum.

These mixing regimes have direct implications for cloud lifetime, albedo, and precipitation efficiency.

Appendix B

Signal Processing Tools

B.1 Short-Time Fourier Transform

A standard Fourier transform applied over the entire time span of a signal only provides a global frequency representation and does not capture how the frequency content evolves over time. This limitation is particularly evident in *intermittent signals*, such as those arising from decaying turbulence, where localized bursts of activity and coherent structures coexist.

To address this issue, the **Short-Time Fourier Transform (STFT)** combines the time and frequency domains into a single framework, allowing the study of how the spectral content varies over time. The signal is divided into overlapping segments, each multiplied by a suitable window function, and a Fourier transform is applied to each segment separately. This procedure produces a time–frequency representation of the signal, forming the basis of a spectrogram [36].

Discrete Formulation

We now introduce the STFT from a discrete point of view, considering a sampled signal $x[n]$ defined at discrete time indices n. The classical discrete-time Fourier transform (DTFT) of $x[n]$ is:

$$X(\omega) = \sum_n x[n]\, e^{-i\omega n}. \tag{B.1}$$

In contrast, the STFT at a specific time index n_0 is defined as

$$X(n_0, \omega) = \sum_n x[n]\, w[n_0 - n]\, e^{-i\omega n}, \tag{B.2}$$

where $w[n]$ is the *analysis window* that selects a short time segment around n_0. The product $x[n]\, w[n_0 - n]$ represents the portion of the signal localized near time n_0. By sliding the window along the time axis and repeating the Fourier transform for each position, we obtain a sequence of localized spectra.

Finally, using a generic time-shift parameter m to represent the sliding operation, the discrete STFT becomes:

$$X(m,\omega) = \sum_{n} x[n]\, w[m-n]\, e^{-i\omega n}. \tag{B.3}$$

The choice of the window function $w[n]$ strongly affects the quality of the resulting spectrogram. In this work, a Hamming window is adopted due to its favorable trade-off between frequency resolution and spectral leakage, as discussed in the next section.

B.2 Hamming Window

When performing a Discrete Fourier Transform (DFT) on a finite signal segment, discontinuities at the edges of the segment introduce spurious frequency components, a phenomenon known as *spectral leakage*. Window functions are introduced to mitigate this effect by smoothly tapering the signal to zero at the boundaries, thus reducing discontinuities before the Fourier transform is computed.

Among the various window functions, the **Hamming window** is a common choice, providing a good compromise between frequency resolution and leakage reduction. It is defined for a segment of length N as:

$$w[n] = 0.54 - 0.46\cos\left(\frac{2\pi n}{N-1}\right), \qquad 0 \le n \le N-1, \tag{B.4}$$

where n is the sample index within the window.

The main properties of the Hamming window are:

- A smooth tapering of the amplitude near the edges, minimizing discontinuities between adjacent segments.
- A relatively narrow main lobe in the frequency domain, which provides reasonable frequency resolution.
- Significantly attenuated side lobes (approximately -41 dB below the main lobe), reducing spectral leakage compared to a simple rectangular window.

Application in this study

In this work, a Hamming window of length 90 samples was applied prior to each FFT in the STFT computation, with a 50% overlap between consecutive windows. This configuration provides a balance between temporal resolution and frequency resolution, ensuring that the resulting spectrograms reveal the true physical dynamics of the flow.

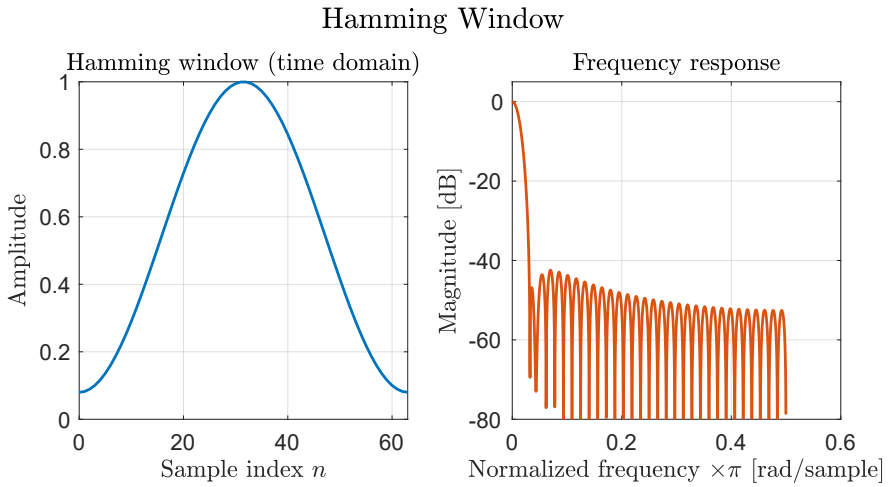

Figure B.1: Hamming window: (left) time-domain shape; (right) frequency response showing main lobe and side lobes. Picture adapted from [37].

The use of the Hamming window is particularly important in this context, as the analyzed signals contain both intermittent turbulence bursts and coherent internal waves. Without a proper window, the spectrogram would be dominated by artificial oscillations introduced by the finite-length sampling, obscuring the physical features of interest. By applying the Hamming window, these artifacts are minimized, and the time–frequency representation highlights the actual flow structures and their evolution.

Bibliography

[1] CP Caulfield. "Layering, instabilities, and mixing in turbulent stratified flows". In: *Annual Review of Fluid Mechanics* 53.1 (2021), pp. 113–145. DOI: https://doi.org/10.1146/annurev-fluid-042320-100458 (cit. on p. 2).

[2] Jielun Sun et al. "Review of wave-turbulence interactions in the stable atmospheric boundary layer". In: *Reviews of geophysics* 53.3 (2015), pp. 956–993. DOI: https://doi.org/10.1002/2015RG000487 (cit. on p. 3).

[3] Juan Pedro Mellado. "Cloud-top entrainment in stratocumulus clouds". In: *Annual Review of Fluid Mechanics* 49.1 (2017), pp. 145–169. DOI: 10.1146/annurev-fluid-010816-060231 (cit. on p. 3).

[4] Juan-Pedro Mellado, CS Bretherton, Bjorn Stevens, and MC Wyant. "DNS and LES for simulating stratocumulus: Better together". In: *Journal of Advances in Modeling Earth Systems* 10.7 (2018), pp. 1421–1438. DOI: https://doi.org/10.1029/2018MS001312 (cit. on p. 3).

[5] Bipin Kumar, Jörg Schumacher, and Raymond A Shaw. "Cloud microphysical effects of turbulent mixing and entrainment". In: *Theoretical and Computational Fluid Dynamics* 27.3 (2013), pp. 361–376. DOI: 10.1007/s00162-012-0272-z (cit. on p. 3).

[6] Ludovico Fossà, Shahbozbek Abdunabiev, Mina Golshan, and Daniela Tordella. "Microphysical timescales and local supersaturation balance at a warm cloud top boundary". In: *Physics of Fluids* 34.6 (2022). DOI: https://doi.org/10.1063/5.0090664 (cit. on pp. 3, 35, 46).

[7] Mina Golshan, Shahbozbek Abdunabiev, Mattia Tomatis, Federico Fraternale, Marco Vanni, and Daniela Tordella. "Intermittency acceleration of water droplet population dynamics inside the interfacial layer between cloudy and clear air environments". In: *International Journal of Multiphase Flow* 140 (2021), p. 103669. ISSN: 0301-9322. DOI: https://doi.org/10.1016/j.ijmultiphaseflow.2021.103669. URL: https://www.sciencedirect.com/science/article/pii/S0301932221001178 (cit. on pp. 3, 21, 37, 46).

[8] Murry L Salby. *Physics of the Atmosphere and Climate*. Cambridge University Press, 2012 (cit. on pp. 6, 8, 115).

[9] Roland Stull. *Practical Meteorology: An Algebra-based Survey of Atmospheric Science*. Available at: <https://www.eoas.ubc.ca/books/Practical$_M$eteorology/ >. 2017 (cit. on pp. 6, 20).

[10] Douglas K. Randall. *Atmosphere, Clouds, and Climate*. National Academies Press, 2012 (cit. on p. 6).

[11] United States Committee on Extension to the Standard Atmosphere. *US standard atmosphere, 1976*. National Oceanic and Amospheric [sic] Administration, 1976 (cit. on p. 12).

[12] George Keith Batchelor. *The theory of homogeneous turbulence*. Cambridge university press, 1953 (cit. on p. 13).

[13] H. J. S. Fernando. "Turbulence in Stratified Fluids". In: *Environmental Stratified Flows*. Ed. by Roger Grimshaw. Boston, MA: Springer US, 2002, pp. 161–189. ISBN: 978-0-306-48024-9. DOI: 10.1007/0-306-48024-7_6. URL: https://doi.org/10.1007/0-306-48024-7_6 (cit. on p. 16).

[14] GN Ivey and J Imberger. "On the nature of turbulence in a stratified fluid. Part I: The energetics of mixing". In: *Journal of Physical Oceanography* 21.5 (1991), pp. 650–658. DOI: 10.1175/1520-0485(1991)021<0650:OTNOTI>2.0.CO;2 (cit. on p. 16).

[15] Paul Billant and Jean-Marc Chomaz. "Self-similarity of strongly stratified inviscid flows". In: *Physics of fluids* 13.6 (2001), pp. 1645–1651. DOI: 10.1063/1.1369125 (cit. on p. 16).

[16] Carl H Gibson. "Laboratory, numerical, and oceanic fossil turbulence in rotating and stratified flows". In: *Journal of Geophysical Research: Oceans* 96.C7 (1991), pp. 12549–12566. DOI: https://doi.org/10.1029/91JC00186 (cit. on p. 16).

[17] Edward A Spiegel and G Veronis. "On the Boussinesq approximation for a compressible fluid." In: *Astrophysical Journal, vol. 131, p. 442* 131 (1960), p. 442. DOI: 10.1086/146849 (cit. on p. 21).

[18] Rupert Klein, Ulrich Achatz, Didier Bresch, Omar M Knio, and Piotr K Smolarkiewicz. "Regime of validity of soundproof atmospheric flow models". In: *Journal of the Atmospheric Sciences* 67.10 (2010), pp. 3226–3237. DOI: https://doi.org/10.1175/2010JAS3490.1 (cit. on p. 21).

[19] PA Vaillancourt, MK Yau, and Wojciech W Grabowski. "Microscopic approach to cloud droplet growth by condensation. Part I: Model description and results without turbulence". In: *Journal of the atmospheric sciences* 58.14 (2001), pp. 1945–1964. DOI: https://doi.org/10.1175/1520-0469(2001)058<1945:MATCDG>2.0.CO;2 (cit. on p. 21).

[20] Jacques Descloitres and MODIS Rapid Response Team. *Atmospheric gravity waves and internal waves off Australia (MODIS/Terra)*. https://visibleearth.nasa.gov/images/69463/atmospheric-gravity-waves-and-internal-waves-off-australia. Image acquired November 11, 2003; published December 5, 2003. 2003 (cit. on p. 23).

[21] Bruce R Sutherland. *Internal gravity waves*. Cambridge university press, 2010 (cit. on p. 24).

[22] Geoffrey K. Vallis. "Gravity Waves". In: *Atmospheric and Oceanic Fluid Dynamics: Fundamentals and Large-Scale Circulation*. Cambridge University Press, 2017, pp. 251–296 (cit. on p. 24).

[23] John Stewart Turner. *Buoyancy effects in fluids*. Cambridge university press, 1979 (cit. on p. 24).

[24] Dale R Durran and Joseph B Klemp. "On the effects of moisture on the Brunt–Väisälä frequency". In: *J. Atmos. Sci* 39.10 (1982), pp. 2152–2158. DOI: https://doi.org/10.1175/1520-0469(1982)039<2152:OTEOMO>2.0.CO;2 (cit. on p. 28).

[25] F Einaudi and DP Lalas. "The propagation of acoustic-gravity waves in a moist atmosphere". In: *Journal of Atmospheric Sciences* 30.3 (1973), pp. 365–376. DOI: https://doi.org/10.1175/1520-0469(1973)030<0365:TPOAGW>2.0.CO;2 (cit. on p. 28).

[26] Michele Iovieno, Carlo Cavazzoni, and Daniela Tordella. "A new technique for a parallel dealiased pseudospectral Navier–Stokes code". In: *Computer physics communications* 141.3 (2001), pp. 365–374. DOI: https://doi.org/10.1016/S0010-4655(01)00433-7 (cit. on pp. 31, 34).

[27] Philofluid Group. *Incompressible Turbulent Flows*. https://philofluid.polito.it/software/incompressible-turbulent-flows/. 2025 (cit. on p. 31).

[28] Claudio Canuto, M Yousuff Hussaini, Alfio Quarteroni, and Thomas A Zang. *Spectral Methods in Fluid Dynamics*. 1988 (cit. on p. 31).

[29] Michel Fortin and Franco Brezzi. *Mixed and hybrid finite element methods*. Vol. 2. New York: Springer-Verlag, 1991 (cit. on p. 31).

[30] Daniela Tordella and Michele Iovieno. "Small-scale anisotropy in turbulent shearless mixing". In: *Physical review letters* 107.19 (2011), p. 194501. DOI: 10.1103/PhysRevLett.107.194501 (cit. on p. 36).

[31] Luca Gallana, Shahbozbek Abdunabiev, Mina Golshan, and Daniela Tordella. "Diffusion of turbulence following both stable and unstable step stratification perturbations". In: *Physics of Fluids* 34.6 (2022). DOI: 10.1063/5.0090042 (cit. on pp. 38, 60, 69).

[32] Marie Poulain-Zarcos, Matthieu J. Mercier, and Alexandra ter Halle. "Global characterization of oscillating grid turbulence in homogeneous and two-layer fluids, and its implication for mixing at high Peclet number". In: *Phys. Rev. Fluids* 7 (5 May 2022), p. 054606. DOI: 10.1103/PhysRevFluids.7.054606. URL: https://link.aps.org/doi/10.1103/PhysRevFluids.7.054606 (cit. on p. 61).

[33] Hans R Pruppacher and James D Klett. *Microphysics of clouds and precipitation: Reprinted 1980*. Springer Science & Business Media, 2012 (cit. on p. 115).

[34] Man Kong Yau and Roddy Rhodes Rogers. *A short course in cloud physics*. Elsevier, 1996 (cit. on p. 115).

[35] Hilding Köhler. "The nucleus in and the growth of hygroscopic droplets". In: *Transactions of the Faraday Society* 32 (1936), pp. 1152–1161. DOI: 10.1039/TF9363201152 (cit. on p. 116).

[36] S Hamid Nawab and Thomas F Quatieri. "Short-time Fourier transform". In: *Advanced topics in signal processing*. 1987, pp. 289–337 (cit. on p. 120).

[37] MathWorks. *Hamming Window*. https://it.mathworks.com/help/signal/ref/hamming.html. Last accessed: 10 September 2025. 2025 (cit. on p. 122).